Cosmology with weak lensing surveys

Dipak Munshi [a,b,*], Patrick Valageas [c], Ludovic van Waerbeke [d], Alan Heavens [e]

[a] *Institute of Astronomy, Madingley Road, Cambridge, CB3 OHA, UK*
[b] *Astrophysics Group, Cavendish Laboratory, Madingley Road, Cambridge CB3 OHE, UK*
[c] *Service de Physique Théorique, CEA Saclay, 91191 Gif-sur-Yvette, France*
[d] *University of British Columbia, Department of Physics and Astronomy, 6224 Agricultural Road, Vancouver, BC V6T 1Z1, Canada*
[e] *SUPA (Scottish Universities Physics Alliance), Institute for Astronomy, University of Edinburgh, Blackford Hill, Edinburgh EH9 3HJ, UK*

ARTICLE INFO

ABSTRACT

Weak gravitational lensing is responsible for the shearing and magnification of the images of high-redshift sources due to the presence of intervening matter. The distortions are due to fluctuations in the gravitational potential, and are directly related to the distribution of matter and to the geometry and dynamics of the Universe. As a consequence, weak gravitational lensing offers unique possibilities for probing the Dark Matter and Dark Energy in the Universe. In this review, we summarise the theoretical and observational state of the subject, focussing on the statistical aspects of weak lensing, and consider the prospects for weak lensing surveys in the future.

Weak gravitational lensing surveys are complementary to both galaxy surveys and cosmic microwave background (CMB) observations as they probe the unbiased non-linear matter power spectrum at modest redshifts. Most of the cosmological parameters are accurately estimated from CMB and large-scale galaxy surveys, so the focus of attention is shifting to understanding the nature of Dark Matter and Dark Energy. On the theoretical side, recent advances in the use of 3D information of the sources from photometric redshifts promise greater statistical power, and these are further enhanced by the use of statistics beyond two-point quantities such as the power spectrum. The use of 3D information also alleviates difficulties arising from physical effects such as the intrinsic alignment of galaxies, which can mimic weak lensing to some extent. On the observational side, in the next few years weak lensing surveys such as CFHTLS, VST-KIDS and Pan-STARRS, and the planned Dark Energy Survey, will provide the first weak lensing surveys covering very large sky areas and depth. In the long run even more ambitious programmes such as DUNE, the Supernova Anisotropy Probe (SNAP) and Large-aperture Synoptic Survey Telescope (LSST) are planned. Weak lensing of diffuse components such as the CMB and 21 cm emission can also provide valuable cosmological information. Finally, we consider the prospects for joint analysis with other probes, such as (1) the CMB to probe background cosmology (2) galaxy surveys to probe large-scale bias and (3) Sunyaev–Zeldovich surveys to study small-scale baryonic physics, and consider the lensing effect on cosmological supernova observations.

Contents

* Corresponding address: Institute of Astronomy, University of Cambridge, Madingley Road, Cambridge, CB3 OHA, UK. Tel.: +44 1223 766660; fax: +44 1223 337523.
E-mail address: munshi@ast.cam.ac.uk (D. Munshi).

1. Introduction and notations

Gravitational lensing refers to the deflection of light rays from distant sources by the gravitational force arising from massive bodies present along the line of sight. Such an effect was already raised by Newton in 1704 and computed by Cavendish around 1784. As is well known, General Relativity put lensing on a firm theoretical footing, and yields twice the Newtonian value for the deflection angle [72]. The agreement of this prediction with the deflection of light from distant stars by the Sun measured during the solar eclipse of 1919 [71] was a great success for Einstein's theory and brought General Relativity to the general attention. The eclipse was necessary to allow one to detect stars with a line of sight which comes close to the Sun.

In a similar fashion, light rays emitted by a distant galaxy are deflected by the matter distribution along the line of sight toward the observer. This creates a distortion of the image of this galaxy, which is both sheared and amplified (or attenuated). It is possible to distinguish two fields of study which make use of these gravitational lensing effects. First, strong-lensing studies correspond to strongly non-linear perturbations (which can lead to multiple images of distant objects) produced by highly non-linear massive objects (e.g. clusters of galaxies). In this case, the analysis of the distortion of the images of background sources can be used to extract some information on the properties of the well-identified foreground lens (e.g. its mass). Second, cosmic shear, or weak gravitational lensing not associated with a particular intervening lens, corresponds to the small distortion (of the order of 1%) of the images of distant galaxies by all density fluctuations along typical lines of sight. Then, one does not use gravitational lensing to obtain the characteristics of a single massive object but tries to derive the statistical properties of the density field as well as the geometrical properties of the Universe (as described by the cosmological parameters, such as the mean density or the curvature). To this order, one computes the mean shear over a rather large region on the sky (a few arc min^2 or more) from the ellipticities of many galaxies (one hundred or more). Indeed, since galaxies are not spherical one needs to average over many galaxies and cross-correlate their observed ellipticity in order to extract a meaningful signal. Putting together many such observations one obtains a large survey (a few to many thousands of square degrees) which may have an intricate geometry (as observational constraints may produce many holes). Then, by performing various statistical measures one can derive from such observations some constraints on the cosmological parameters as well as on the statistical properties of the density field over scales between a few arc min to one degree, see for instance [203,195,16,224,303,196,249].

Note that in addition to the strong-lensing and weak-lensing effects discussed above, one can also use gravitational lensing effects in the intermediate regime for astrophysical purposes. For instance, galaxy–galaxy lensing (associated with the distortion of background galaxies by one or a few nearby foreground galaxies) allows one to probe the galactic dark matter halos. In this fashion, one can measure the galaxy virial mass as a function of luminosity, as well as possible dependencies on the environment [93]. Then, such observations can be used to constrain galaxy formation models. In this review, we shall focus on statistical weak-lensing studies.

Traditionally, the study of large scale structures has been done by analyzing galaxy catalogues. However, this method is plagued by the problem of the galaxy bias (i.e. the distribution of light may not exactly follow the distribution of mass). The advantage of weak lensing is its ability to probe directly the matter distribution, through the gravitational potential, which is much more easily related to theory. In this way, one does not need to involve less well-understood processes like galaxy or star formation.

In the last few years many studies have managed to detect cosmological shear in random patches of the sky [6,7,39,96, 97,115,114,145,156,187,223,227,301,302,313]. While early studies were primarily concerned with the detection of a non-zero weak lensing signal, present weak lensing studies are already putting constraints on cosmological parameters such as the matter density parameter Ω_m and the amplitude σ_8 of the power-spectrum of matter density fluctuations. These works also help to lift parameter degeneracies when used along with other cosmological probes such as Cosmic Microwave Background (CMB) observations. In combination with galaxy redshift surveys they can be used to study the bias associated with various galaxies which will be useful for galaxy formation scenarios thereby providing much needed clues to the galaxy formation processes. For cosmological purposes, perhaps most exciting is the possibility that weak lensing will determine the properties of the dominant contributor to the Universe's energy budget: Dark Energy. Indeed, the recent acceleration of the Universe detected from the magnitude–redshift relation of supernovae (SNeIa) occurs at too late redshifts to be probed by the CMB fluctuations. On the other hand, weak lensing surveys offer a detailed probe of the dynamics of the Universe at low redshifts $z < 3$. Thus weak lensing is among the best independent techniques to confirm this acceleration and to analyze in greater details the equation of state of this dark energy component which may open a window on new physics beyond the standard model (such as extra dimensions).

In this review we describe the recent progress that has been made and various prospects of future weak lensing surveys. We first describe in Section 2 the basic elements of the deflection of light rays by gravity and the various observables associated with cosmological weak gravitational lensing. In Section 3 we review the 2-point statistics of these observables (power-spectra and 2-point correlations) and the problem of mass reconstruction from observed shear maps. Next, we explain in Section 4 how the knowledge of the redshift of background sources can be used to improve constraints on theoretical cosmological models or to perform fully 3-dimensional analysis (3D weak lensing). Then, we describe in Section 5 how to extract further information from weak lensing surveys by studying higher-order correlations which can tighten the constraints on cosmological parameters or provide some information on non-Gaussianities associated with non-linear dynamics or primordial physics. We turn to the determination of weak lensing shear maps from actual observations of

Table 1
Notation for cosmological variables

Total matter density in units of critical density	Ω_m
Reduced cosmological constant	Ω_Λ
Reduced dark energy density	Ω_{de}
Mean comoving density of the Universe	$\bar{\rho}$
Hubble constant at present time	H_0
Hubble constant at present time in units of 100 km s^{-1} Mpc^{-1}	h
rms linear density contrast in a sphere of radius 8 h^{-1} Mpc	σ_8

Table 2
Notation for coordinates

Metric	$ds^2 = c^2 dt^2 - a^2(t)[d\chi^2 + \mathcal{D}^2(d\theta^2 + \sin^2\theta\, d\varphi^2)]$
Speed of light	c
Scale factor	a
Comoving radial coordinate	χ, r
Comoving angular diameter distance	$\mathcal{D}$
Comoving position in 3D real space	$\mathbf{x}, \mathbf{r}, (\chi, \mathcal{D}\vec{\theta})$
Comoving wavenumber in 3D Fourier space	$\mathbf{k}, (k_\parallel, \vec{k}_\perp), (k_\parallel, \vec{\ell}/\mathcal{D})$
Bend angle	$\vec{\alpha}$
Deflection angle	$\delta\vec{\theta}$
Image position on the sky	$\vec{\theta}$
Flat-sky angle	(θ_1, θ_2)
2D angular wavenumber	$\vec{\ell}, (\ell_x, \ell_y), (\ell_1, \ell_2)$

Table 3
Notation for fields and weak-lensing variables

Gravitational potential	Φ
Lensing potential	ϕ
Shear matrix	Ψ
Amplification matrix	$\mathcal{A}$
Weak-lensing convergence	κ
Complex weak-lensing shear	$\gamma = \gamma_1 + i\gamma_2$
Shear pseudo-vector	$\vec{\gamma} = \gamma_1\vec{e}_x + \gamma_2\vec{e}_y$
Tangential component of shear	γ_t, γ_+
Cross component of shear	$\gamma_\times$
Weak-lensing magnification	μ
Angular filter radius	θ_s
Smoothed convergence, smoothed shear	$\bar{\kappa}, \bar{\gamma}$
Weak-lensing aperture mass	M_{ap}
3D matter density power spectrum	$P(k)$
2D convergence power spectrum	$P_\kappa(\ell)$
2D shear power spectrum	$P_\gamma(\ell)$
Two-point correlation	ξ
3D density contrast bispectrum	$B(k_1, k_2, k_3)$
2D convergence bispectrum	$B_\kappa(\ell_1, \ell_2, \ell_3)$
Probability distribution function of the smoothed convergence	$\mathcal{P}_\kappa(\bar{\kappa})$

galaxy images and to the correction techniques which have been devised to this order in Section 6. In Section 7 we discuss the numerical simulations which are essential to compare theoretical predictions with observational data. We describe in Section 8 how weak lensing surveys can also be performed at other wavelengths than the common optical range, using for instance the 21 cm emission of first generation protogalaxies as distant sources. We present in greater detail the weak lensing distortion of the CMB radiation in Section 9. In Section 10 we also discuss how weak lensing can be combined or cross-correlated with other data sets, such as the CMB or galaxy surveys, to help constrain cosmological models or derive some information on the matter distribution (e.g. mass-to-light relationships). Finally, we conclude in Section 11. To help the reader, we also give in Tables 1–3 our notations for most coordinate systems and variables used in this review.

2. Weak lensing theory

2.1. Deflection of light rays

We briefly describe here the basic idea behind weak gravitational lensing as we present a simple heuristic derivation of the first-order result for the deflection of light rays by gravity. For a rigorous derivation using General Relativity the reader can consult references [154,16,237,256].
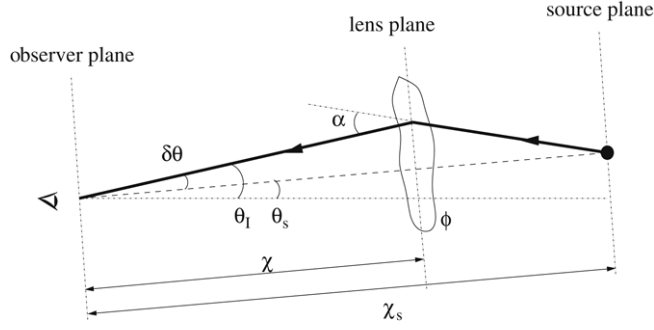
Fig. 1. Deflection of light rays from a distant source at comoving radial distance χ_s by a gravitational potential fluctuation Φ at distance χ. For a thin lens the deflection by the angle α is taken as instantaneous. This changes the observed position of the source by the angle $\delta\theta$, from the intrinsic source direction θ_s to the image direction θ_I on the sky.

We assume in the following that deflections angles are small so that we only consider first-order terms. This is sufficient for most applications of weak lensing since by definition the latter corresponds to the case of small perturbations of light rays by the large-scale structures of the universe. Let us consider within Newtonian theory the deflection of a photon with velocity **v** that passes through a small region of space where the gravitational potential Φ is non-zero. The acceleration perpendicular to the unperturbed trajectory, $\dot{\vec{v}}_\perp = -\nabla_\perp \Phi$, yields a small transverse velocity $\vec{v}_\perp = -\int dt \nabla_\perp \Phi$. This gives a deflection angle $\vec{\alpha} = \vec{v}_\perp / c = -\int dl \nabla_\perp \Phi / c^2$ for a constant velocity $|\mathbf{v}| = c$. As is well-known, General Relativity simply yields this Newtonian result multiplied by a factor two. This deflection changes the observed position on the sky of the radiation source by a small angle $\delta\vec{\theta}$. For an extended source (e.g. a galaxy) this also leads to both a magnification and a shear of the image of the source from which one can extract some information on the gravitational potential Φ. If the deflection takes place within a small distance it can be taken as instantaneous which corresponds to the thin lens approximation (as in geometrical optics) as displayed in Fig. 1. Besides, in cosmology transverse distances are related to angles through the comoving angular diameter distance $\mathcal{D}$ given by:

$$\mathcal{D}(\chi) = \frac{c \sin_K \left(|1 - \Omega_m - \Omega_\Lambda|^{1/2} H_0 \, \chi/c \right)}{H_0 |1 - \Omega_m - \Omega_\Lambda|^{1/2}}, \tag{2.1}$$

where $\sin_K$ means the hyperbolic sine, sinh, if $(1 - \Omega_m - \Omega_\Lambda) > 0$, or sine if $(1 - \Omega_m - \Omega_\Lambda) < 0$; if $(1 - \Omega_m - \Omega_\Lambda) = 0$, then $\mathcal{D}(\chi) = \chi$ (case of a flat Universe). The radial comoving distance χ measured by a light ray which travels from a source at redshift z to the observer at $z = 0$ is given by:

$$\chi = \frac{c}{H_0} \int_0^z \frac{dz'}{\sqrt{\Omega_\Lambda + (1 - \Omega_m - \Omega_\Lambda)(1 + z')^2 + \Omega_m (1 + z')^3}}, \tag{2.2}$$

where z' is the redshift along the line of sight. Note that χ measures both a spatial coordinate distance and a travel time. Here we also introduced the Hubble constant H_0 and the cosmological parameters Ω_m (matter density parameter) and Ω_Λ (dark energy in the form of a cosmological constant). Therefore, the source appears to have moved in the source plane over a comoving distance $\mathcal{D}(\chi_s)\delta\vec{\theta} = -\mathcal{D}(\chi_s - \chi)\vec{\alpha}$ as can be seen from Fig. 1, where $\vec{\alpha}$ and $\delta\vec{\theta}$ are 2D vectors in the plane perpendicular to the unperturbed light ray. Summing up the deflections arising from all potential gradients between the observer and the source gives the total shift on the sky:

$$\delta\vec{\theta} = \vec{\theta}_I - \vec{\theta}_s = \frac{2}{c^2} \int_0^{\chi_s} d\chi \, \frac{\mathcal{D}(\chi_s - \chi)}{\mathcal{D}(\chi_s)} \, \nabla_\perp \Phi(\chi), \tag{2.3}$$

where $\vec{\theta}_s$ is the intrinsic position of the source on the sky and $\vec{\theta}_I$ is the observed position. However, generally we do not know the true position of the source but only the position of the observed image. Thus the observable quantities are not the displacements $\delta\vec{\theta}$ themselves but the distortions induced by these deflections. They are given at lowest order by the symmetric shear matrix Ψ_{ij} [148,16,138] which we define as:

$$\Psi_{ij} = \frac{\partial \delta\theta_i}{\partial \theta_{sj}} = \frac{2}{c^2} \int_0^{\chi_s} d\chi \, \frac{\mathcal{D}(\chi)\mathcal{D}(\chi_s - \chi)}{\mathcal{D}(\chi_s)} \, \nabla_i \nabla_j \Phi(\chi), \tag{2.4}$$

Eq. (2.4) follows from Eq. (2.3) if we note that a change of angle $d\vec{\theta}$ for the unperturbed light ray corresponds to a transverse distance $\mathcal{D}(\chi)d\vec{\theta}$ in the lens plane where the gravitational potential Φ produces the gravitational lensing. The reasoning presented above clearly shows that Eq. (2.4) uses the weak lensing approximation; the derivatives $\nabla_i \nabla_j \Phi(\chi)$ of

the gravitational potential are computed along the unperturbed trajectory of the photon. This assumes that the components of the shear tensor are small but the density fluctuations δ can be large [148]. We can also express the shear matrix Ψ_{ij} in terms of a lensing potential $\phi(\vec{\theta}; \chi_s)$ (also called the deflection potential) as:

$$\Psi_{ij} = \phi_{,ij} \quad \text{with} \quad \phi(\vec{\theta}; \chi_s) = \frac{2}{c^2} \int_0^{\chi_s} \mathrm{d}\chi \, \frac{\mathcal{D}(\chi_s - \chi)}{\mathcal{D}(\chi_s)\mathcal{D}(\chi)} \, \Phi(\chi, \mathcal{D}(\chi)\vec{\theta}). \tag{2.5}$$

The expression (2.5) is formally divergent because of the term $1/\mathcal{D}(\chi)$ near $\chi = 0$, but this only affects the monopole term which does not contribute to the shear matrix Ψ_{ij} (indeed derivatives with respect to angles yield powers of $\mathcal{D}$ as in Eq. (2.4)). Therefore, we may set the constant term to zero so that $\phi(\vec{\theta})$ is well defined. Eq. (2.5) clearly shows how the weak lensing distortions are related to the gravitational potential projected onto the sky and can be fully described at this order by the 2D lensing potential $\phi(\vec{\theta})$. Thus, in this approximation lensing by the 3D matter distribution from the observer to the redshift z_s of the source plane is equivalent to a thin lens plane with the same deflection potential $\phi(\vec{\theta})$. However, from the dependence of $\phi(\vec{\theta}; \chi_s)$ on the redshift z_s of the source plane we can recover the 3D matter distribution as discussed below in Section 4. Note that weak lensing effects grow with the redshift of the source as the line of sight is more extended. However, since distant galaxies are fainter and more difficult to observe weak lensing surveys mainly probe redshifts $z_s \sim 1$. On the other hand, this range of redshifts of order unity is of great interest in probing the dark energy component of the Universe. Next, one can also introduce the amplification matrix $\mathcal{A}$ of image flux densities which is simply given by the ratio of image areas, that is by the Jacobian:

$$\mathcal{A} = \frac{\partial \vec{\theta}_s}{\partial \vec{\theta}_I} = (\delta_{ij} + \Psi_{ij})^{-1} = \begin{pmatrix} 1 - \kappa - \gamma_1 & -\gamma_2 \\ -\gamma_2 & 1 - \kappa + \gamma_1 \end{pmatrix}, \tag{2.6}$$

which defines the *convergence* κ and the *complex shear* $\gamma = \gamma_1 + \mathrm{i}\,\gamma_2$. At linear order the convergence gives the magnification of the source as $\mu = [\det(\mathcal{A})]^{-1} \simeq 1 + 2\kappa$. The shear describes the area-preserving distortion of amplitude given by $|\gamma|$ and of direction given by its phase, see also Section 6.1 and Fig. 15. In general the matrix $\mathcal{A}$ also contains an antisymmetric part associated with a rotation of the image but this term vanishes at linear order as can be seen from Eq. (2.4). From Eq. (2.6) the convergence κ and the shear components γ_1, γ_2, can be written at linear order in terms of the shear tensor as:

$$\kappa = \frac{\Psi_{11} + \Psi_{22}}{2}, \quad \gamma = \gamma_1 + \mathrm{i}\,\gamma_2 \quad \text{with} \quad \gamma_1 = \frac{\Psi_{11} - \Psi_{22}}{2}, \gamma_2 = \Psi_{12}. \tag{2.7}$$

On the other hand, the gravitational potential, Φ, is related to the fluctuations of the density contrast, δ, by Poisson's equation:

$$\nabla^2 \Phi = \frac{3}{2} \Omega_m H_0^2 (1 + z) \, \delta \quad \text{with} \quad \delta(\mathbf{x}) = \frac{\rho(\mathbf{x}) - \overline{\rho}}{\overline{\rho}}, \tag{2.8}$$

where $\overline{\rho}$ is the mean density of the universe. Note that since the convergence κ and the shear components γ_i can be expressed in terms of the scalar lensing potential ϕ they are not independent. For instance, one can check from the first equations (2.5) and (2.7) that we have $\kappa_{,1} = \gamma_{1,1} + \gamma_{2,2}$ [151]. This allows one to derive consistency relations satisfied by weak lensing distortions (e.g. [247]) and deviations from these relations in the observed shear fields can be used to estimate the observational noise or systematics. Of course such relations also imply interrelations between correlation functions, see [249] and Section 3 below. For a rigorous derivation of Eqs. (2.4)–(2.7) one needs to compute the paths of light rays (null geodesics) through the perturbed metric of spacetime using General Relativity [154]. An alternative approach is to follow the distortion of the cross-section of an infinitesimal light beam [230,31,256,16]. Both methods give back the results (2.4)–(2.7) obtained in a heuristic manner above.

2.2. Convergence, shear and aperture mass

Thanks to the radial integration over χ in (2.4) gradients of the gravitational potential along the radial direction give a negligible contribution as compared with transverse fluctuations [148,138,174] since positive and negative fluctuations cancel along the line of sight. In other words, the radial integration selects Fourier radial modes of order $|k_\parallel| \sim H/c$ (inverse of cosmological distances over which the effective lensing weight $\hat{w}(\chi)$ varies, see Eq. (2.10) below) whereas transverse modes are of order $|\vec{k}_\perp| \sim 1/\mathcal{D}\theta_s \gg |k_\parallel|$ where $\theta_s \ll 1$ is the typical angular scale (a few arc min) probed by the weak-lensing observable. Therefore, within this small-angle approximation the 2D Laplacian (2.7) associated with κ can be expressed in terms of the 3D Laplacian (2.8) at each point along the line of sight. This yields for the convergence along a given line of sight up to z_s:

$$\kappa(z_s) \simeq \int_0^{\chi_s} \mathrm{d}\chi \, w(\chi, \chi_s)\delta(\chi) \quad \text{with} \quad w(\chi, \chi_s) = \frac{3\Omega_m H_0^2 \mathcal{D}(\chi)\mathcal{D}(\chi_s - \chi)}{2c^2 \mathcal{D}(\chi_s)}(1 + z). \tag{2.9}$$

Thus the convergence, κ, can be expressed very simply as a function of the density field; it is merely an average of the local density contrast along the line of sight. Therefore, weak lensing observations allow one to measure the projected density field κ on the sky (note that by looking at sources located at different redshifts one may also probe the radial direction). In

practice the sources have a broad redshift distribution which needs to be taken into account. Thus, the quantity of interest is actually:

$$\kappa = \int_0^\infty dz_s \, n(z_s) \kappa(z_s) = \int_0^{\chi_{max}} d\chi \, \hat{w}(\chi) \delta(\chi) \quad \text{with } \hat{w}(\chi) = \int_z^{z_{max}} dz_s \, n(z_s) \, w(\chi, \chi_s), \tag{2.10}$$

where $n(z_s)$ is the mean redshift distribution of the sources (e.g. galaxies) normalized to unity and z_{max} is the depth of the survey. Eq. (2.10) neglects the discrete effects due to the finite number of galaxies, which can be obtained by taking into account the discrete nature of the distribution $n(z_s)$. This gives corrections of order $1/N$ to higher-order moments of weak-lensing observables, where N is the number of galaxies within the field of interest. In practice N is much larger than unity (for a circular window of radius 1 arc min we expect $N > 100$ for the SNAP mission) therefore it is usually sufficient to work with Eq. (2.10).

In order to measure weak-lensing observables such as κ or the shear γ one measures for instance the brightness or the shape of galaxies located around a given direction $\vec{\theta}$ on the sky. Therefore, one is led to consider weak-lensing quantities smoothed over a non-zero angular radius θ_s around the direction $\vec{\theta}$. More generally, one can define any smoothed weak-lensing quantity $\bar{X}(\vec{\theta})$ from its angular filter $U_X(\Delta\vec{\theta})$ by:

$$\bar{X}(\vec{\theta}) = \int d\vec{\theta}' \, U_X(\vec{\theta}' - \vec{\theta}) \kappa(\vec{\theta}') = \int d\chi \, \hat{w} \int d\vec{\theta}' \, U_X(\vec{\theta}' - \vec{\theta}) \delta(\chi, \mathcal{D}\vec{\theta}'), \tag{2.11}$$

where $\vec{\theta}'$ is the angular vector in the plane perpendicular to the line of sight (we restrict ourselves to small angular windows) and $\mathcal{D}\vec{\theta}'$ is the two-dimensional vector of transverse coordinates. Thus, it is customary to define the smoothed convergence by a top-hat U_κ of angular radius θ_s but this quantity is not very convenient for practical purposes since it is easier to measure the ellipticity of galaxies (related to the shear γ) than their magnification (related to κ). This leads one to consider compensated filters $U_{M_{ap}}$ with polar symmetry which define the "aperture-mass" M_{ap}, that is with $\int d\vec{\theta} \, U_{M_{ap}}(\vec{\theta}) = 0$. Then M_{ap} can be expressed in terms of the tangential component γ_t of the shear [239] so that it is not necessary to build a full convergence map from observations:

$$M_{ap}(\vec{\theta}) \equiv \int d\vec{\theta}' U_{M_{ap}}(|\vec{\theta}' - \vec{\theta}|) \kappa(\vec{\theta}') = \int d\vec{\theta}' Q_{M_{ap}}(|\vec{\theta}' - \vec{\theta}|) \gamma_t(\vec{\theta}') \tag{2.12}$$

where we introduce [239]:

$$Q_{M_{ap}}(\theta) = -U_{M_{ap}}(\theta) + \frac{2}{\theta^2} \int_0^\theta d\theta' \, \theta' \, U_{M_{ap}}(\theta'). \tag{2.13}$$

Besides, the aperture-mass provides a useful separation between E and B modes, as discussed below in Section 3.3. The aperture mass has the advantage that it can be chosen to have compact support, so it can be calculated from observations of a finite area. It can also be tuned to remove the strong lensing regime, if desired, by choosing $U = $ constant within some radius, in which case Q is zero. Finally, U can be chosen to select a fairly narrow range in wavenumber space, which can aid power spectrum estimation. One can alternatively choose a matched filter to improve signal-to-noise measurements.

For analytical and data analysis purposes it is often useful to work in Fourier space. Thus, we write for the 3D matter density contrast $\delta(\mathbf{x})$ and the 2D lensing potential $\phi(\vec{\theta})$:

$$\delta(\mathbf{x}) = \int \frac{d\mathbf{k}}{(2\pi)^3} \, e^{-i\mathbf{k}.\mathbf{x}} \, \delta(\mathbf{k}) \quad \text{and} \quad \phi(\vec{\theta}) = \int \frac{d\vec{\ell}}{(2\pi)^2} \, e^{-i\vec{\ell}.\vec{\theta}} \, \phi(\vec{\ell}), \tag{2.14}$$

where we use a flat-sky approximation for 2D fields. This is sufficient for most weak lensing purposes where we consider angular scales of the order of 1–10 arc min, but we shall describe in Section 4.5 the more general expansion over spherical harmonics. From Eq. (2.5) and Poisson's equation (2.8) we obtain:

$$\phi(\vec{\ell}) = -2 \int d\chi \hat{w}(\chi) \int \frac{dk_\parallel}{2\pi} \, e^{-ik_\parallel \chi} \frac{1}{k^2 \mathcal{D}(\chi)^4} \, \delta\left(k_\parallel, \frac{\vec{\ell}}{\mathcal{D}(\chi)}; \chi\right), \tag{2.15}$$

where $k_\parallel$ is the component parallel to the line of sight of the 3D wavenumber $\mathbf{k} = (k_\parallel, \vec{k}_\perp)$, with $\vec{k}_\perp = \vec{\ell}/\mathcal{D}$, and $\delta(\mathbf{k}; \chi)$ is the matter density contrast in Fourier space at redshift $z(\chi)$. The weight $\hat{w}(\chi)$ along the line of sight was defined in Eqs. (2.9) and (2.10). Then, from Eq. (2.7) we obtain for the convergence κ:

$$\kappa(\vec{\ell}) = -\frac{1}{2}(\ell_x^2 + \ell_y^2) \, \phi(\vec{\ell}) \simeq \int d\chi \frac{\hat{w}(\chi)}{\mathcal{D}^2} \int \frac{dk_\parallel}{2\pi} \, e^{-ik_\parallel \chi} \, \delta\left(k_\parallel, \frac{\vec{\ell}}{\mathcal{D}(\chi)}; \chi\right). \tag{2.16}$$

In the last expression we used as for Eq. (2.9) Limber's approximation $k^2 \simeq k_\perp^2$ as the integration along the line of sight associated with the projection on the sky suppresses radial modes as compared with transverse wavenumbers (i.e. $|k_\parallel| \ll k_\perp$). In a similar fashion, we obtain from Eq. (2.7) for the complex shear γ:

$$\gamma(\vec{\ell}) = -\frac{1}{2}(\ell_x + i\ell_y)^2 \, \phi(\vec{\ell}) = \frac{\ell_x^2 - \ell_y^2 + 2i\ell_x\ell_y}{\ell_x^2 + \ell_y^2} \, \kappa(\vec{\ell}) = e^{i2\alpha} \, \kappa(\vec{\ell}), \tag{2.17}$$

where α is the polar angle of the wavenumber $\vec{\ell} = (\ell_x, \ell_y)$. This expression clearly shows that the complex shear γ is a spin-2 field: it transforms as $\gamma \to \gamma\, e^{-i2\psi}$ under a rotation of transverse coordinates axis of angle ψ. This comes from the fact that an ellipse transforms into itself through a rotation of $180°$ and so does the shear which measures the area-preserving distortion, see Fig. 15.

For smoothed weak-lensing observables $\bar{X}$ as defined in Eq. (2.11) we obtain:

$$\bar{X}(\vec{\ell}) = W_X(-\vec{\ell}\theta_s)\kappa(\vec{\ell}) \qquad \text{with } W_X(\vec{\ell}\theta_s) = \int d\vec{\theta}\, e^{i\vec{\ell}.\vec{\theta}} U_X(\vec{\theta}), \tag{2.18}$$

where we introduced the Fourier transform W_X of the real-space filter U_X of angular scale θ_s. This gives for the convergence and the shear smoothed with a top-hat of angular radius θ_s:

$$W_\kappa(\vec{\ell}\theta_s) = \frac{2J_1(\ell\theta_s)}{\ell\theta_s}, \qquad W_\gamma(\vec{\ell}\theta_s) = W_\kappa(\ell\theta_s)\, e^{i2\alpha}, \tag{2.19}$$

where J_1 is the Bessel function of the first kind of order 1. In real space this gives back (with $\theta = |\vec{\theta}|$):

$$U_\kappa(\vec{\theta}) = \frac{\Theta(\theta_s - \theta)}{\pi\theta_s^2}, \qquad U_\gamma(\vec{\theta}) = -\frac{\Theta(\theta - \theta_s)}{\pi\theta^2}\, e^{i2\beta}, \tag{2.20}$$

where Θ is the Heaviside function and β is the polar angle of the angular vector $\vec{\theta}$. Note that Eq. (2.20) clearly shows that the smoothed convergence is an average of the density contrast over the cone of angular radius θ_s whereas the smoothed shear can be written as an average of the density contrast outside of this cone.

One drawback of the shear components is that they are even quantities (their sign can be changed through a rotation of axis, see Eq. (2.17)), hence their third-order moment vanishes by symmetry and one must measure the fourth-order moment $\langle\bar{\gamma}_i^4\rangle$ (i.e. the kurtosis) in order to probe the deviations from Gaussianity. Therefore it is more convenient to use the aperture-mass defined in Eq. (2.12) which can be derived from the shear but is not even, so that deviations from Gaussianity can be detected through the third-order moment $\langle M_{ap}^3\rangle$. A simple example is provided by the pair of filters [239]:

$$U_{M_{ap}}(\vec{\theta}) = \frac{\Theta(\theta_s - \theta)}{\pi\theta_s^2}\, 9\left(1 - \frac{\theta^2}{\theta_s^2}\right)\left(\frac{1}{3} - \frac{\theta^2}{\theta_s^2}\right), \tag{2.21}$$

and:

$$W_{M_{ap}}(\vec{\ell}\theta_s) = \frac{24J_4(\ell\theta_s)}{(\ell\theta_s)^2}. \tag{2.22}$$

An alternative approach was taken by [63], who chose a filter matched to the expected profile of galaxy clusters, to improve the signal-to-noise.

2.3. Approximations

The derivation of Eq. (2.4) does not assume that the density fluctuations δ are small but it assumes that deflection angles $\delta\vec{\theta}$ are small so that the relative deflection Ψ_{ij} of neighboring light rays can be computed from the gravitational potential gradients along the unperturbed trajectory (Born approximation). This may not be a good approximation for individual light beams, but in cosmological weak-lensing studies considered in this review one is only interested in the statistical properties of the gravitational lensing distortions. Since the statistical properties of the tidal field Φ_{ij} are, to an excellent approximation, identical along the perturbed and unperturbed paths, the use of Eq. (2.4) is well-justified to compute statistical quantities such as the correlation functions of the shear field [148,21].

Apart from the higher-order corrections to the Born approximation discussed above (multiple lens couplings), other higher-order terms are produced by the observational procedure. Indeed, in Eq. (2.10) we neglected the fluctuations of the galaxy distribution $n(z_s)$ which can be coupled to the matter density fluctuations along the line of sight. This source–lens correlation effect is more important as the overlapping area between the distributions of sources and lenses increases. On the other hand, source density fluctuations themselves can lead to spurious small-scale power (as the average distance to the sources can vary with the direction on the sky). Using analytical methods Ref. [23] found that both these effects are negligible for the skewness and kurtosis of the convergence provided the source redshift dispersion is less than about 0.15. These source clustering effects were further discussed in [95] who found that numerical simulations agree well with semi-analytical estimates and that the amplitude of such effects strongly depends on the redshift distribution of the sources. A recent study of the source–lens clustering [75], using numerical simulations coupled to realistic semi-analytical models for the distribution of galaxies, finds that this effect can bias the estimation of σ_8 by 2%–5%. Therefore, accurate photometric redshifts will be needed for future missions such as SNAP or LSST to handle this effect.

3. Statistics of 2D cosmic shear

For statistical analysis of cosmic shear, it is most common to use 2-point quantities, i.e. those which are quadratic in the shear, and calculated either in real or harmonic space. For this section, we will restrict the discussion to 2D fields, where we consider the statistics of the shear pattern on the sky only, and not in 3D. The shear field will be treated as a 3D field in Section 4. Examples of real-space 2-point statistics are the average shear variance and various shear correlation functions. In general there are advantages for cosmological parameter estimation in using harmonic-space statistics, as their correlation properties are more convenient, but for surveys with complicated geometry, such as happens with removal of bright stars and artifacts, there can be practical advantages to using real-space measures, as they can be easier to estimate. All the 2-point statistics can be related to the underlying 3D matter power spectrum via the (2D) convergence power spectrum $P_\kappa(\ell)$, and inspection of the relationship between the two point statistic and $P_\kappa(\ell)$ can be instructive, as it shows which wavenumbers are picked out by each statistic. In general, a narrow window in ℓ space may be desirable if the power spectrum is to be estimated.

3.1. Convergence and shear power spectra

We define the power spectra $P(k)$ of the 3D matter density contrast and $P_\kappa(\ell)$ of the 2D convergence as:

$$\langle \delta(\mathbf{k}_1)\delta(\mathbf{k}_2)\rangle = (2\pi)^3 \delta_D(\mathbf{k}_1 + \mathbf{k}_2)P(k_1) \tag{3.1}$$

and:

$$\langle \kappa(\vec{\ell}_1)\kappa(\vec{\ell}_2)\rangle = (2\pi)^2 \delta_D(\vec{\ell}_1 + \vec{\ell}_2)P_\kappa(\ell_1). \tag{3.2}$$

The Dirac functions δ_D express statistical homogeneity whereas statistical isotropy implies that $P(\mathbf{k})$ and $P_\kappa(\vec{\ell})$ only depend on $k = |\mathbf{k}|$ and $\ell = |\vec{\ell}|$. In Eq. (3.2) we used a flat-sky approximation which is sufficient for most weak-lensing purposes. We shall discuss in Section 4 the expansion over spherical harmonics (instead of plane waves as in Eq. (3.2)) which is necessary for instance for full-sky studies. Then, from Eqs. (2.16) and (2.17) we obtain:

$$P_\kappa(\ell) = P_\gamma(\ell) = \frac{1}{4}\ell^4 P_\phi(\ell) \tag{3.3}$$

and:

$$P_\kappa(\ell) = \int_0^\chi d\chi' \frac{\hat{w}^2(\chi')}{\mathcal{D}^2(\chi')} P\left(\frac{\ell}{\mathcal{D}(\chi')}; \chi'\right). \tag{3.4}$$

Thus this expression gives the 2D convergence power spectrum in terms of the 3D matter power spectrum $P(k; \chi)$ integrated along the line of sight, using Limber's approximation.

3.2. 2-point statistics in real space

As an example of a real-space 2-point statistic, consider the *shear variance*, defined as the variance of the average shear $\bar{\gamma}$ evaluated in circular patches of varying radius θ_s. The averaging is a convolution, so the power is multiplied (see Eqs. (2.18) and (2.19)):

$$\langle |\bar{\gamma}|^2 \rangle = \int \frac{d\ell}{2\pi} \ell P_\kappa(\ell) \frac{4J_1^2(\ell\theta_s)}{(\ell\theta_s)^2}, \tag{3.5}$$

where J_n is a Bessel function of order n.

The *shear correlation functions* can either be defined with reference to the coordinate axes,

$$\xi_{ij}(\theta) \equiv \langle \gamma_i(\vec{\theta}')\gamma_j(\vec{\theta}' + \vec{\theta})\rangle \tag{3.6}$$

where $i, j = 1, 2$ and the averaging is done over pairs of galaxies separated by angle $\theta = |\vec{\theta}|$. By parity $\xi_{12} = 0$, and by isotropy ξ_{11} and ξ_{22} are functions only of $|\vec{\theta}|$. The correlation function of the complex shear is

$$\langle \gamma\gamma^* \rangle_\theta = \int \frac{d^2\ell}{(2\pi)^2} P_\gamma(\ell)\, e^{i\vec{\ell}.\vec{\theta}}$$

$$= \int \frac{\ell d\ell}{(2\pi)^2} P_\kappa(\ell) e^{i\ell\theta\cos\varphi} d\varphi$$

$$= \int \frac{d\ell}{2\pi} \ell P_\kappa(\ell) J_0(\ell\theta). \tag{3.7}$$

Alternatively, the shears may be referred to axes oriented tangentially (t) and at $45°$ to the radius ($\times$), defined with respect to each pair of galaxies used in the averaging. The rotations $\gamma \to \gamma' = \gamma\, e^{-2i\psi}$, where ψ is the position angle of the pair, give
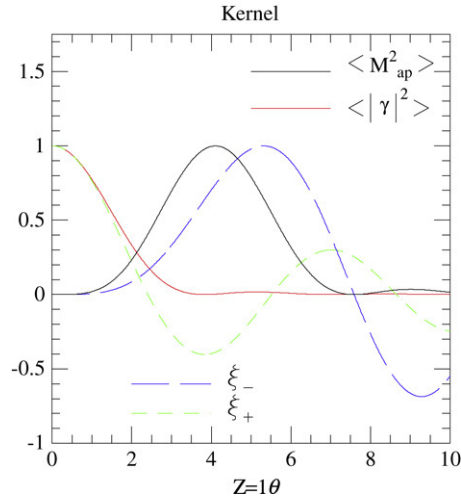
Fig. 2. Kernel functions for the two-point statistics discussed in this section. $z = \ell\theta_s$. The thin solid line peaking at $z = 0$ corresponds with the shear variance, the thick solid line is the aperture mass, with filter given in Eq. (2.21), the short dashed line is the kernel for ξ_+ and the long dashed to ξ_-.

tangential and cross components of the rotated shear as $\gamma' = -\gamma_t - i\gamma_\times$, where the components have correlation functions ξ_{tt} and $\xi_{\times\times}$ respectively. It is common to define a pair of correlations

$$\xi_\pm(\theta) = \xi_{tt} \pm \xi_{\times\times}, \tag{3.8}$$

which can be related to the convergence power spectrum by (see [148])

$$\xi_+(\theta) = \int_0^\infty \frac{d\ell}{2\pi} \ell P_\kappa(\ell) J_0(\ell\theta)$$
$$\xi_-(\theta) = \int_0^\infty \frac{d\ell}{2\pi} \ell P_\kappa(\ell) J_4(\ell\theta). \tag{3.9}$$

Finally, let us consider the class of statistics referred to as *aperture masses* associated with *compensated filters*, which we defined in Eq. (2.12). This allows M_{ap} to be related to the tangential shear [239] as in Eq. (2.12). Several forms of $U_{M_{ap}}$ have been suggested, which trade locality in real space with locality in ℓ space. Ref. [242] considers the filter $U_{M_{ap}}$ of Eq. (2.21) which cuts off at some scale, θ_s. From Eq. (2.22) this gives a two-point statistic

$$\langle M_{ap}^2(\theta_s) \rangle = \int \frac{d\ell}{2\pi} \ell P_\kappa(\ell) \frac{576 J_4^2(\ell\theta_s)}{(\ell\theta_s)^4}. \tag{3.10}$$

Other forms have been suggested [60], which are broader in real space, but pick up a narrower range of ℓ power for a given θ. As we have seen, all of these two-point statistics can be written as integrals over ℓ of the convergence power spectrum $P_\kappa(\ell)$ multiplied by some kernel function, since weak-lensing distortions can be expressed in terms of the lensing potential ϕ, see Eqs. (2.5) and (2.16).

If one wants to estimate the matter power spectrum, then there are some advantages in having a narrow kernel function, but the uncertainty principle then demands that the filtering is broad on the sky. This can lead to practical difficulties in dealing with holes, edges etc. Filter functions for the 2-point statistics mentioned here are shown in Fig. 2.

3.3. E/B decomposition

Weak gravitational lensing does not produce the full range of locally linear distortions possible. These are characterised by translation, rotation, dilation and shear, with six free parameters. Translation is not readily observable, but weak lensing is specified by three parameters rather than the four remaining degrees of freedom permitted by local affine transformations. This restriction is manifested in a number of ways: for example, the transformation of angles involves a 2×2 matrix which is symmetric, so not completely general, see Eq. (2.6). Alternatively, a general spin-weight 2 field can be written in terms of second derivatives of a *complex* potential, whereas the lensing potential is real. As noticed below Eq. (2.8) and in Eq. (3.25), this also implies that there are many other consistency relations which have to hold if lensing is responsible for the observed shear field. In practice the observed ellipticity field may not satisfy the expected relations, if it is contaminated by distortions not associated with weak lensing. The most obvious of these is optical distortions of the telescope system, but could also involve physical effects such as intrinsic alignment of galaxy ellipticities, which we will consider in Section 4.

A convenient way to characterise the distortions is via E/B decomposition, where the shear field is described in terms of an 'E-mode', which is allowed by weak lensing, and a 'B-mode', which is not. These terms are borrowed from similar
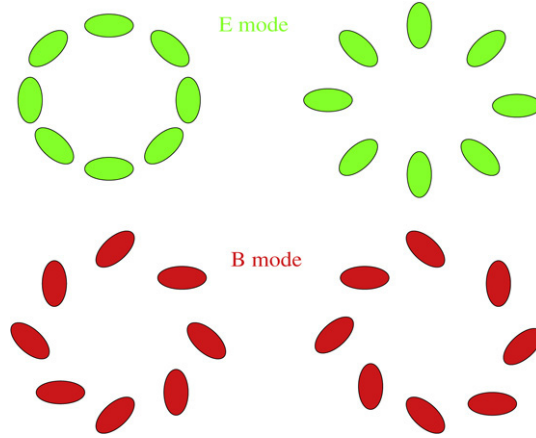
Fig. 3. Illustrative E and B modes: the E modes show what is expected around overdensities (left) and underdensities (right). The B mode patterns should not be seen (from van Waerbeke and Mellier [303]).
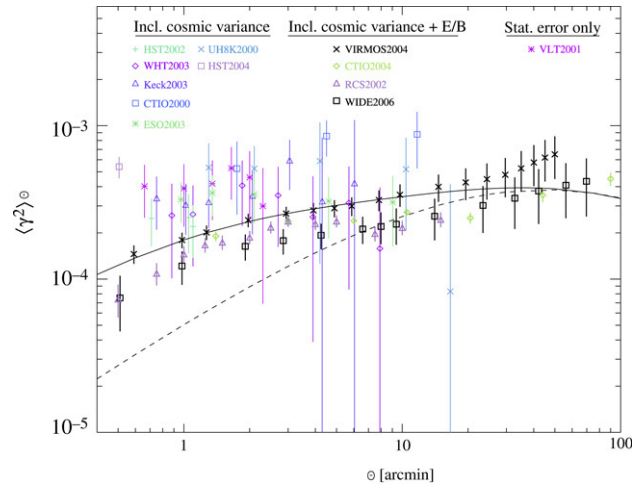

Fig. 4. Compilation of most of the shear measurements listed in Table 4. The vertical axis is the shear top-hat variance multiplied by the angular scale in arcminutes. The horizontal axis is the radius of the smoothing window in arcminutes. The positioning along the y-axis is only approximate given that the different surveys have a slightly different source redshift distribution. The RCS result (mean source redshift of 0.6) was rescaled to a mean source redshift of one.

decompositions in polarisation fields. In fact weak lensing can generate B-modes, but they are expected to be very small [245], so the existence of a significant B-mode in the observed shear pattern is indicative of some non-lensing contamination. Illustrative examples of E- and B-modes are shown in Fig. 3 (from [303]). The easiest way to introduce a B-mode mathematically is to make the lensing potential complex:

$$\phi = \phi_E + i\phi_B. \tag{3.11}$$

There are various ways to determine whether a B-mode is present. A neat way is to generalise the aperture mass to a complex $M = M_{ap} + iM_{\perp}$, where the real part picks up the E modes, and the imaginary part the B modes. Alternatively, the $\xi_{\pm}$ can be used [60,246]:

$$P_{\kappa\pm}(\ell) = \pi \int_0^\infty d\theta\, \theta \left[J_0(\ell\theta)\xi_+(\theta) \pm J_4(\ell\theta)\xi_-(\theta) \right], \tag{3.12}$$

where the $\pm$ power spectra refer to E and B mode powers. In principle this requires the correlation functions to be known over all scales from 0 to ∞. Variants of this [60] allow the E/B-mode correlation functions to be written in terms of integrals of $\xi_{\pm}$ over a finite range:

$$\begin{aligned}
\xi_E(\theta) &= \frac{1}{2}\left[\xi_-(\theta) + \xi'_+(\theta)\right] \\
\xi_B(\theta) &= -\frac{1}{2}\left[\xi_-(\theta) - \xi'_+(\theta)\right],
\end{aligned} \tag{3.13}$$

where

$$\xi'_+(\theta) = \xi_+(\theta) + 4 \int_0^\theta \frac{\mathrm{d}\vartheta}{\vartheta} \xi_+(\vartheta) - 12\theta^2 \int_0^\theta \frac{\mathrm{d}\vartheta}{\vartheta^3} \xi_+(\vartheta). \tag{3.14}$$

This avoids the need to know the correlation functions on large scales, but needs the observed correlation functions to be extrapolated to small scales; this was one of the approaches taken in the analysis of the CFHTLS data [120]. Difficulties with estimating the correlation functions on small scales have led others to prefer to extrapolate to large scales, such as in the analysis of the GEMS [104] and William Herschel data [190]. Note that without full sky coverage, the decomposition into E and B modes is ambiguous, although for scales much smaller than the survey it is not an issue.

3.4. Estimators and their covariance

The most common estimate of the cosmic shear comes from measuring the ellipticities of individual galaxies. We will consider the practicalities in Section 6. For weak gravitational lensing, these estimates are very noisy, since the galaxies as a population have intrinsic ellipticities e_S with a dispersion of about 0.4, whereas the typical cosmic shear is around $\gamma \simeq 0.01$. Therefore, one needs a large number N of galaxies to decrease the noise $\sim e_S/\sqrt{N}$ associated with these intrinsic ellipticities (hence one needs to observe the more numerous faint galaxies). The observed ellipticity is related to the shear by [238]

$$e_S = \frac{e - 2g + g^2 e^*}{1 + g^2 - 2\mathrm{Re}(ge^*)}, \tag{3.15}$$

where $g = \gamma/(1 - \kappa)$ is the reduced shear. Here we defined the ellipticity e such that for an elliptical image of axis ratio $r < 1$ we have:

$$|e| = \frac{1 - r^2}{1 + r^2}. \tag{3.16}$$

Other definitions are also used in the literature such as $|e'| = (1 - r)/(1 + r)$, see [249]. To linear order in γ or κ, we obtain from Eq. (3.15):

$$e \simeq e_S + 2\gamma, \tag{3.17}$$

with a small correction term when averaged. e is therefore dominated by the intrinsic ellipticity, and many source galaxies are needed to get a robust measurement of cosmic shear. This results in estimators of averaged quantities, such as the average shear in an aperture, or a weighted average in the case of M_{ap}. Any analysis of these quantities needs to take account of their noise properties, and more generally in their covariance properties. We will look only at a couple of examples here; a more detailed discussion of covariance of estimators, including non-linear cumulants, appears in [208].

3.4.1. Linear estimators
Perhaps the simplest average statistic to use is the average (of N) galaxy ellipticities in a 2D aperture on the sky:

$$\bar{\gamma} \equiv \frac{1}{N} \sum_{i=1}^N \frac{e_i}{2}. \tag{3.18}$$

The covariance of two of these estimators $\bar{\gamma}_\alpha$ and $\bar{\gamma}_\beta^*$ is

$$\langle \bar{\gamma}_\alpha \bar{\gamma}_\beta^* \rangle = \frac{1}{4NM} \sum_{i=1}^N \sum_{j=1}^M \langle (e_{Si} + 2\gamma_i)(e_{Sj}^* + 2\gamma_j^*) \rangle, \tag{3.19}$$

where the apertures have N and M galaxies respectively. If we assume (almost certainly incorrectly; see Section 4.7) that the source ellipticities are uncorrelated with each other, and with the shear, then for distinct apertures the estimator is an unbiased estimator of the shear correlation function averaged over the pair separations. If the apertures overlap, then this is not the case. For example, in the shear variance, the apertures are the same, and

$$\langle |\bar{\gamma}^2| \rangle = \frac{1}{N^2} \sum_{i=1}^N \sum_{j=1}^N \left\langle \frac{|e_{Si}|^2}{4} \delta_{ij} + \gamma_i \gamma_j^* \right\rangle, \tag{3.20}$$

which is dominated by the presence of the intrinsic ellipticity variance, $\sigma_e^2 \equiv \langle |e_S|^2 \rangle \simeq 0.3^2 - 0.4^2$. The average shear therefore has a variance of $\sigma_e^2/4N$. If we use the (quadratic) shear variance itself as a statistic, then it is estimated by omitting the diagonal terms:

$$|\bar{\gamma}^2| = \frac{1}{4N(N-1)} \sum_{i=1}^N \sum_{j \neq i} e_i e_j^*. \tag{3.21}$$

For aperture masses Eq. (2.12), the intrinsic ellipticity distribution leads to a shot noise term from the finite number of galaxies. Again we simplify the discussion here by neglecting correlations of source ellipticities. The shot noise can be calculated by the standard method [217] of dividing the integration solid angle into cells i of size $\Delta^2\theta_i$ containing $n_i = 0$ or 1 galaxy:

$$M_{\mathrm{ap}} \simeq \sum_i \Delta^2\theta_i\, n_i\, Q(|\vec{\theta}_i|)\, (e_{Si}/2 + \gamma_i)_t. \tag{3.22}$$

Squaring and taking the ensemble average, noting that $\langle e_{Si,t} e_{Sj,t}\rangle = \sigma_e^2 \delta_{ij}/2$, $n_i^2 = n_i$, and rewriting as a continuous integral gives

$$\langle M_{\mathrm{ap}}^2\rangle_{SN} = \frac{\sigma_e^2}{8} \int \mathrm{d}^2\theta\, Q^2(|\vec{\theta}|). \tag{3.23}$$

Shot noise terms for other statistics are calculated in similar fashion. In addition to the covariance from shot noise, there can be signal covariance, for example from samples of different depths in the same area of sky; both samples are affected by the lensing by the common low-redshift foreground structure [209].

3.4.2. Quadratic estimators

We have already seen how to estimate in an unbiased way the shear variance. The shear correlation functions can similarly be estimated:

$$\hat{\xi}_{\pm}(\theta) = \frac{\displaystyle\sum_{ij} w_i w_j (e_{it} e_{jt} \pm e_{i\times} e_{j\times})}{4 \displaystyle\sum_{ij} w_i w_j}, \tag{3.24}$$

where the w_i are arbitrary weights, and the sum extends over all pairs of source galaxies with separations close to θ. Only in the absence of intrinsic correlations, $\langle e_{it} e_{jt} \pm e_{i\times} e_{j\times}\rangle = \sigma_e^2 \delta_{ij} + 4\xi_{\pm}(|\vec{\theta}_i - \vec{\theta}_j|)$, are these estimators unbiased. The variance of the shear $\langle|\bar{\gamma}|^2\rangle$ and of the aperture-mass $\langle M_{\mathrm{ap}}^2\rangle$ can also be obtained from the shear correlation functions (as may be seen for instance from Eq. (3.10)). This avoids the need to place circular apertures on the sky which is hampered by the gaps and holes encountered in actual weak lensing surveys.

As with any quadratic quantity, the covariance of these estimators depends on the 4-point function of the source ellipticities and the shear. These expressions can be evaluated if the shear field is assumed to be Gaussian, but the expressions for this (and the squared aperture mass covariance) are too cumbersome to be given here, so the reader is directed to [246]. At small angular scales (below $\sim10'$), which are sensitive to the non-linear regime of gravitational clustering, the fields can no longer be approximated as Gaussian and one must use numerical simulations to calibrate the non-Gaussian contributions to the covariance, as described in [262].

In harmonic space, the convergence power spectrum may be estimated from either ξ_+ or ξ_- (or both), using Eq. (3.9). From the orthonormality of the Bessel functions,

$$P_\kappa(\ell) = \int_0^\infty \mathrm{d}\theta\, \theta\, \xi_{\pm}(\theta) J_{0,4}(\ell\theta), \tag{3.25}$$

where the 0, 4 correspond to the $+/-$ cases. In practice, $\xi_{\pm}(\theta)$ is not known for all θ, and the integral is truncated on both small and large scales. This can lead to inaccuracies in the estimation of $P_\kappa(\ell)$ (see [246]). An alternative method is to parametrise $P_\kappa(\ell)$ in band-powers, and to use parameter estimation techniques to estimate it from the shear correlation functions [124,38].

3.4.3. 2-point statistics measurement

Since the first measurements of weak lensing by large scale structures [299,6,313,156], all ideas discussed above have been put in practice on real data. Fig. 4 shows the measurement of shear top-hat variance as function of scale. This figure clearly shows that even early weak lensing measurement succeeded in capturing the non-linear matter clustering at scales below 10–20 arc min. Some groups performed a E/B separation, which leads to a more accurate measurement of residual systematics. Table 4 shows all measurements of the mass power spectrum σ_8 until 2006. It is interesting to note, except for COMBO-17 [104], none of the measurements are using a source redshift distribution obtained from the data, they all use the Hubble Deep Fields with different prescriptions regarding galaxy weighing. Ref. [304] have shown that the Hubble Deep Field photometric redshift distribution can lead to a source mean redshift error of $\sim10\%$ due to sample variance. The relative tension between different measures of σ_8 in Table 4 comes in part from this problem, and also from an uncertainty regarding how to treat the residual systematics, the B-mode, in the cosmic shear signal. Recently, [134] have released the largest photometric redshift catalogue, obtained from the CFHTLS-DEEP data. The most recent 2-point statistics analysis involves the combination of this photometric redshift sample with the largest weak lensing surveys described in Table 4. One of those analysis combines the largest lensing surveys to date [19] totalling a sky area of 100 deg^2, comprising deep and shallow surveys. The other analysis cover the most recent CFHTLS WIDE survey; it is uniform in depth and gives the first

Table 4
Reported constraints on the power spectrum normalization "σ_8" for $\Omega_m = 0.3$ for a flat Universe, obtained from a given "statistic" (from [303] and extended)

ID	$\sigma_8(\Omega = 0.3)$	Statistic	Field	$m_{\lim}$	CosVar	E/B	z_s	Γ
Maoli et al. 01	1.03 ± 0.05	$\langle \gamma^2 \rangle$	VLT + CTIO + WHT + CFHT	–	No	No	–	0.21
Van Waerbeke et al. 01	0.88 ± 0.11	$\langle \gamma^2 \rangle, \xi(r),$ $\langle M_{\rm ap}^2 \rangle$	CFHT 8 deg^2.	$I = 24.5$	No	No (yes)	1.1	0.21
Rhodes et al. 01	$0.91^{+0.25}_{-0.29}$	$\xi(r)$	HST 0.05 deg^2	$I = 26$	Yes	No	0.9–1.1	0.25
Hoekstra et al. 02 [116]	0.81 ± 0.08	$\langle \gamma^2 \rangle$	CFHT + CTIO 24 deg^2.	$R = 24$	Yes	No	0.55	0.21
Bacon et al. 03	0.97 ± 0.13	$\xi(r)$	Keck + WHT 1.6 deg^2	$R = 25$	Yes	No	0.7–0.9	0.21
Réfrégier et al. 02	0.94 ± 0.17	$\langle \gamma^2 \rangle$	HST 0.36 deg^2.	$I = 23.5$	Yes	No	0.8–1.0	0.21
Van Waerbeke et al. 02	0.94 ± 0.12	$\langle M_{\rm ap}^2 \rangle$	CFHT 12 deg^2.	$I = 24.5$	Yes	Yes	0.78–1.08	0.1–0.4
Hoekstra et al. 02	$0.91^{+0.05}_{-0.12}$	$\langle \gamma^2 \rangle, \xi(r),$ $\langle M_{\rm ap}^2 \rangle$	CFHT + CTIO 53 deg^2.	$R = 24$	Yes	Yes	0.54–0.66	0.05–0.5
Brown et al. 03	0.74 ± 0.09	$\langle \gamma^2 \rangle, \xi(r)$	COMBO17 1.25 deg^2.	$R = 25.5$	Yes	No (Yes)	0.8–0.9	–
Hamana et al. 03	$(2\sigma)0.69^{+0.35}_{-0.25}$	$\langle M_{\rm ap}^2 \rangle, \xi(r)$	Subaru 2.1 deg^2.	$R = 26$	Yes	Yes	0.8–1.4	0.1–0.4
Jarvis et al. 03	$(2\sigma)0.71^{+0.12}_{-0.16}$	$\langle \gamma^2 \rangle, \xi(r),$ $\langle M_{\rm ap}^2 \rangle$	CTIO 75 deg^2.	$R = 23$	Yes	Yes	0.66	0.15–0.5
Rhodes et al. 04	1.02 ± 0.16	$\langle \gamma^2 \rangle, \xi(r)$	STIS 0.25 deg^2.	$\langle I \rangle = 24.8$	Yes	No	1.0 ± 0.1	–
Heymans et al. 05	0.68 ± 0.13	$\langle \gamma^2 \rangle, \xi(r)$	GEMS 0.3 deg^2.	$\langle m_{606} \rangle = 25.6$	Yes	No (Yes)	~ 1	–
Massey et al. 05	1.02 ± 0.15	$\langle \gamma^2 \rangle, \xi(r)$	WHT 4 deg^2.	$R = 25.8$	Yes	Yes	~ 0.8	–
Van Waerbeke et al. 05	0.83 ± 0.07	$\langle \gamma^2 \rangle, \xi(r)$	CFHT 12 deg^2.	$I = 24.5$	Yes	No (Yes)	0.9 ± 0.1	0.1–0.3
Heitterscheidt et al. 06	0.8 ± 0.1	$\langle \gamma^2 \rangle, \xi(r)$	GaBoDS 13 deg^2.	$R = [21.5, 24.5]$	Yes	Yes	~ 0.78	$h \in [0.63, 0.77]$
Semboloni et al. 06	0.90 ± 0.14	$\langle M_{\rm ap}^2 \rangle, \xi(r)$	CFHTLS-DEEP 2.3 deg^2.	$i = 25.5$	Yes	Yes	~ 1	$\Gamma = \Omega h$
Hoekstra et al. 06	0.85 ± 0.06	$\langle \gamma^2 \rangle, \xi(r),$ $\langle M_{\rm ap}^2 \rangle$	CFHTLS-WIDE 22 deg^2.	$i = 24.5$	Yes	Yes	0.8 ± 0.1	$\Gamma = \Omega h$
Benjamin et al. 07	0.74 ± 0.04	$\xi(r)$	Various 100 deg^2	Various	Yes	Yes	0.78	$\Gamma \simeq \Omega h$
Fu et al. 08	0.70 ± 0.04	$\langle \gamma^2 \rangle, \xi(r),$ $\langle M_{\rm ap}^2 \rangle$	CFHTLS-WIDE 57 deg^2.	$i = 24.5$	Yes	Yes	0.95	$\Gamma \simeq \Omega h$

"CosVar" tells us whether or not the cosmic variance has been included, "E/B" tells us whether or not a mode decomposition has been used in the likelihood analysis. z_s and Γ are the priors used for the different surveys identified with "ID".

measurement of cosmic shear at large angular scale (Fu et al. [78]). The former finds $\sigma_8 \left(\frac{\Omega_m}{0.24} \right)^{0.59} = 0.84 \pm 0.05$ and the latter $\sigma_8 \left(\frac{\Omega_m}{0.25} \right)^{0.64} = 0.785 \pm 0.043$. The relative tension is gone, as nicely illustrated in Fig. 5 and tends to favor a relatively low normalisation when combined with the cosmic microwave background WMAP3 data $\sigma_8 = 0.77 \pm 0.03$ (Fu et al. [78]). One can reasonably argue that the major uncertainty remains the calibration of the source redshift distribution [19], Fu et al. [78], which strongly suggests that a photometric redshift measurement of all galaxies used in weak lensing measurements must be a priority for future surveys. The systematics due to the Point Spread Function correction (see Section 6) seems to be much better understood than a few years ago, and many promising techniques have been proposed to solve it.

3.5. Mass reconstruction

The problem of mass reconstruction is a central topic in weak lensing. Historically this is because the early measurements of weak gravitational lensing were obtained in clusters of galaxies, and this led to the very first maps of dark matter [33,74]. These maps were the very first demonstrations that we could *see* the dark side of the Universe without any assumption regarding the light–mass relation, which, of course, was a major breakthrough in our exploration of the Universe. Reconstructing mass maps is also the only way to perform a complete comparison of the dark matter distribution to the Universe as seen in other wavelengths. For these reasons, mass reconstruction is also part of the shear measurement process. A recent example of the power of mass reconstruction is shown by the *bullet cluster* [47,34], which clearly indicates the presence of dark matter at a location different from where most of the baryons are. This is a clear demonstration that, at least for the extreme cases where light and baryons do not trace the mass, weak lensing is the only method that can probe the matter distribution.

A mass map is a convergence, κ map (projected mass), which can be reconstructed from the shear field γ_i:

$$\kappa = \frac{1}{2} \left(\partial_x^2 + \partial_y^2 \right) \phi; \qquad \gamma_1 = \frac{1}{2} \left(\partial_x^2 - \partial_y^2 \right) \phi; \qquad \gamma_2 = \partial_x \partial_y \phi, \qquad (3.26)$$

where ϕ is the projected gravitational potential [148], see Eqs. (2.5)–(2.7). Assuming that the reduced shear and shear are equal to first approximation, i.e. $g_i \simeq \gamma_i$ (which is true only in the weak lensing regime when $|\gamma| \ll 1$ and $\kappa \ll 1$), [149]
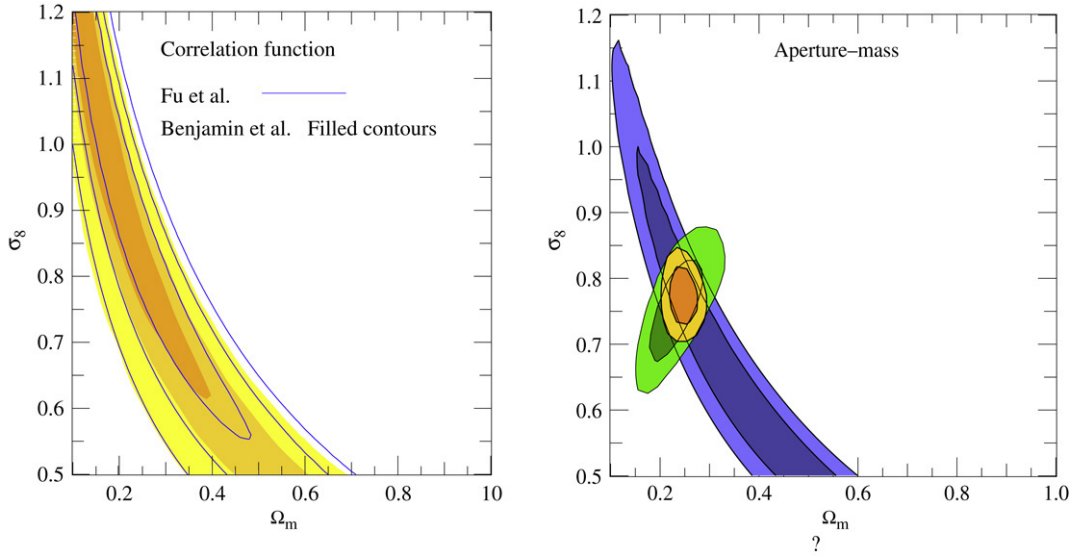
Fig. 5. Left panel: combined Ω_m and σ_8 constraints from [19] and [78] who have only 30% of data in common (a fraction of CFHTLS wide data); shear correlation function was used. Right panel: lensing constraints from the aperture mass measurement in [78] combined with WMAP3. Courtesy Liping Fu.

have shown that the Fourier transform of the smoothed convergence $\bar{\kappa}(\vec{\ell})$ can be obtained from the Fourier transform of the smoothed shear map $\bar{\gamma}(\vec{\ell})$:

$$\bar{\kappa}(\vec{\ell}) = \frac{\ell_x^2 + \ell_y^2}{\ell_x^2 - \ell_y^2 + 2i\ell_x\ell_y} \bar{\gamma}(\vec{\ell}). \tag{3.27}$$

This follows from Eq. (2.17) if smoothing is a convolution as in Eq. (2.11) which is expressed in Fourier space as a product, see Eq. (2.18). This relation explicitly shows that mass reconstruction must be performed with a given smoothing window, otherwise the variance of the mass map becomes infinite [149]. Indeed, the random galaxy intrinsic ellipticities e_{Si} introduce a white noise which gives a large-ℓ divergence when we transform back to real space for the variance $\langle \bar{\kappa}^2 \rangle_c$. The Fourier transform method is a fast $N \log N$ process, but the non-linear regions $\kappa \sim \gamma_i \sim 1$ are not accurately reconstructed. A likelihood reconstruction method works in the intermediate and strong lensing regimes [13]. A χ^2 function of the reduced shear g_i is minimised by finding the best gravitational potential ϕ_{ij} calculated on a grid ij:

$$\chi^2 = \sum_{ij} \left[\left| g_{ij}^{\text{obs}} - g_{ij}^{\text{guess}}(\phi_{ij}) \right|^2 \right]. \tag{3.28}$$

The shot noise of the reconstructed mass map depends on the smoothing window, the intrinsic ellipticity of the galaxies and the number density of galaxies [298]. The two methods outlined above provide an accurate description of the shot noise: it was shown [297] that two and three-points statistics can be measured accurately from reconstructed mass maps using these methods (see Fig. 6). Important for cluster lensing, the non-linear version of [149] has been developed in [153], and [238] have developed an alternative which also conserves the statistical properties of the noise. The advantage of a reconstruction method that leaves intact the shot noise is that a statistical analysis of the mass map is relatively straightforward (e.g. the peak statistics in [139]). Mass reconstruction has proven to be reasonably successful in blind cluster searches [204,48,80]. A radically different approach in map making consists in reducing the noise in order to identify the highest signal-to-noise peaks. Such an approach has been developed by [257,36,189]. More recently [273] proposed a wavelet approach, where the size of the smoothing kernel is optimized as a function of the local noise amplitude. An application of this method on the COSMOS data for cluster detection is shown in [192].

Mass maps are essential for some specific cosmological studies such as morphology analysis like Minkowski functionals and Euler characteristics [233] and for global statistics (probability distribution function of the convergence, e.g. [320]). The reconstruction processes is non local, and this is why it is difficult to have a perfect control of the error propagation and systematics in the κ maps. In particular, note that one can only reconstruct the convergence κ up to a constant κ_0, since Eq. (3.27) is undetermined for $\ell = 0$. Indeed, a constant matter surface density in the lens plane does not create any shear (since it selects no preferred direction) but it leads to a non-zero constant convergence (which may only be eliminated if we observe a wide-enough field where the mean convergence should vanish, or use complementary information such as number counts which are affected by the associated magnification). This is the well-known mass-sheet degeneracy. The aperture mass statistics M_{ap} [150,242] introduced in Eq. (2.12) has been invented to enforce locality of the mass reconstruction, therefore it might provide an alternative to the inversion problem, although it is not yet clear that it can achieve a signal-to-noise as good as top-hat or Gaussian smoothing windows.
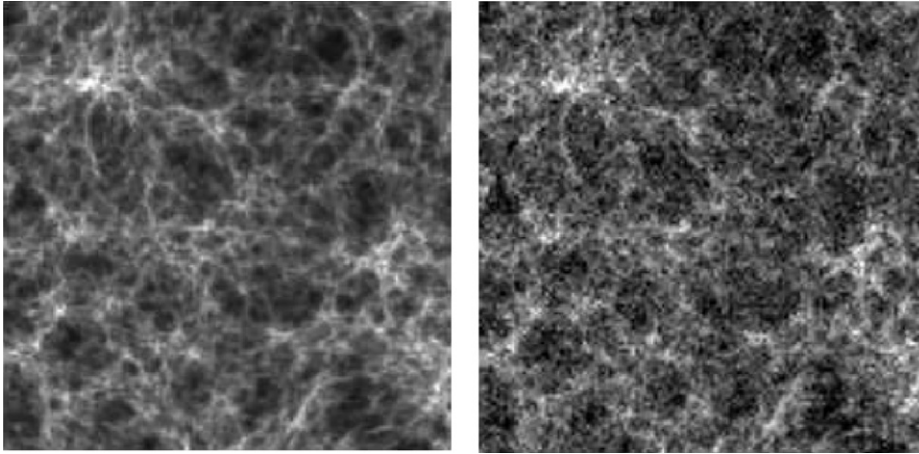
Fig. 6. Left: Simulated noise-free κ map. Field-of-view is 49 square degrees in LCDM cosmology. Right: Reconstructed κ field with realistic noise level (give details). Van Waerbeke et al. [297] have shown that two and three-point statistics can be accurately measured from such mass reconstructions.

The aperture mass statistic can also be used to provide unbiased estimates of the power spectrum [14], galaxy biasing [296,233], high order statistics [242,300], and peak statistics [102].

4. 3D weak lensing

4.1. What is 3D weak lensing?

The way in which weak lensing surveys have been analysed to date has been to look for correlations of shapes of galaxies on the sky; this can be done even if there is no distance information available for individual sources. However, as we have seen, the interpretation of observed correlations depends on where the imaged galaxies are: the more distant they are, the greater the correlation of the images. One therefore needs to know the statistical distribution of the source galaxies, and ignorance of this can lead to relatively large errors in recovered parameters. In order to rectify this, most lensing surveys obtain multi-colour photometry of the sources, from which one can estimate their redshifts. These 'photometric redshifts' are not as accurate as spectroscopic redshifts, but the typical depth of survey required by lensing surveys makes spectroscopy an impractical option for large numbers of sources. 3D weak lensing uses the distance information of *individual* sources, rather than just the *distribution* of distances. If one has an estimate of the distance to each source galaxy, then one can utilise this information and investigate lensing in three dimensions. Essentially one has an estimate of the shear field at a number of discrete locations in 3D.

There are several ways 3D information can be used: one is to reconstruct the 3D gravitational potential or the overdensity field from 3D lensing data. We will look at this in Section 4.2. The second is to exploit the additional statistical power of 3D information, firstly by dividing the sources into a number of shells based on estimated redshifts. One then essentially performs a standard lensing analysis on each shell, but exploits the extra information from cross-correlations between shells. This sort of analysis is commonly referred to as tomography, and we explore this in Section 4.3, and in Section 4.4, where one uses ratios of shears behind clusters of galaxies. Finally, one can perform a fully-3D analysis of the estimated shear field. Each approach has its merits. We cover 3D statistical analysis in Section 4.5. At the end of Section 4.7, we investigate how photometric redshifts can remove a potentially important physical systematic: the intrinsic alignment of galaxies, which could be wrongly interpreted as a shear signal. Finally, in Section 4.8, we consider a potentially very important systematic error arising from a correlation between cosmic shear and the intrinsic alignment of foreground galaxies, which could arise if the latter responds to the local tidal gravitational field which is partly responsible for the shear.

4.2. 3D potential and mass reconstruction

As we have already seen, it is possible to reconstruct the surface density of a lens system by analysing the shear pattern of galaxies in the background. An interesting question is then whether the reconstruction can be done in three dimensions, when distance information is available for the sources. It is probably self-evident that mass distributions can be *constrained* by the shear pattern, but the more interesting possibility is that one may be able to *determine* the 3D mass density in an essentially non-parametric way from the shear data.

The idea [284] is that the shear pattern is derivable from the lensing potential $\phi(\mathbf{r})$, which is dependent on the gravitational potential $\Phi(\mathbf{r})$ through the integral equation

$$\phi(\mathbf{r}) = \frac{2}{c^2} \int_0^r dr' \left(\frac{1}{r'} - \frac{1}{r} \right) \Phi(\mathbf{r}'), \tag{4.1}$$

where the integral is understood to be along a radial path (the Born approximation), and a flat Universe is assumed in Eq. (4.1). The gravitational potential is related to the density field via Poisson's Eq. (2.8). There are two problems to solve here; one is to construct ϕ from the lensing data, the second is to invert Eq. (4.1). The second problem is straightforward: the solution is

$$\Phi(\mathbf{r}) = \frac{c^2}{2} \frac{\partial}{\partial r} \left[r^2 \frac{\partial}{\partial r} \phi(\mathbf{r}) \right]. \tag{4.2}$$

From this and Poisson's equation $\nabla^2 \Phi = (3/2)H_0^2 \Omega_m \delta/a(t)$, we can reconstruct the mass overdensity field

$$\delta(\mathbf{r}) = \frac{a(t)c^2}{3H_0^2 \Omega_m} \nabla^2 \left\{ \frac{\partial}{\partial r} \left[r^2 \frac{\partial}{\partial r} \phi(\mathbf{r}) \right] \right\}. \tag{4.3}$$

The construction of ϕ is more tricky, as it is not directly observable, but must be estimated from the shear field. This reconstruction of the lensing potential suffers from a similar ambiguity to the mass-sheet degeneracy for simple lenses. To see how, we first note that the complex shear field γ is the second derivative of the lensing potential:

$$\gamma(\mathbf{r}) = \left[\frac{1}{2} \left(\frac{\partial^2}{\partial x^2} - \frac{\partial^2}{\partial y^2} \right) + i \frac{\partial^2}{\partial x \partial y} \right] \phi(\mathbf{r}). \tag{4.4}$$

As a consequence, since the lensing potential is real, its estimate is ambiguous up to the addition of any field $f(\mathbf{r})$ for which

$$\frac{\partial^2 f(\mathbf{r})}{\partial x^2} - \frac{\partial^2 f(\mathbf{r})}{\partial y^2} = \frac{\partial^2 f(\mathbf{r})}{\partial x \partial y} = 0. \tag{4.5}$$

Since ϕ must be real, the general solution to this is

$$f(\mathbf{r}) = F(r) + G(r)x + H(r)y + P(r)(x^2 + y^2), \tag{4.6}$$

where F, G, H and P are arbitrary functions of $r \equiv |\mathbf{r}|$. Assuming these functions vary smoothly with r, only the last of these survives at a significant level to the mass density, and corresponds to a sheet of overdensity

$$\delta = \frac{4a(t)c^2}{3H_0^2 \Omega_m r^2} \frac{\partial}{\partial r} \left[r^2 \frac{\partial}{\partial r} P(r) \right]. \tag{4.7}$$

There are a couple of ways to deal with this problem. For a reasonably large survey, one can assume that the potential and its derivatives are zero on average, at each r, or that the overdensity has average value zero. For further details, see [7]. Note that the relationship between the overdensity field and the lensing potential is a linear one, so if one chooses a discrete binning of the quantities, one can use standard linear algebra methods to attempt an inversion, subject to some constraints such as minimising the expected reconstruction errors. With prior knowledge of the signal properties, this is the Wiener filter. See [129] for further details of this approach.

4.3. Tomography

In the case where one has distance information for individual sources, it makes sense to employ the information for statistical studies. A natural course of action is to divide the survey into slices at different distances, and perform a study of the shear pattern on each slice. In order to use the information effectively, it is necessary to look at cross-correlations of the shear fields in the slices, as well as correlations within each slice [121]. This procedure is usually referred to as tomography, although the term does not seem entirely appropriate.

We start by considering the average shear in a shell, which is characterised by a probability distribution for the source redshifts $z = z(r)$, $p(z)$. The shear field is the second edth derivative of the lensing potential, e.g. [41].

$$\gamma(\mathbf{r}) = \frac{1}{2} \eth \, \eth \, \phi(\mathbf{r}) \simeq \frac{1}{2} (\partial_x + i \partial_y)^2 \phi(\mathbf{r}), \tag{4.8}$$

where the derivatives are in the angular direction, and the last equality holds in the flat-sky limit. If we average the shear in a shell, giving equal weight to each galaxy, then the average shear can be written in terms of an effective lensing potential

$$\phi_{\mathrm{eff}}(\boldsymbol{\theta}) = \int_0^\infty \mathrm{d}z\, p(z) \phi(\mathbf{r}) \tag{4.9}$$

where the integral is at fixed $\boldsymbol{\theta}$, and $p(z)$ is zero outside the slice (we ignore errors in distance estimates such as photometric redshifts; these could be incorporated with a suitable modification to $p(z)$). In terms of the gravitational potential, the effective lensing potential is

$$\phi_{\mathrm{eff}}(\boldsymbol{\theta}) = \frac{2}{c^2} \int_0^\infty \mathrm{d}r\, \Phi(\mathbf{r}) g(r), \tag{4.10}$$
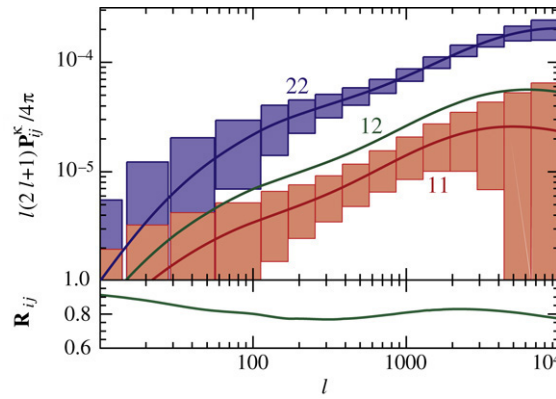
Fig. 7. The power spectra of two slices, their cross power spectrum, and their correlation coefficient. From [121].

where reversal of the order of integration gives the lensing efficiency to be

$$g(r) = \int_{z(r)}^{\infty} dz' \, p(z') \left(\frac{1}{r} - \frac{1}{r'} \right), \tag{4.11}$$

where $z' = z'(r')$ and we assume flat space. If we perform a spherical harmonic transform of the effective potentials for slices i and j, then the cross power spectrum can be related to the power spectrum of the gravitational potential $P_\Phi(k)$ via a version of Limber's equation:

$$\langle \phi_{\ell m}^{(i)} \phi_{\ell' m'}^{*(j)} \rangle = C_{\ell,ij}^{\phi\phi} \, \delta_{\ell'\ell} \delta_{m'm}, \tag{4.12}$$

where

$$C_{\ell,ij}^{\phi\phi} = \left(\frac{2}{c^2} \right)^2 \int_0^\infty dr \, \frac{g^{(i)}(r) g^{(j)}(r)}{r^2} \, P_\Phi(\ell/r; r) \tag{4.13}$$

is the cross power spectrum of the lensing potentials. The last argument in P_Φ allows for evolution of the power spectrum with time, or equivalently distance. The power spectra of the convergence and shear are related to $C_{\ell,ij}^{\phi\phi}$ by [122]

$$
\begin{aligned}
C_{\ell,ij}^{\kappa\kappa} &= \frac{\ell^2(\ell+1)^2}{4} \, C_{\ell,ij}^{\phi\phi} \\
C_{\ell,ij}^{\gamma\gamma} &= \frac{1}{4} \frac{(\ell+2)!}{(\ell-2)!} \, C_{\ell,ij}^{\phi\phi}.
\end{aligned}
\tag{4.14}
$$

The sensitivity of the cross power spectra to cosmological parameters is through various effects, as in 2D lensing: the shape of the linear gravitational potential power spectrum is dependent on some parameters, as is its nonlinear evolution; in addition the $z(r)$ relation probes cosmology. The reader is referred to standard cosmological texts for more details of the dependence of the distance–redshift relation on cosmological parameters.

Ref. [121] illustrates the power and limitation of tomography, with two shells (Fig. 7). As expected, the deeper shell (2) has a larger lensing power spectrum than the nearby shell (1), but it is no surprise to find that the power spectra from shells are correlated, since the light from both passes through some common material. Thus one does gain from tomography, but, depending on what one wants to measure, the gains may or may not be very much. For example, tomography adds rather little to the accuracy of the amplitude of the power spectrum, but far more to studies of dark energy properties. One also needs to worry about systematic effects, as leakage of galaxies from one shell to another, through noisy or biased photometric redshifts, can degrade the accuracy of parameter estimation [133,180].

4.4. The shear ratio test

The shear contributed by the general large-scale structure is typically about 1%, but the shear behind a cluster of galaxies can far exceed this. As always, the shear of a background source is dependent on its redshift, and on cosmology, but also on the mass distribution in the cluster. This can be difficult to model, so it is attractive to consider methods which are decoupled from the details of the mass distribution of the cluster. Various methods have been proposed (e.g. [140,29,319]). The method currently receiving the most attention is simply to take ratios of average tangential shear in different redshift slices for sources behind the cluster.

The amplitude of the induced tangential shear is dependent on the source redshift z, and on cosmology via the angular diameter distance–redshift relation $S_k[r(z)]$ by [285]

$$\gamma_t(z) = \gamma_t(z = \infty) \frac{S_k[r(z) - r(z_l)]}{S_k[r(z)]}, \tag{4.15}$$
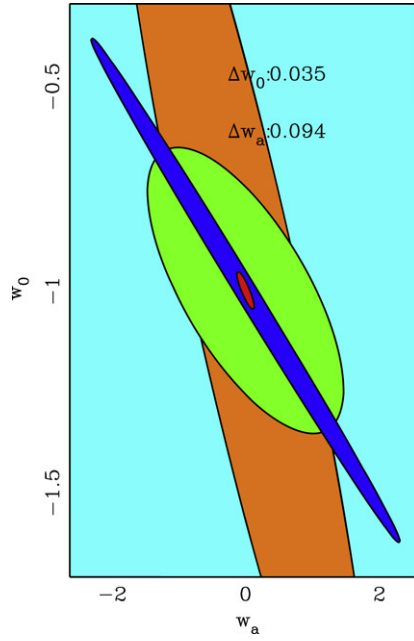
Fig. 8. The accuracy expected from the combination of experiments dedicated to studying dark energy properties. The equation of state of dark energy is assumed to vary with scale factor a as $w(a) = w_0 + w_a(1-a)$, and the figures show the 1-sigma, 2-parameter regions for the experiments individually and in combination. The supernova study fills the plot, the thin diagonal band is Planck, the near-vertical band is BAO, and the ellipse is the 3D lensing power spectrum method. The small ellipse is the expected accuracy from the combined experiments. From [100].
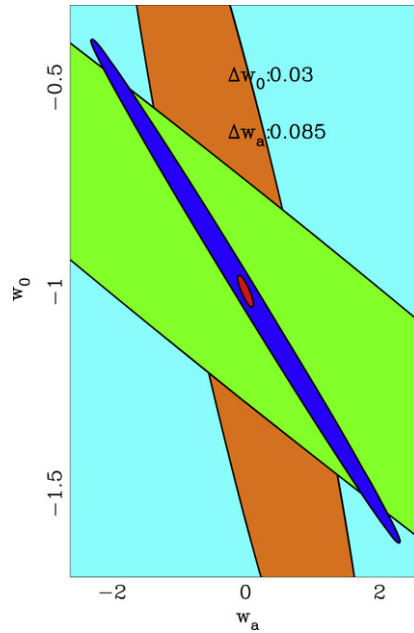

Fig. 9. As in Fig. 8, but with the shear ratio test as the lensing experiment. Supernovae fill the plot, Planck is the thin diagonal band, BAO the near-vertical band, and the shear ratio is the remaining 45° band. The combination of all experiments is in the centre. From [285].

where $\gamma_{t,\infty}$ is the shear which a galaxy at infinite distance would experience, and which characterises the strength of the distortions induced by the cluster, at redshift z_l. Evidently, we can neatly eliminate the cluster details by taking ratios of tangential shears, for pairs of shells in source redshift:

$$R_{ij} \equiv \frac{\gamma_{t,i}}{\gamma_{t,j}} = \frac{S_k[r(z_j)]\, S_k[r(z_i) - r(z_l)]}{S_k[r(z_i)]\, S_k[r(z_j) - r(z_l)]}. \tag{4.16}$$

In reality, the light from the more distant shell passes through an extra pathlength of clumpy matter, so suffers an additional source of shear. This can be treated as a noise term [285]. This approach is attractive in that it probes cosmology through the distance–redshift relation alone, being (at least to good approximation) independent of the growth rate of the fluctuations. Its dependence on cosmological parameters is therefore rather simpler, as many parameters (such as the amplitude of matter fluctuations) do not affect the ratio except through minor side-effects. More significantly, it can be used in conjunction with lensing methods which probe both the distance–redshift relation and the growth-rate of structure. Such a dual approach can in principle distinguish between quintessence-type dark energy models and modifications of Einstein gravity. This possibility arises because the effect on global properties (e.g. $z(r)$) is different from the effect on perturbed quantities (e.g. the growth rate of the power spectrum) in the two cases. The method has a signal-to-noise which is limited by the finite number of clusters which are massive enough to have measurable tangential shear. In an all-sky survey, the bulk of the signal would come from the 10^5–10^6 clusters above a mass limit of $10^{14} M_\odot$.

4.5. Full 3D analysis of the shear field

An alternative approach to take is to recognise that, with photometric redshift estimates for individual sources, the data one is working with is a very noisy 3D shear field, which is sampled at a number of discrete locations, and for whom the locations are somewhat imprecisely known. It makes some sense, therefore, to deal with the data one has, and to compare the statistics of the discrete 3D field with theoretical predictions. This was the approach of [99,41,100]. It should yield smaller statistical errors than tomography, as it avoids the binning process which loses information. Typical gains are a factor of 1.3 improvement in parameter errors.

In common with many other methods, one has to make a decision whether to analyse the data in configuration space or in the spectral domain. The former, usually studied via correlation functions, is advantageous for complex survey geometries, where the convolution with a complex window function implicit in spectral methods is avoided. However, the more readily computed correlation properties of a spectral analysis are a definite advantage for Bayesian parameter estimation, and we follow that approach here.

The natural expansion of a 3D scalar field (r, θ, ϕ) which is derived from a potential is in terms of products of spherical harmonics and spherical Bessel functions, $j_\ell(kr) Y_\ell^m(\boldsymbol\theta)$. Such products, characterised by 3 spectral parameters (k, ℓ, m), are eigenfunctions of the Laplace operator, thus making it very easy to relate the expansion coefficients of the density field to that of the potential (essentially via $-k^2$ from the ∇^2 operator). Similarly, the 3D expansion of the lensing potential,

$$\phi_{\ell m}(k) \equiv \sqrt{\frac{2}{\pi}} \int \mathrm{d}^3\mathbf{r}\, \phi(\mathbf{r}) k j_\ell(kr) Y_\ell^m(\boldsymbol\theta), \tag{4.17}$$

where the prefactor and the factor of k are introduced for convenience. The expansion of the complex shear field is most naturally made in terms of spin-weight 2 spherical harmonics $_2Y_\ell^m$ and spherical Bessel functions, since $\gamma = \frac{1}{2} \eth\,\eth\, \phi$, and $\eth\,\eth\, Y_\ell^m \propto {}_2Y_\ell^m$:

$$\gamma(\mathbf{r}) = \sqrt{2\pi} \sum_{\ell m} \int \mathrm{d}k\, \gamma_{\ell m}\, k j_\ell(kr)\, {}_2Y_\ell^m(\boldsymbol\theta). \tag{4.18}$$

The choice of the expansion becomes clear when we see that the coefficients of the shear field are related very simply to those of the lensing potential:

$$\gamma_{\ell m}(k) = \frac{1}{2} \sqrt{\frac{(\ell+2)!}{(\ell-2)!}}\, \phi_{\ell m}(k). \tag{4.19}$$

The relation of the $\phi_{\ell m}(k)$ coefficients to the expansion of the density field is readily computed, but more complicated as the lensing potential is a weighted integral of the gravitational potential. The details will not be given here, but relevant effects such as photometric redshift errors, nonlinear evolution of the power spectrum, and the discreteness of the sampling are easily included. The reader is referred to the original papers for details [99,41,100].

In this way the correlation properties of the $\gamma_{\ell m}(k)$ coefficients can be related to an integral over the power spectrum, involving the $z(r)$ relation, so cosmological parameters can be estimated via standard Bayesian methods from the coefficients. Clearly, this method probes the dark energy effect on both the growth rate and the $z(r)$ relation.

4.6. Parameter forecasts from 3D lensing methods

In this section we summarise some of the forecasts for cosmological parameter estimation from 3D weak lensing. We will explore this further in Section 10, but here concentrate on the statistical errors which should be achievable with the shear ratio test and with the 3D power spectrum techniques. Tomography should be similar to the latter. We show results from 3D weak lensing alone, as well as in combination with other experiments. These include CMB, supernova and baryon oscillation studies. The methods generally differ in the parameters which they constrain well, but also in terms of the degeneracies inherent in the techniques. Using more than one technique can be very effective at lifting the degeneracies, and very accurate

determinations of cosmological parameters, in particular dark energy properties, may be achievable with 3D cosmic shear surveys covering thousands of square degrees of sky to median source redshifts of order unity.

Figs. 8 and 9 show the accuracy which might be achieved with a number of surveys designed to measure cosmological parameters. We concentrate here on the capabilities of each method, and the methods in combination, to constrain the dark energy equation of state, and its evolution, parametrised by [46]

$$w(a) = \frac{p}{\rho c^2} = w_0 + w_a(1 - a),$$ (4.20)

where the behaviour as a function of scale factor a is, in the absence of a compelling theory, assumed to have this simple form. $w = -1$ would arise if the dark energy behaviour was actually a cosmological constant.

The assumed experiments are: a 5-band 3D weak lensing survey, analysed either with the shear ratio test, or with the spectral method, covering 10,000 deg^2 to a median redshift of 0.7, similar to the capabilities of a groundbased 4 m-class survey with a several square degree field; the Planck CMB experiment (14-month mission); a spectroscopic survey to measure baryon oscillations (BAO) in the galaxy matter power spectrum, assuming constant bias, and covering 2000 deg^2 to a median depth of unity, and a smaller $z = 3$ survey of 300 deg^2, similar to WFMOS capabilities on Subaru; a survey of 2000 Type Ia supernovae to $z = 1.5$, similar to SNAP's design capabilities.

We see that the experiments in combination are much more powerful than individually, as some of the degeneracies are lifted. Note that the combined experiments appear to have rather smaller error bars than is suggested by the single-experiment constraints. This is because the combined ellipse is the projection of the product of several multi-dimensional likelihood surfaces, which intersect in a small volume. (The projection of the intersection of two surfaces is not the same as the intersection of the projection of two surfaces.) The figures show that errors of a few percent on w_0 are potentially achievable, or, with this parametrisation, an error of w at a 'pivot' redshift of $z \simeq 0.4$ of under 0.02. This error is essentially the minor axis of the error ellipses.

4.7. Intrinsic alignments

The main signature of weak lensing is a small alignment of the images, at the level of a correlation of ellipticities of $\sim 10^{-4}$. One might be concerned that physical processes might also induce an alignment of the galaxies themselves. The possible effect is immediately apparent if one considers that the shear is often estimated from the ellipticity of a galaxy, which includes the intrinsic ellipticity of the source e_s:

$$e \simeq e_s + 2\gamma.$$ (4.21)

A useful statistic to consider is the shear correlation function, which would normally be estimated from the ellipticity correlation function:

$$\langle ee^* \rangle = 4\langle \gamma\gamma^* \rangle + \langle e_s e_s^* \rangle + 4\langle \gamma e^* \rangle.$$ (4.22)

This equation is schematic, referring either to galaxies separated by some angle on the sky, or by a 3D separation in the case of a 3D analysis. The first term is the cosmic signal one wishes to use; the second term is the *intrinsic alignment* signal, and the third is the *shear-intrinsic alignment* signal, which we will consider later. Until recently, both these additional terms were assumed to be zero. The hope was that even galaxies close together on the line of sight would typically be at such large physical separations that physical processes which could correlate the orientations would be absent. However, the lensing signal is very small, so the assumption that intrinsic alignment effects are sufficiently small needs to be tested. For the intrinsic alignment signal, this was first done in a series of papers by a number of groups in 2000–1 (e.g. [98,61,59,42]), and the answer is that the effect may not be negligible, and is expected to be strongly dependent on the depth of the survey. This is easy to see, since at fixed angular separation, galaxies in a shallow survey will be physically closer together in space, and hence more likely to experience tidal interactions which might align the galaxies. In addition to this, the shallower the survey, the smaller the lensing signal. In a pioneering study, the alignments of nearby galaxies in the SuperCOSMOS survey were investigated [38]. This survey is so shallow (median redshift ~ 0.1) that the expected lensing signal is tiny. A non-zero alignment was found, which agrees with at least some of the theoretical estimates of the effect. The main exception is the numerical study of [147], which predicts a contamination so high that it could dominate even deep surveys. For deep surveys, the consensus is that the effect is expected to be rather small, but if one wants to use weak lensing as a probe of subtle effects such as the effects of altering the equation of state of dark energy, then one cannot ignore it. There are essentially two options — either one tries to calculate the intrinsic alignment signal and subtract it, or one tries to remove it altogether. The former approach is not practical, as, although there is some agreement as to the general level of the contamination, the details are not accurately enough known. The latter approach is becoming possible, as lensing surveys are now obtaining estimates of the distance to each galaxy, via photometric redshifts (spectroscopic redshifts are difficult to obtain, because one needs a rather deep sample, with median redshift at least 0.6 or so, and large numbers, to reduce shot noise due to the random orientations of ellipticities). With photometric redshifts, one can downweight or completely remove physically close galaxies from the pair statistics (such as the shear correlation function) [103,161]. Thus one removes a systematic error in favour of a slightly increased statistical error. The analysis in [104] explicitly removed close pairs and shows that it can be done very successfully.

4.8. Shear-intrinsic alignment correlation

The cross term $\langle \gamma e^* \rangle$ was neglected entirely until [111] pointed out that it was not necessarily zero. The idea here is that the local tidal gravitational field contributes to the shear of background images, and if it also influenced the orientation of a galaxy locally, then it could induce correlations between foreground galaxies and background galaxies, even though they may be physically separated by gigaparsecs. This term is more problematic for cosmic shear studies, because it is not amenable to the simple solutions which work well for the intrinsic alignment signal. It is conceivable that this effect is the limiting systematic effect in cosmic shear studies, as it seems necessary actually to model it and remove it. Studies of the SDSS [184] measured a significant signal in a related statistic, for very luminous galaxies, and a study of N-body simulations supported the view that the effect was likely to be non-negligible, at the level of up to 10% of the cosmic shear signal. On a more positive note, it seems [111,162,106] that the term scales with source and lens angular diameter distances in proportion to the lensing efficiency $S_k(r_l) S_k(r_{ls})/S_k(r_s)$. This is reasonable, and also very useful, as it makes the parametrisation of the shear-intrinsic alignment much more straightforward. One can either use templates [162] or parametrise the contamination as a single function of separation, and marginalise over these nuisance parameters in the estimation of cosmological parameters. See also [37].

4.9. Summary

In this section, we have looked at the possible uses of 3D information to enhance what one can do with cosmic shear. We found that the 3D gravitational potential can be reconstructed, from which the 3D matter density field could be determined. In addition, statistical tests such as the 3D power spectrum method, or the shear ratio test, can determine cosmological parameters connected with dark energy which are difficult to estimate using other methods. We found that the combination of various different methods can be very powerful, with the equation of state of dark energy able to be determined to an accuracy of a few percent, in principle. We explored some of the physical systematics which might limit the lensing approach, in particular intrinsic alignments, whose contamination can be reduced to a negligible level if photometric redshift information is available. The limiting physical systematic is almost certain to be the shear-intrinsic alignment signal, which may account for as much as 10% of the cosmic shear signal, and which must be removed. Fortunately the specific redshift dependence of this term offers realistic prospects of determining it in conjunction with the cosmic shear signal.

5. Non-Gaussianities

The two-point statistics discussed in Section 3 can be used to constrain cosmological parameters. However, since they can be expressed in terms of the convergence power $P_\kappa(\ell)$ they mainly depend on the same combination of parameters. Thus, from Eq. (2.9) we can expect $\langle \bar\kappa^2 \rangle \sim \sigma_8^2 \Omega_m^2$ if we neglect the dependence on cosmology of comoving distances, where σ_8 is the normalization of the linear power-spectrum. A more careful analysis [21] actually gives the scaling of Eq. (10.1). In order to lift this degeneracy between the parameters Ω_m and σ_8 one can combine weak lensing observations with other cosmological probes such as the CMB, as we shall discuss in Section 10, or use 3D information as seen in Section 4 (e.g. Eq. (4.16)). An alternative procedure is to consider higher-order moments of weak lensing observables. Indeed, even if the initial conditions are Gaussian, since the dynamics is non-linear non-Gaussianities develop and in the non-linear regime the density field becomes strongly non-Gaussian (this is an unstable self-gravitating expanding system). This can be seen from the constraints $\langle \delta \rangle = 0$ and $\delta \geq -1$ (because the matter density $\rho = (1+\delta)\bar\rho$ is positive) which imply that in the highly non-linear regime ($\langle \delta^2 \rangle \gg 1$) the probability distribution of the density contrast δ must be far from Gaussian. Since weak gravitational lensing effects arise from the matter distribution (see Eq. (2.4)) high-order correlation functions of both the 3D density field and weak-lensing observables are non-zero and could be used to extract additional information.

5.1. Bispectrum and three-point functions

The three-point correlation function is the lowest-order statistics which can be used to detect non-Gaussianity. In Fourier space it is called the bispectrum which is defined as:

$$\langle \delta(\mathbf{k}_1)\delta(\mathbf{k}_2)\delta(\mathbf{k}_3) \rangle = (2\pi)^3 \delta_D(\mathbf{k}_1 + \mathbf{k}_2 + \mathbf{k}_3) B(k_1, k_2, k_3) \tag{5.1}$$

for the 3D matter density contrast, where the Dirac factor results from statistical homogeneity. Isotropy also implies that $B(k_1, k_2, k_3)$ only depends on the length of the three wavenumbers $\mathbf{k}_1$, $\mathbf{k}_2$, $\mathbf{k}_3$ or alternatively on two lengths k_1, k_2 and the angle α_{12} between both vectors. A key feature of the bispectrum (5.1) is that in the large-scale limit its dependence on the normalization of the power-spectrum can be factorized out [21]. Indeed, at large scales where the density contrast is much smaller than unity and quasi-linear perturbation theory is valid one can expand the density contrast as a perturbative series of the form:

$$\delta(\mathbf{k}, z) = \delta^{(1)}(\mathbf{k}, z) + \delta^{(2)}(\mathbf{k}, z) + \cdots, \tag{5.2}$$

where $\delta^{(q)}$ is of order q over the initial density field ($\delta^{(1)}$ is simply the linear density contrast δ_L). Then, substituting into the three-point function we obtain:

$$\langle \delta(\mathbf{k}_1)\delta(\mathbf{k}_2)\delta(\mathbf{k}_3) \rangle = \langle \delta^{(1)}(\mathbf{k}_1)\delta^{(1)}(\mathbf{k}_2)\delta^{(1)}(\mathbf{k}_3) \rangle + \langle \delta^{(2)}(\mathbf{k}_1)\delta^{(1)}(\mathbf{k}_2)\delta^{(1)}(\mathbf{k}_3) \rangle$$
$$+ \langle \delta^{(1)}(\mathbf{k}_1)\delta^{(2)}(\mathbf{k}_2)\delta^{(1)}(\mathbf{k}_3) \rangle + \langle \delta^{(1)}(\mathbf{k}_1)\delta^{(1)}(\mathbf{k}_2)\delta^{(2)}(\mathbf{k}_3) \rangle + \cdots, \tag{5.3}$$

where the dots stand for terms of order $(\delta^{(1)})^5$ and beyond. For Gaussian initial conditions the first term vanishes whereas the three other terms are of order $(\delta^{(1)})^4$ so that the quantity:

$$Q(k_1, k_2, k_3) = \frac{B(k_1, k_2, k_3)}{P(k_2)P(k_3) + P(k_1)P(k_3) + P(k_1)P(k_2)} \tag{5.4}$$

is independent of the normalization of the linear density power-spectrum $P_L(k)$ at large scales. In this manner one can separate the dependence on σ_8 from the dependence on other cosmological parameters. Using the small-angle approximation the $\vec{\ell}$-space three-point correlation of the convergence reads [26]:

$$\langle \kappa(\vec{\ell}_1)\kappa(\vec{\ell}_2)\kappa(\vec{\ell}_3) \rangle = (2\pi)^2 \delta_D(\vec{\ell}_1 + \vec{\ell}_2 + \vec{\ell}_3)B_\kappa(\ell_1, \ell_2, \ell_3), \tag{5.5}$$

with:

$$B_\kappa(\ell_1, \ell_2, \ell_3) = \int d\chi \, \frac{\hat{w}^3}{\mathcal{D}^4} \, B\left(\frac{\ell_1}{\mathcal{D}}, \frac{\ell_2}{\mathcal{D}}, \frac{\ell_3}{\mathcal{D}} \right). \tag{5.6}$$

Then, as in Eq. (5.4) one can consider ratios such as $B_\kappa(\ell_1, \ell_2, \ell_3)/(P_\kappa(l_2)P_\kappa(l_3) + \cdots)$ to lift the degeneracy between the parameters Ω_m and σ_8 [21]. Using tomography (i.e. redshift binning of the sources) also helps to constrain cosmological parameters such as the equation of state of the dark energy component, as studied in Ref. [280]. We display their results in Fig. 10 which shows that bispectrum tomography can improve parameter constraints significantly, typically by a factor of three, compared to just power spectrum tomography.

In practice, most of the angular range probed by weak lensing surveys is actually in the transition domain from the linear to highly non-linear regimes (from $10'$ down to $1'$). Therefore, it is important to have a reliable prediction for these mildly and highly non-linear scales, once the cosmology and the initial conditions are specified. Since there is no rigorous analytical framework to fully describe this regime numerical simulations play a key role in obtaining the non-linear evolution of the matter power spectrum and of higher-order statistics [214,271]. Based on these simulation results and analytical insight it is possible to build analytical models which can describe the low order moments of weak lensing observables such as the bispectrum [300]. Using a halo model as described in Appendix A.3, Refs. [278,279] investigated the real-space three-point correlation of the convergence $\langle \kappa(\vec{\theta}_1)\kappa(\vec{\theta}_2)\kappa(\vec{\theta}_3) \rangle$. They studied its dependence on the triangle geometry $(\vec{\theta}_1, \vec{\theta}_2, \vec{\theta}_3)$ and on the parameters of the halo model [278] and compared these predictions with numerical simulations [279].

As seen earlier it is more convenient for observational purposes to consider the shear rather than the convergence since it is the former which is directly measured (in fact what is actually measured is the reduced shear $\gamma/(1 - \kappa)$ which can be approximated by γ in the weak-lensing regime, [238]). However, since $\vec{\gamma}$ is a 2-component field there are many ways to combine shear triplets. Here we defined the shear spin-2 "vector" as $\vec{\gamma} = \gamma_1\vec{e}_x + \gamma_2\vec{e}_y$ where $\vec{e}_x, \vec{e}_y$ are the 2D basis vectors using the flat sky approximation which is valid for small angles (let us recall that $\vec{\gamma}$ is not truly a vector since its components change as $\cos(2\psi)$ and $\sin(2\psi)$ under a rotation of ψ of coordinate axis, as seen from Eq. (2.17)). Besides, one must take care not to define statistics which depend on the choice of the coordinate system. A possible approach is to consider scalar quantities such as the aperture mass M_{ap} which can be expressed both in terms of the convergence or shear fields. However, this may not be optimal from a signal-to-noise perspective since the integration over the window radius θ_s may dilute the cosmological signal as contributions from triangle configurations where the shear three-point function is positive or negative can partly cancel out. Moreover, the additional information contained in the detailed angular behavior of the shear three-point correlation can be useful to constrain cosmology and large-scale structures. Therefore, it is interesting to build estimators designed for the high-order correlations of the shear field.

One strategy investigated in [26] is to study the mean shear pattern $\vec{\gamma}(\vec{\theta})$ around a pair of points $\vec{\theta}_1, \vec{\theta}_2$ through the quantity $\langle \vec{\gamma}_3(\vec{\theta}) \rangle = \langle [\vec{\gamma}(\vec{\theta}_1).\vec{\gamma}(\vec{\theta}_2)]\vec{\gamma}(\vec{\theta}) \rangle$. This study, based on analytical results (using the behavior of the density three-point correlation in the quasi-linear regime and its simplest extension to smaller scales) and numerical simulations, shows that this mean shear is almost uniform, and perpendicular to $\vec{\theta}_{12}$, over an elliptic area that covers the segment $\vec{\theta}_{12}$ which joins both points. This suggests measuring the average of $\langle \vec{\gamma}_3(\vec{\theta}) \rangle$ over this ellipse so as to avoid cancellations. In this manner [25] managed to obtain from the VIRMOS-DESCART Lensing Survey the first detection of non-Gaussianities in a weak lensing survey. We display their results in Fig. 11 which shows that the amplitude and shape of the signal agree with theoretical predictions from numerical simulations. Although the measures are still too noisy to provide useful constraints on cosmology they show such weak-lensing observations to be a very promising tool. On the other hand, [27] also obtained explicit analytical expressions for the shear three-point correlations from the one-halo term which appears within halo models (when all points are assumed to lie within the same dark matter halo, see Appendix A.3) and recovered the pattern shown by numerical simulations. These results may serve as a guideline to build optimized estimators for the shear three-point correlations.
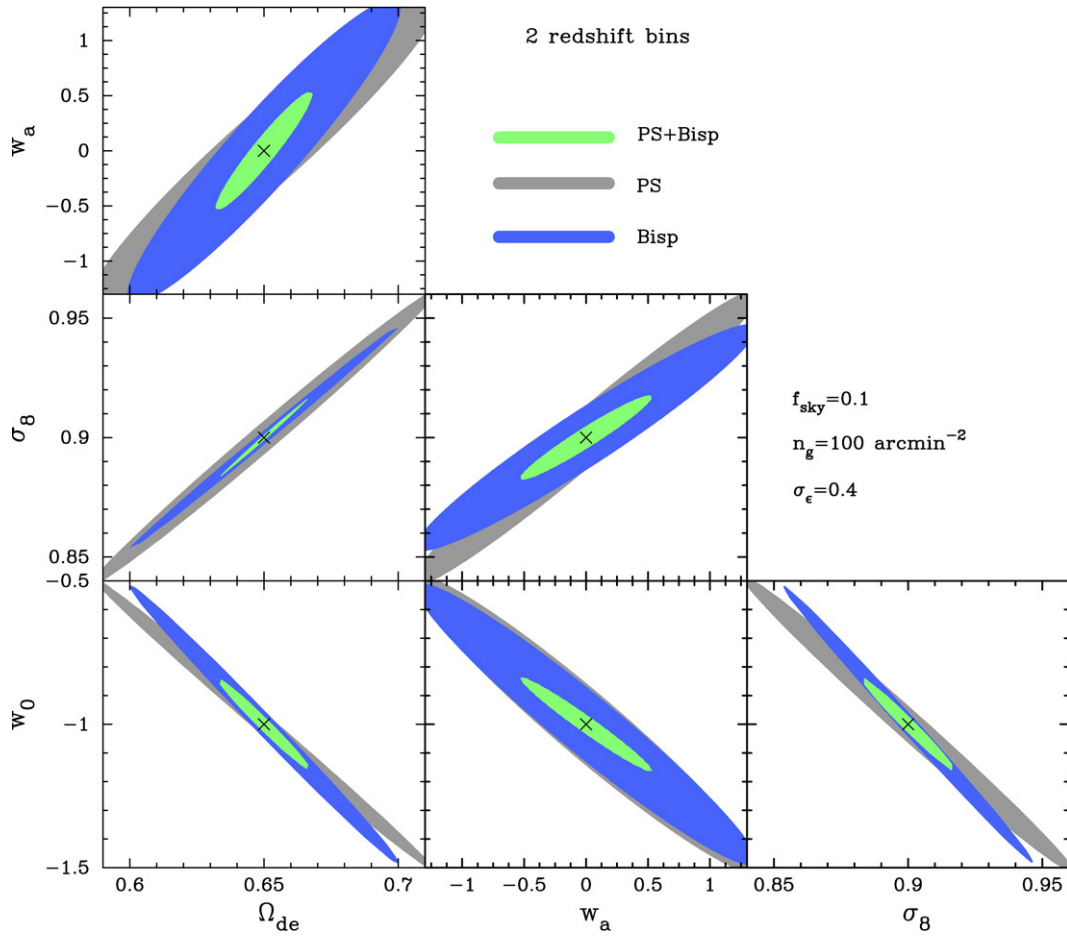
Fig. 10. Projected 68% confidence level constraints in the parameter space of Ω_{de}, w_0, w_a and σ_8 from the lensing power spectrum and the bispectrum in two redshift bins, as indicated. The coefficients w_0 and w_a parameterize the equation of state of the dark energy component. The results shown are obtained assuming priors on n, $\Omega_b h^2$ and h expected from the Planck mission. The sky coverage and number density are taken to be $f_{sky} = 0.1$ and $n_g = 100$ arc min^{-2}, and angular modes $50 \leq l \leq 3000$ are used. From [278].
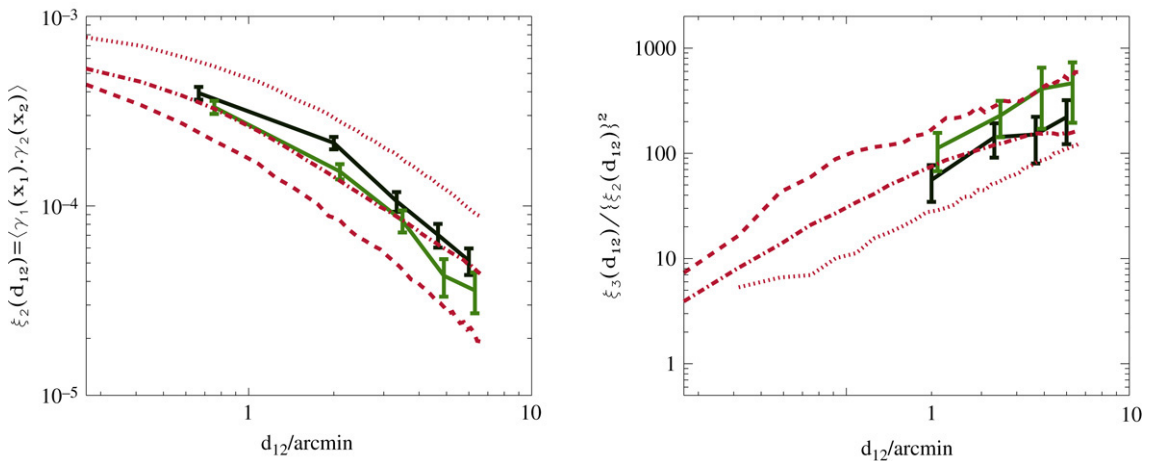

Fig. 11. Results for the VIRMOS-DESCART survey for the two point correlation function (left) and the reduced three point function (right). The solid line with error bars shows the raw results, when both the E and B contributions to the two-point correlation functions are included. The dot–dashed line with error bars corresponds to measurements where the contribution of the B mode has been subtracted out from the two-point correlation function (but not from ξ_3 there is no known way to do it). These measurements are compared to results obtained in τCDM, OCDM and ΛCDM simulations (dashed, dotted and dot–dashed lines respectively). From [25].

A more systematic approach presented in [248] is to look for natural components which transform in a simple way through rotations. Thus, to handle the three point function $\langle\gamma(\vec{\theta}_1)\gamma(\vec{\theta}_2)\gamma(\vec{\theta}_3)\rangle$ one first defines the "center" **c** of the three directions $\vec{\theta}_1, \vec{\theta}_2, \vec{\theta}_3$ on the sky (**c** may be taken for instance as the centroid, the circumcenter or the orthocenter of the triangle). Next, at each point one defines γ_+ as the component of the shear along the direction that separates **c** and $\vec{\theta}_i$ and $\gamma_\times$ as the component along this direction rotated by $45°$. From these tangential and cross components one introduces the complex shear $\gamma^{(\mathbf{c})} = \gamma_+ + i\gamma_\times$ and the "natural components" are defined as the four complex combinations:

$$\Gamma^{(0)} = \langle\gamma^{(\mathbf{c})}(\vec{\theta}_1)\gamma^{(\mathbf{c})}(\vec{\theta}_2)\gamma^{(\mathbf{c})}(\vec{\theta}_3)\rangle, \qquad \Gamma^{(1)} = \langle\gamma^{(\mathbf{c})*}\gamma^{(\mathbf{c})}\gamma^{(\mathbf{c})}\rangle,$$
$$\Gamma^{(2)} = \langle\gamma^{(\mathbf{c})}\gamma^{(\mathbf{c})*}\gamma^{(\mathbf{c})}\rangle, \qquad \Gamma^{(3)} = \langle\gamma^{(\mathbf{c})}\gamma^{(\mathbf{c})}\gamma^{(\mathbf{c})*}\rangle. \tag{5.7}$$

Clearly the $\Gamma^{(i)}$ only depend on the geometry of the triangle but to avoid ambiguities and miscalculations one must ensure that the points are always labeled in the same direction (e.g. counterclockwise, [249]). Each of these $\Gamma^{(i)}$ is invariant only under special rotations but the important feature is that, under a general rotation, the different $\Gamma^{(i)}$ do not mix but are simply multiplied by a phase factor. Note however that the four $\Gamma^{(i)}$ are not independent as they arise from the same matter distribution and three-point statistics are fully described by the projected matter bispectrum [250]. On the other hand, such interrelations provide a redundancy which might be used to detect noise sources or B modes.

An alternative method to study the shear three-point function is to divide the possible combinations into even and odd quantities through parity transformations [316]. For instance, one chooses for the center of the triangle the barycenter $\mathbf{c} = (\vec{\theta}_1 + \vec{\theta}_2 + \vec{\theta}_3)/3$ and defines again the tangential and cross components of the shear, γ_+ and $\gamma_\times$, from the direction that separates **c** and $\vec{\theta}_i$ and from this direction rotated by $45°$. Clearly this rotation changes direction under a parity transformation so that $\gamma_\times \to -\gamma_\times$ (since γ is a spin-2 field, see Eq. (2.17), and the relative rotation is $2 \times 45° = 90°$) whereas $\gamma_+ \to \gamma_+$. Therefore, we obtain four parity-even three-point correlations: $\langle\gamma_+\gamma_+\gamma_+\rangle$, $\langle\gamma_+\gamma_\times\gamma_\times\rangle$, $\langle\gamma_\times\gamma_+\gamma_\times\rangle$, $\langle\gamma_\times\gamma_\times\gamma_+\rangle$, and four parity-odd three-point correlations: $\langle\gamma_\times\gamma_\times\gamma_\times\rangle$, $\langle\gamma_\times\gamma_+\gamma_+\rangle$, $\langle\gamma_+\gamma_\times\gamma_+\rangle$, $\langle\gamma_+\gamma_+\gamma_\times\rangle$. As a consequence, for some symmetric configurations some odd functions must vanish [277]. In particular, for equilateral triangles all odd functions vanish. This property assumes that the shear results only from weak-lensing (which only produces E modes), whereas source galaxy clustering, intrinsic alignments and observational noise can produce both E and B modes (see Sections 3 and 4). The advantage of this procedure is that by focusing on even functions one avoids diluting the signal by combining the estimators with parts which contain no weak-lensing information (odd functions for symmetrical triangle geometries). Besides, the parity-odd functions can be used to monitor the noise or to estimate the contribution associated with higher-order effects beyond the Born approximation, source clustering or intrinsic alignments. Ref. [316] used a halo model (see Appendix A.3) to investigate the behavior of these three-point correlations as a function of the triangle geometry. Ref. [279] found that the halo model agrees well with numerical simulations at scales $> 1'$ and could be used to obtain predictions for shear statistics in order to lift degeneracies in cosmological parameters. We display their results in Fig. 12 which also shows that odd functions are smaller than even ones and vanish for symmetric geometries. They also note that future weak-lensing observations may be able to constrain the parameters of the halo model such as the mean halo density profile and halo mass function. On the other hand, using ray-tracing simulations Ref. [277] also evaluated the signal-to-noise taking into account the noise associated with galaxy intrinsic ellipticities. They found that a deep lensing survey of area 10 deg^2 should be sufficient to detect a non-zero signal but an accurate measure would require an area exceeding 100 deg^2.

5.2. Cumulants and probability distributions

A simpler quantity than the three-point functions discussed above is provided by the third-order cumulant $\langle\bar{X}^3\rangle$ of smoothed weak-lensing observables (2.11) such as the smoothed convergence $\bar{\kappa}$ or the aperture-mass M_{ap}. In the quasi-linear regime where a perturbative approach is valid (with Gaussian initial conditions) one can see from Eqs. (5.3)–(5.6) that the skewness $S_3^{(\kappa)} = \langle\bar{\kappa}^3\rangle/\langle\bar{\kappa}^2\rangle^2$ of the smoothed convergence is independent of the matter density power spectrum normalization σ_8 (the same property is clearly valid for other observables like M_{ap} which are linear over the matter density field). Therefore, by measuring the second- and third-order moments of the convergence or of the aperture mass at large angular scales one can obtain a constraint on Ω_m [21]. Indeed, from Eq. (2.9) we see that $\kappa \sim \Omega_m$ (neglecting the dependence of cosmological distances $\mathcal{D}$ on Ω_m) hence we can expect a strong dependence on Ω_m of the skewness as $S_3^{(\kappa)} \sim \Omega_m^{-1}$. A numerical study shows indeed that for sources at redshift $z_s \simeq 1$ the skewness scales roughly as $S_3^{(\kappa)} \sim \Omega_m^{-0.8}$ [21]. Alternatively, from the skewness of weak lensing observables one can derive the skewness of the matter density field in the linear regime and check that the scenario of the growth of large-scale structures through gravitational instability from initial Gaussian conditions is valid. In order to increase the information content which can be extracted from low-order cumulants one can consider generalized moments such as $\langle M_{ap}(\theta_{s1})M_{ap}(\theta_{s2})M_{ap}(\theta_{s3})\rangle$ which cross-correlate the aperture-mass $M_{ap}(\theta_{si})$ associated with three different filter radii θ_{s1}, θ_{s2} and θ_{s3}. Then, the amplitude of such cumulants can be used to constrain cosmological parameters whereas the dependence on the angular radius or the angular separation of the various filters helps constraining the properties of the large-scale density field [209,160]. For instance, one can introduce correlation coefficients r_{pqs} such as:

$$r_{pqs} = \frac{\langle\bar{X}_1^p\bar{X}_2^q\bar{X}_3^s\rangle_c}{\langle\bar{X}_1^{p+q+s}\rangle_c^{p/(p+q+s)}\langle\bar{X}_2^{p+q+s}\rangle_c^{q/(p+q+s)}\langle\bar{X}_3^{p+q+s}\rangle_c^{s/(p+q+s)}}, \tag{5.8}$$
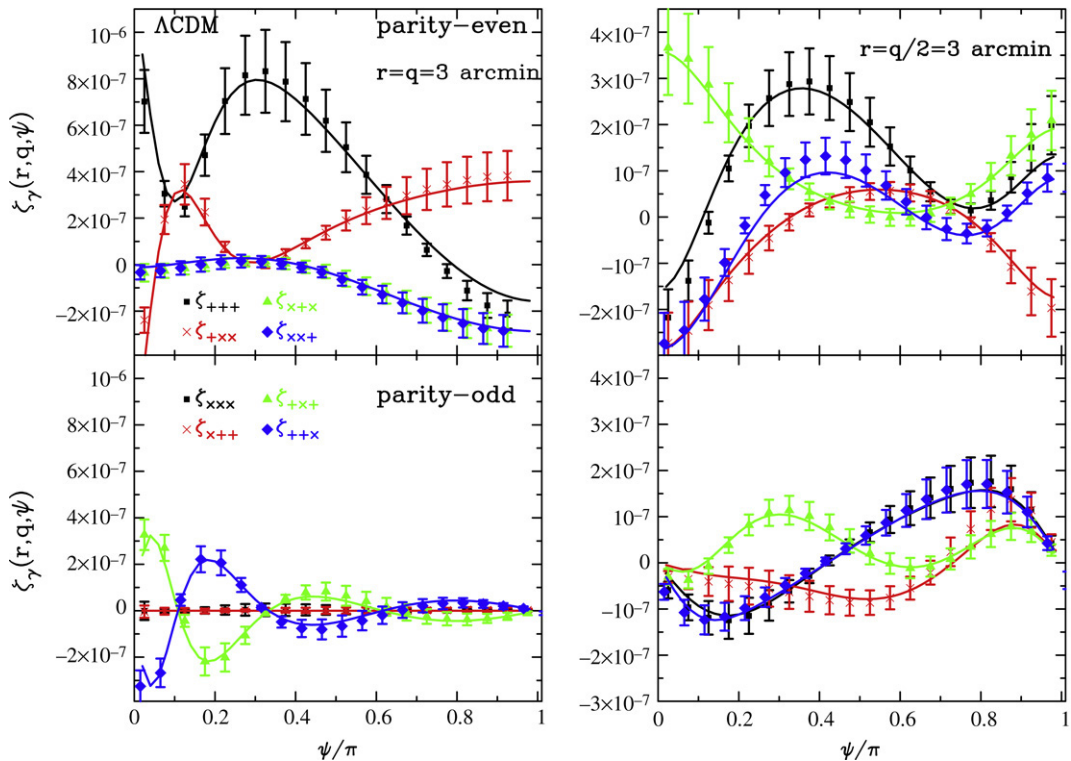
Fig. 12. The eight shear 3-point correlation functions for the ΛCDM model against triangle configurations (ψ is the angle between the two sides of length q and r). The upper and lower plots show the results for the parity-even and -odd functions, respectively. Note that range on the y-axis for the right panel is about two times smaller than in the left panel. The solid curves show the halo model predictions for the eight shear 3-point correlation functions, while the symbols are the simulation results as indicated. From [278].

where $\bar{X}_i$ is the aperture-mass or the convergence smoothed over scale θ_{si} (the source redshift distributions $n_i(z_s)$ may also be different). These correlation coefficients describe the information associated with three-point cumulants $\langle \bar{X}_1^p \bar{X}_2^q \bar{X}_3^s \rangle_c$ which goes beyond the one-point cumulants $\langle \bar{X}^p \rangle_c$. We show in Fig. 13 the predictions of an analytical model based on a hierarchical *ansatz* (Appendix A.2) for the aperture-mass statistics, applied to the planned SNAP survey (left panel) and compared with numerical simulations (right panel). The behavior of these correlation coefficients can be used to discriminate between models of the density field [209] and to check that the observed non-Gaussianities arise from non-linear gravitational clustering. On the other hand, the left panel in Fig. 13 also shows how the aperture-mass is correlated between different angular scales. This correlation decreases faster than for the smoothed convergence or the smoothed shear because the filter $W_{M_{ap}}(\ell\theta_s)$ is more narrow than W_κ in Fourier space, see Fig. 2. This is actually useful if one intends to derive constraints on cosmology from weak lensing surveys since it means that the errors associated with sufficiently different scales are uncorrelated. This also holds for the two-point moments discussed in Section 3 and for higher-order moments. Of course, the power-spectrum $P_\kappa(\ell)$ and higher-order generalization such as the bispectrum $B_\kappa(\ell_1, \ell_2, \ell_3)$ are even less correlated and contain all the relevant information.

In practice, because of the numerous holes within the survey area one first computes shear three-point correlations by summing over galaxy triplets and next writes $\langle M_{ap}^3 \rangle$ as an integral over these three-point correlations (using the fact that M_{ap} can be written in terms of the shear γ), see for instance [146]. Applying this method to the VIRMOS-DESCART data Ref. [218] were able to detect $S_3^{(M_{ap})}$ and to infer an upper bound $\Omega_m < 0.5$ by comparison with simulations. Next, one could measure higher order moments of weak lensing observables. Note that for the shear components odd order moments vanish by symmetry so that one needs to consider the fourth-order moment to go beyond the variance [277]. However, higher order moments are increasingly noisy [295] so that it has not been possible to go beyond the skewness yet.

In order to compare observations with theory one needs to use numerical simulations or to build analytical models which can describe the low order moments of weak lensing observables or their full probability distribution, as described in the Appendix. This can be done through a hierarchical *ansatz* where all higher-order density correlations are expressed in terms of the two-point correlation [12,295]. Then, the probability distribution of weak lensing observables can be directly written in terms of the probability distribution of the matter density (Appendix A.2). In some cases the mere existence of this relationship allows one to discriminate between analytical models for the density field which are very similar [207]. Alternatively, one can use a halo model (Appendix A.3) where the matter distribution is described as a collection of halos [52] and the low order moments of weak lensing observables can be derived by averaging over the statistics of these halos [278,
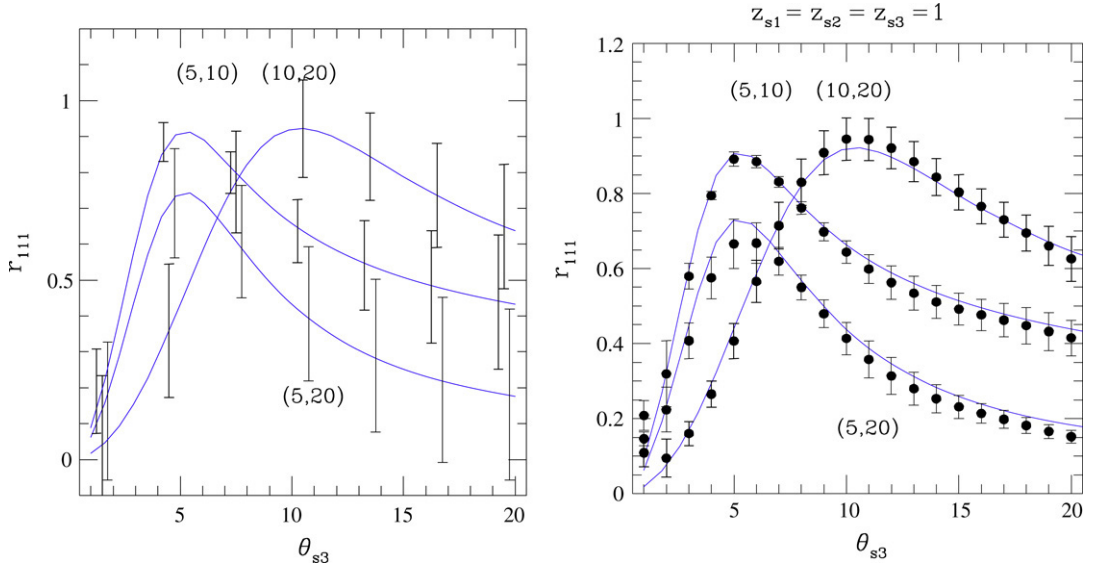
Fig. 13. *Left panel:* The correlator r_{111} of the aperture-mass for the full wide SNAP survey is plotted as a function of smoothing angle θ_{s3} for a fixed pair of $(\theta_{s1}, \theta_{s2})$. The pair $(\theta_{s1}, \theta_{s2})$ for each curve is indicated in the plot. Error bars denote the $1 - \sigma$ scatter around the mean, associated with galaxy intrinsic ellipticities and cosmic variance. *Right panel:* The three-point correlation coefficient r_{111} of the aperture-mass as a function of smoothing angle θ_{s3} for a fixed pair of $(\theta_{s1}, \theta_{s2})$. The three source redshifts are equal: $z_{s1} = z_{s2} = z_{s3} = 1$. The solid curve is the analytical model (A.19) while solid points with error-bars are measurements from simulation data. From [209].
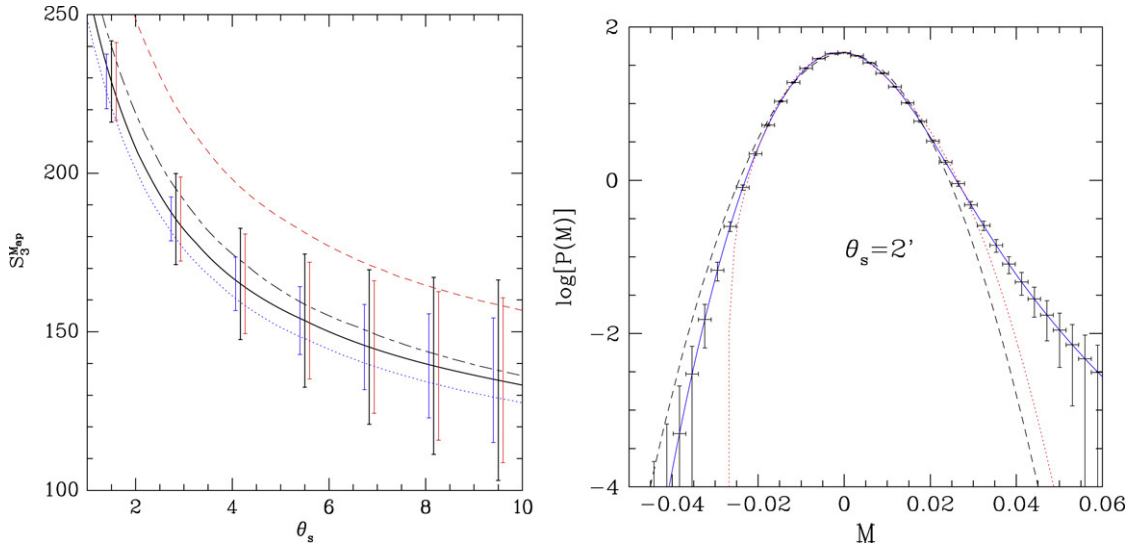

Fig. 14. *Left panel:* The skewness $s_3^{Map} = \langle M_{ap}^3 \rangle / \langle M_{ap}^2 \rangle^2$ of the aperture-mass (solid curve), for the SNAP survey. The central error bars show the $1 - \sigma$ dispersion due to galaxy intrinsic ellipticities and cosmic variance. The smaller error bars which are slightly shifted to the left show the dispersion obtained by neglecting non-Gaussian contributions to the dispersion whereas the smaller error bars which are slightly shifted to the right show the dispersion obtained from the estimator built from the cumulant rather than the moment. We also show the effect of a 10% increase of Ω_m (lower dotted curve), of a 10% increase of σ_8 (central dot–dashed curve) and of a 10% decrease of the redshift z_0 (upper dashed curve). *Right panel:* The pdf $\mathcal{P}(M)$ for the estimator M associated with the aperture-mass M_{ap}. Note that the Gaussian noise introduced by intrinsic ellipticities makes $\mathcal{P}(M)$ closer to the Gaussian than the actual pdf $\mathcal{P}(M_{ap})$ which only takes into account gravitational lensing. The solid line shows the theoretical prediction, the dashed line is the Gaussian and the dotted line is the Edgeworth expansion up to the first non-Gaussian term (the skewness). The error bars show the $1 - \sigma$ dispersion. From [295].

279]. On the other hand, one can use weak lensing to constrain halo properties and to detect substructures [67]. For the particular case of the smoothed convergence the probability distribution function (PDF) $\mathcal{P}(\bar{\kappa})$ can be expressed in terms of the PDF $\mathcal{P}(\delta)$ of the 3D matter density contrast within some simple approximations, see Eq. (A.7). This allows one to apply to the convergence simple models which were originally devised for the 3D density field such as the lognormal model [282] or more elaborate ones [291,309,12]. For more complex weak-lensing observables such as the aperture-mass these approximations can no longer be used and one needs an explicit model of the density correlations (see Appendix) to derive their cumulants or their PDF. We display in Fig. 14 the results obtained from a hierarchical *ansatz* for the aperture-
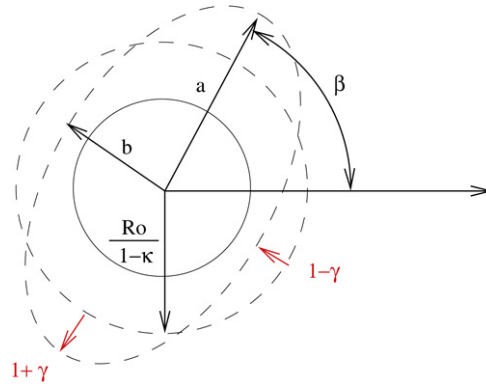
Fig. 15. Schematic representation of a lensed galaxy. In the source plane, the galaxy is circular and has radius R_0. Convergence κ stretches its average radius to $R_0/(1 - \kappa)$, and the shear γ distort the galaxy along some angle β. a and b are the semi-major and semi-minor axis respectively.

mass, for the skewness (left panel) and the PDF of an estimator of M_{ap} [295]. In such calculations one must take into account the noise associated with the intrinsic ellipticities of galaxies and the cosmic variance. However, the left panel of Fig. 14 shows that despite these sources of noise future surveys such as SNAP should be able to constrain cosmological parameters at a level of 10% from such low-order moments, whereas the right panel shows that the tails of the PDF $\mathscr{P}(M_{ap})$ should allow one to extract information beyond low-order moments.

5.3. Primordial non-Gaussianities

So far we have discussed the non-Gaussianities associated with the non-linearity of the gravitational dynamics, assuming Gaussian initial conditions. However, results from future surveys can also be very useful in constraining primordial non-Gaussianity predicted by some early universe theories [280]. On the other hand, generalised theories of gravity can have very different predictions regarding gravity-induced non-Gaussianities as compared to General Relativity, which can also be probed using future data. A joint analysis of power spectrum and bispectrum from weak lensing surveys will provide a very powerful way to constrain, not only cosmological parameters, but early universe theories and alternative theories of gravitation, see also [234]. Thus, a recent work [27] has studied the possibility of constraining higher-dimensional gravity from the cosmic shear three-point correlation function.

6. Data reduction from weak lensing surveys

6.1. Shape measurement

Weak lensing by large scale structures induces a coherent alignment of galaxy shapes across large angular distances. A crucial step for its measurement is the accurate estimation of galaxy shapes, free of biases and systematics. A common approximation is to describe galaxies as simple elliptical objects, for which the quadrupole of the light distribution is a fair estimate of the shear γ. If we call $f(\vec{\theta})$ the 2-dimensional light distribution of the galaxy image, then the quadrupole moment Q_{ij} is defined in its simplest form as:

$$Q_{ij} = \frac{\int d\theta_i d\theta_j w(|\vec{\theta}|) f(\vec{\theta})(\theta_i - \hat{\theta}_i)(\theta_j - \hat{\theta}_j)}{\int d\theta_i d\theta_j \, w(|\vec{\theta}|) f(\vec{\theta})}, \tag{6.1}$$

where $\hat{\theta}_i$ is the centroid of the light distribution. The role of the isotropic weight function $w(|\vec{\theta}|)$ is to suppress the pixel noise at large distance from the center of the light distribution. This weighting is crucial to all shape measurement, if absent, the galaxy ellipticity would be extremely noisy. Most of the problems in shear measurement is precisely to recover the true galaxy shape before convolution, and the weight function makes this task very complicated. Different shape measurement techniques have chosen different functional forms for w, and this is discussed in the following section. The ellipticity $e_i = (e_1, e_2)$ of the galaxy is given by (using the same definition as in Section 3.4 with Eqs. (3.15)–(3.17)):

$$(e_1, e_2) = \left(\frac{Q_{11} - Q_{22}}{Q_{11} + Q_{22}}; \frac{2Q_{12}}{Q_{11} + Q_{22}} \right). \tag{6.2}$$

When galaxies are not lensed (in the source plane), their average ellipticity is zero $\langle e_i \rangle = 0$ from the assumption of isotropy. Lensed galaxies exhibit an average non-zero distortion $\delta_i = \langle e_i \rangle$ over the coherence scale of the lensing potential ϕ because the shear γ_i stretches galaxy shapes locally in the same direction. The distortion is given by Eq. (6.2), where Q

is the quadrupole moment of the galaxy image Q^I. The relation between the source quadrupole Q^S and Q^I depends on the magnification matrix $\mathcal{A}$ (see Section 2):

$$Q^I = \mathcal{A}^{-1} Q^S \mathcal{A}^{-1}, \tag{6.3}$$

where

$$\mathcal{A} = \begin{pmatrix} 1 - \kappa - \gamma_1 & -\gamma_2 \\ -\gamma_2 & 1 - \kappa + \gamma_1 \end{pmatrix}. \tag{6.4}$$

The matrix $\mathcal{A}$ of Eq. (6.4) describes the mapping between the source and image planes. The source galaxy surface brightness $f^S(\vec{\theta})$ is stretched along the eigen axis of $\mathcal{A}$, and the observed galaxy light distribution becomes:

$$f(\vec{\theta}) = \left[1 + (\mathcal{A} - I)_{ij} \theta_j \partial_i \right] f^S(\vec{\theta}). \tag{6.5}$$

Fig. 15 shows what is happening to the shape of a galaxy in the weak lensing regime. The quantities of interest can be listed as follows (see also Section 2):

- Convergence κ
- Distortion $|\delta| = \frac{a^2 - b^2}{a^2 + b^2}$
- Shear $|\gamma| = \frac{a - b}{a + b}$
- Magnification $\mu = [\det(\mathcal{A})]^{-1} = \left[(1 - \kappa)^2 - \gamma^2 \right]^{-1}$.

The convergence and magnification cannot be easily measured because we do not know the size of galaxies in the source plane. Therefore, we focus on the shear (and the related aperture-mass M_{ap}, see Eq. (2.12)) as estimators of weak lensing effects. However we would like to point out that magnification has been measured successfully on SLOAN from the excess of distant quasars around foreground galaxies [254] and this technique could potentially be a powerful probe of cosmology in the future. The distortion offers the advantage that we know statistically its value in the source plane, i.e. $\langle \delta_i \rangle = 0$, meaning that source galaxies are randomly aligned (but see Sections 4.7 and 4.8).

6.2. Point spread function correction

One cannot easily measure the distortion δ_i for two reasons: the optics of the telescope induce geometrical distortions that can be misinterpreted as a weak lensing signal if not carefully corrected: the stars, which provide a picture of the Point Spread Function (PSF) of the telescope's aperture, have complicated, elongated shapes. The second problem is that the weak lensing signal is better measured on distant galaxies. Indeed, since the line of sight is more extended weak lensing effects have a greater magnitude, see Eq. (2.4). However, these distant galaxies are small and faint, and the sky noise for these objects is large. Consequently, a naive estimation of the quadrupole Q_{ij} from Eq. (6.1) is essentially a measure of sky noise.

Refs. [152,178] showed that one can overcome both problems by (1) reducing the noise at the edge of the galaxy using a gaussian filter, (2) expressing the effect of the PSF convolution analytically as a perturbation expansion, and use the first-order term to correct the galaxy shapes. The KSB method [152] can be summarized as follows: the observed ellipticity e_i^{obs} is the sum of three terms, the first is the intrinsic ellipticity e_i^{int} of the galaxy before lensing and before convolution with the PSF. e_i^{int} is unobservable, but the isotropy of space implies $\langle e_i^{\mathrm{int}} \rangle = 0$. The second term describes the galaxy shape response to an anisotropic PSF (which depends on a measurable quantity called the smear polarizability tensor P_{ij}^{sm}), and the last term describes the response to the isotropic PSF (which depends on the "preseeing" shear polarizability P^γ, also measurable). Therefore the observed ellipticity becomes

$$e_i^{\mathrm{obs}} = e_i^{\mathrm{int}} + P_{ij}^{\mathrm{sm}} p_j^* + P^\gamma \gamma_i, \tag{6.6}$$

where γ_i is the shear we want to measure and p^* is the stellar ellipticity estimated at the galaxy position. P^{sm}, p^* and P^γ can all be estimated from the image (see [152] for the details). Some refinements should be included when shapes are measured on space data [112,223], but they do not change the philosophy of the method, which remains a first-order perturbative approach. The estimation of p^* at the galaxy position is done by first measuring p^* on the stars and then interpolating its value assuming a second-order polynomial variation across the CCDs. This is a crucial step since an inaccurate model could lead to significant B modes in the signal [302], fortunately various models have been proposed to account for non-polynomial variations [117]. Ref. [141] has shown that we can perform a singular value decomposition method of the PSF variation between individual exposures in order to improve the correction. This would be a particularly useful approach for lensing surveys planning to observe the same part of the sky hundreds of times (LSST, ALPACA).

The ultimate accuracy of galaxy shape correction is still a wide open question. Whether or not there is a fundamental limit in the measurement of galaxy shapes is a particularly critical issue for the design of future gravitational lensing surveys (see Section 6.3). KSB has been historically the first shape measurement method working and for that reason it has been tested intensively, but its accuracy is not expected to be better than 5%–10% [73]. Clearly this is not enough for precision cosmology which seeks sub-percent precision on shape measurement.

Many post-KSB techniques have been developed over the past five years in order to improve upon the original KSB approach, most of them are being intensively tested only now [105,193]. A quick summary of these methods follows. The reader can obtain the details by looking at the original papers or the description given in [105]. Ref. [166] proposed to model the PSF and the galaxies by a sum of Gaussians of different widths. The pre-seeing galaxy shape is recovered by a χ^2 minimisation between the galaxy model and the measured profile. Ref. [155] extended the original KSB by properly modelling the PSF with a realistic kernel, dropping the assumption of a Gaussian profile. The PSF is then circularized prior to measuring the galaxy shapes (the circularization technique is also used by [270]). A radically different approach consists in projecting the shapes (galaxies and stars) on a basis of orthogonal functions [28,225,226]. The effect of convolution and shear can be expressed analytically on the basis functions and the solution of the preseeing galaxy shape can be found by a straightforward matrix inversion. This technique turns out to be important not only for shape measurement, but also for simulating realistic galaxy profiles. It also offers in principle a total control of the different processes changing the shape of a galaxy (shear, amplification, PSF, etc...). Mathematically, a galaxy with profile $f(\vec{\theta})$ can be decomposed over a set of basis functions $B_{(n_1,n_2)}(\vec{\theta}; \beta)$ as

$$f(\vec{\theta}) = \sum_{(n_1,n_2)} f_{(n_1,n_2)} B_{(n_1,n_2)}(\vec{\theta}; \beta), \tag{6.7}$$

where β is a scaling parameter adjusted to the size of the galaxy we want to analyse, $f_{(n_1,n_2)} = f_{\mathbf{n}}$ are called the shapelets coefficients, and $B_{(n_1,n_2)}$ could be any family of polynomial functions fulfilling our favorite recurrence relation (orthogonality, orthonormality, etc...). Although the description is given here for a cartesian coordinate system, the same formalism can be developed for any coordinate system better suited for galaxy shape analysis (see [191] for a derivation using polar coordinates). The convolution of a lensed galaxy $f(\vec{\theta})$ with a stellar profile $g(\vec{\theta})$ produces a galaxy with profile $h(\vec{\theta})$ such that its shapelets coefficients are:

$$h_{\mathbf{n}} = \sum_{\mathbf{m,l}} C_{\mathbf{nml}} f_{\mathbf{m}} g_{\mathbf{l}} = \sum_{\mathbf{m}} P_{\mathbf{nm}} f_{\mathbf{m}}, \tag{6.8}$$

where C and $P = Cg$ are matrices that can be measured on the data. The preseeing galaxy profile can be formally obtained from the matrix inversion $f = P^{-1}h$. Ref. [28] developed a similar method but they also perform a circularization of the PSF like in [270] prior to the measurement of the pre-seeing galaxy shape. Ref. [167] has implemented a version of the shapelet technique based on ideas developed in [166] where galaxies and PSF are decomposed on a fixed set of simple profiles. Currently, there are six different shape measurement techniques, and several implementations of KSB, corresponding to more than a dozen of different pipelines. This clearly demonstrates the richness of the topic, but one should ensure that they all lead to the same shear measurement. A comparison of the performances of all these techniques is shown in [109], but the authors focussed on analytical galaxy profiles instead of real, noisy, profiles. They found that KSB was performing the best, which is surprising given the number of approximations involved. The Shear TEsting Program STEP [105,193][1] has been setup in order to systematically perform intensive tests of shape measurement methods. Its goal is to test the different pipelines on simulated and real data sets and to find the ultimate limit of shape measurement from space and ground based images.

Ref. [105] measured the difference between the measured shear γ_i^{meas} and the true shear γ_i^{true} on a large number of simulated images with very different PSF simulating various optical defects of the telescope. The chosen parametrization was:

$$\gamma_1^{\mathrm{meas}} - \gamma_1^{\mathrm{true}} = q(\gamma_1^{\mathrm{true}})^2 + m\gamma_1^{\mathrm{true}} + c_1, \tag{6.9}$$

where q, m and c_1 are measured from different realizations of image quality (PSF anisotropy and seeing size). Fig. 16 shows the r.m.s. of these parameters. It shows the main result from STEP, indicating that shape measurement accuracy is within the few percent range, at least one order of magnitude above the required accuracy for future experiments such as SNAP and LSST. This figure also shows that KSB is performing remarkably well, in agreement with [109], and the newer methods are potentially even more powerful, although this is not revealed by the STEP analysis. The average calibration factor m with today's shape measurement methods is found to be of the order of one percent or higher of the input shear, and the systematic bias c is of the order of a tenth of a percent for most techniques. Recent developments are encouraging, however, with fast model-fitting techniques such as *lensfit* [201] showing smaller offsets than the best linear STEP methods [164].

Among all the methods, the very attractive feature of the shapelets lies in the fact that each transformation experienced by a galaxy (PSF, shear, convergence, etc...) can be expressed as a simple set of operators acting linearly on the set of basis functions describing the galaxy. A general transformation of the galaxy shape is therefore a linear process which can formally be solved in one pass to provide the pre-seeing shape. The shapelets, or similar approaches [28], provide in principle a perfect description of the galaxy shapes. Is it the ultimate method with the best possible accuracy? In the weak lensing regime for instance, the quadrupole of the light distribution fully describes the shear γ, a two-components spin-weight 2 object, and it is unnecessary to measure the details of the galaxy shape. In that case, the shapelets might appear like overkill, and limiting
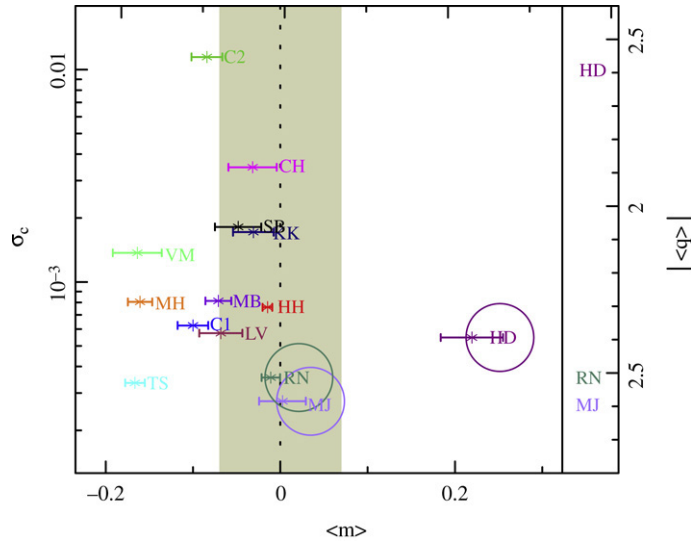
---

[1] http://www.physics.ubc.ca/~heymans.

Fig. 16. From Heymans et al. [105], plot showing the calibration bias *m*, PSF residual and non-linearity ⟨*q*⟩ for different pipelines (see Heymans et al. [105] for a complete list of references and detailed description of the methods).

the number of basis functions is appropriate [167]. The solution of the shape measurement problem is a trade-off between an accurate description of the galaxy morphology (i.e. galaxy structures) and an unbiased measure of the second order moments: we want to describe the galaxy shape with enough, but not too many, details. This optimal trade-off depends on the weak lensing information we want to extract from the galaxy distortion. For instance, in the weak lensing regime, it is assumed that the shear does not vary across the galaxy, and the quadrupole of the light distribution is then a complete description of the lensing effect. This is equivalent to saying that the centroid of a lensed galaxy is the lensed centroid of the source galaxy. Mathematically, this means that

$$\left(\vec{\theta}^{S} - \vec{\theta}^{SC}\right) \simeq \mathcal{A}\left(\vec{\theta}^{I} - \vec{\theta}^{IC}\right),\tag{6.10}$$

where $\vec{\theta}^{S}$ and $\vec{\theta}^{I}$ are the angular position of a galaxy source and image respectively, and $\vec{\theta}^{SC}$ and $\vec{\theta}^{IC}$ are the centroid position of the source and image respectively. Eq. (6.3) is a direct consequence of this approximation. It obviously breaks down near the critical line where the determinant of the amplification matrix $\mathcal{A}$ is zero and the magnification is infinite. The source galaxy is then strongly distorted and gravitational arcs are observed [76]. In the intermediate regime where source galaxies are mildly distorted and have an arc-like shape, weak lensing is just an approximation, and the quadrupole of the light distribution is not enough to quantify the lensing effect. A higher-order description of the galaxy shape becomes necessary [88]. Refs. [89, 8,194] developed the theory of *flexion* which is a description of the next order of shear measurements, the octopole. In that case, Eq. (6.10) is not valid and should be replaced by:

$$\theta'_{i} = \mathcal{A}_{ij}\theta_{j} + \frac{1}{2}D_{ijk}\theta_{i}\theta_{j},\tag{6.11}$$

where $D_{ijk} = \partial_{k}\mathcal{A}_{ij}$ is given by:

$$D_{ij1} = \begin{pmatrix} -2\gamma_{1,1} - \gamma_{2,2} & -\gamma_{2,1} \\ -\gamma_{2,1} & -\gamma_{2,2} \end{pmatrix}; \qquad D_{ij2} = \begin{pmatrix} -\gamma_{2,1} & -\gamma_{2,1} \\ -\gamma_{2,1} & 2\gamma_{1,2} - \gamma_{2,1} \end{pmatrix}.\tag{6.12}$$

Higher orders of galaxy shapes are a probe of higher order derivatives of the gravitational lensing potential [244]. This is therefore particularly relevant for lensing by cluster of galaxies and space quality images, because the latter is well suited for an accurate measurement of galaxy shapes beyond the quadrupole. The new relation between the source and image galaxy profile is given by

$$f(\vec{\theta}) = \left[1 + \left[(\mathcal{A} - I)_{ij}\theta_{j} + \frac{1}{2}D_{ijk}\theta_{j}\theta_{k}\right]\partial_{i}\right]f^{S}(\vec{\theta}),\tag{6.13}$$

which replaces Eq. (6.5). The flexion terms can be conveniently expressed in terms of shapelet operators [89]. The practical utility of flexion has not been demonstrated yet, but progress is being made to show whether or not it is measurable. With the development of CCD detectors in space it is likely that flexion could provide useful lensing information [8].

Lots of progress has been made in the measurement of galaxy shapes since the original KSB paper in 1995. The most recent shape measurement method [167] shows that the one percent accuracy goal has not yet been reached, and most of the effort now consists of showing that this goal can be met in order to perform high precision cosmology with weak lensing;
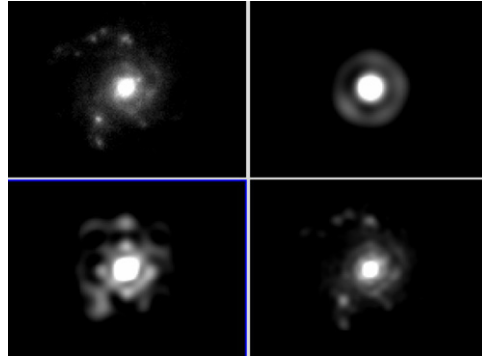
Fig. 17. Simulating galaxies with shapelets: Top-left is a galaxy from the Hubble Ultra Deep Field and the other panels show its simulated image using the shapelets with $n_{max} = 5, 10, 30$.
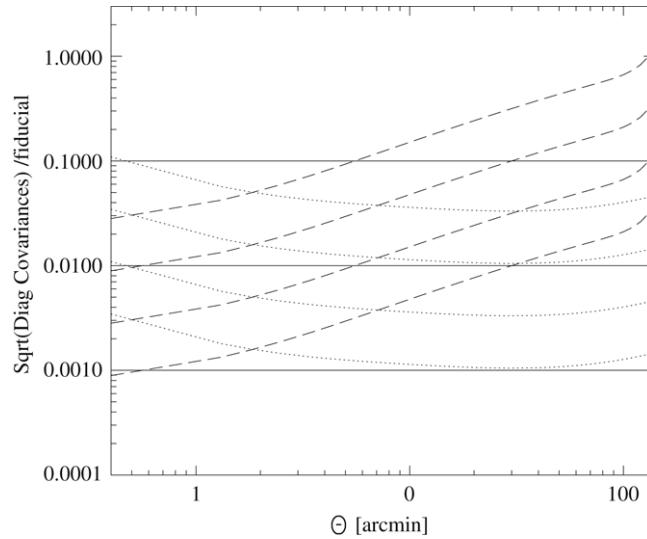

Fig. 18. Two sources of error: statistical noise and cosmic variance. The curves show the diagonal part of the covariance matrix for either source of noise, normalised by the fiducial model shear variance. Dashed line: contribution from the statistical error, dotted line: contribution from the sampling (cosmic) variance. The thick solid lines show various levels of multiplicative errors from 0.01 to 0.001.

this is the primary goal of the STEP project. With the development of these techniques and improving image quality, it becomes possible to measure higher order shear effects such as the octopole. Shapelets or a similar method are particularly useful to extract high-order morphology information, while KSB is enough for percent precision shear measurement [105,193].

The shapelets can also be used to generate realistic images of galaxies, which is important for testing shape measurement methods. Here one uses a training set to *teach* a galaxy image simulator how to generate a realistic combination of shapelet coefficients in order to reproduce statistically real data sets. One such galaxy simulation is shown in Fig. 17. Ref. [194] for instance simulated galaxies using the shapelets, whose distribution has been trained using the Hubble Ultra Deep Field.

6.3. Statistical and systematic errors

In this section, we consider the potential sources of error and systematics in the shear measurement, not the error caused by intrinsic alignment (see Section 4.7) and selection biases correlated with the shear orientation and amplitude [109]. The latter was shown to be negligible [105].

A complete description of galaxy shape is certainly not necessary for most weak lensing applications. According to [105], the main limitation in shear measurement comes from the calibration of the shear amplitude: the PSF anisotropy is relatively easy to correct, but the isotropic correction due to the seeing is still not accurate to better than a few percent (see Fig. 16). An additive error should also be considered, as suggested by Fig. 16. Ref. [133] has shown that, in order not to degrade significantly the cosmological parameters estimation from future weak lensing experiments (SNAP and LSST), the additive error has to be less then 10^{-4}, which is one order of magnitude better than what can be achieved today (see Fig. 16). It is still unclear how to estimate the impact of the additive error for realistic surveys, since the redshift, color and morphology
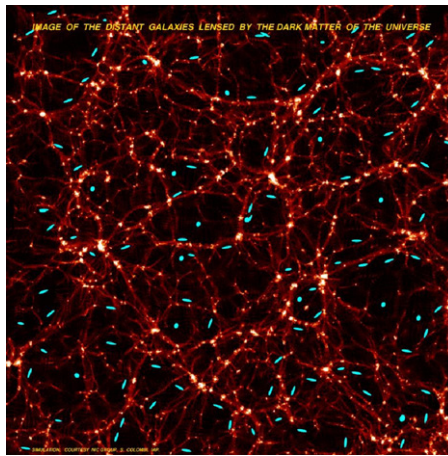
Fig. 19. The blue elongated disks represent observed images of background galaxies. The dark matter filaments from numerical simulations which were used to simulate the survey are also plotted to show alignments of ellipticities of observed galaxies with underlying filamentary structures (Figure courtesy: Stephane Colombi and Yannick Mellier).

dependence might be quite complicated and are not yet well understood. The multiplicative (i.e. calibration) error of the order of one percent does not seem to degrade dramatically the cosmological parameters constraints [133], but this is because the cosmological constraints come from the largest scales, where the error budget is dominated by cosmic variance and not by the multiplicative error [304]. Fig. 18 shows that a large multiplicative error degrades significantly the weak lensing signal at angular scales less than 10 arc min, and has no effect at scales 20 arc min and above. Therefore a complete scientific use of a lensing survey is also dependent on our ability to reduce the multiplicative error, not only the additive error. With the STEP effort [105,193] and the large amount of ground and space based data available from current weak lensing surveys, the shape measurement issue will probably be solved within the next 2 or 3 years. The major source of error for weak lensing survey will then become our ability to estimate the photometric redshifts of the source galaxies [304]. This is a powerful technique, but the redshift error is large and often there are multiple redshift solutions due to spectral features not covered by the set of filters. This is clearly shown in [134], where photometric redshift degeneracies are left with the 5 filters ugriz of the MEGACAM camera. Ref. [133] has shown that the requirement of photometric redshift precision is tight if we want to achieve tomography: for instance the average redshift needs to be accurate to better than 1%. A large number of filters in the optical and near infrared coverage would then be necessary. Ref. [163] finds that the requirements are less severe for 3D weak lensing (see Section 4).

7. Simulations

In order to obtain good signal-to-noise for estimates of cosmological parameters, it is necessary to probe many different scales, including small scales where linear or second-order perturbation theory is not valid. As we have no exact analytical description of matter clustering at small or intermediate scales, numerical N-body simulation techniques are employed to study gravitational clustering in an expanding background. Numerical techniques typically use ray-tracing techniques through N-body simulations to study weak lensing of background sources. Other methods include line-of-sight integration of shear. Although often only limited by computational power, numerical techniques too depend on various approximations which can only be verified by consistency checks against analytical results.

Simulating (strong) lensing by individual objects can provide valuable information regarding background cosmology through the statistics of arcs, see e.g. [288,210] for early studies. Simulating weak lensing surveys on the other hand probes inhomogeneous matter distribution by large scale structure in the Universe. Early attempts to simulate weak gravitational lensing by inhomogeneous dark matter distribution was initiated by various authors in the early 1990s. These studies include [236,144,169,5,16,31]. However the most detailed studies in this direction started emerging by the late 1990s. Ref. [308] following up previous work done by [306,307] presented a detailed analysis of lensing by large scale structure. On a slightly larger angular scale this study was extended and complemented later by the work done by [138] who constructed shear and convergence maps using ray-tracing simulations. With ever increasing computational power the typical size of the sky which can be simulated using ray tracing experiments has increased over the years and recent studies can now focus even on scales comparable to tens of degrees while still resolving smaller angular scales well, see Fig. 19. These numerical developments have also stimulated improved analytical modelling of weak lensing using perturbative techniques at larger angular scales and halo-based models or the hierarchical *ansatz* at small angular scales.
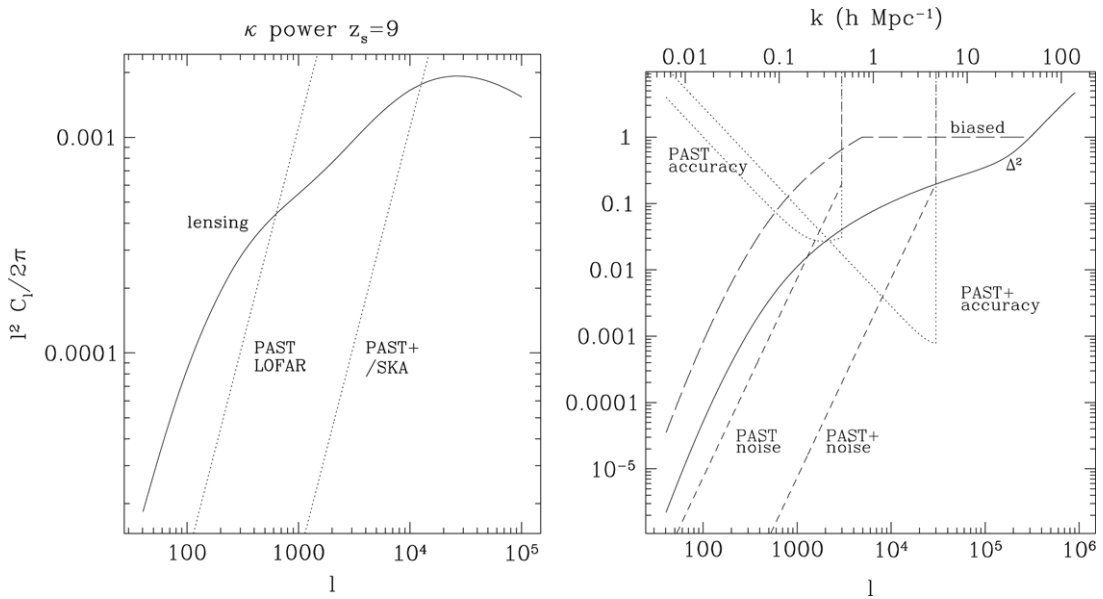
Fig. 20. In the left panel convergence power spectra for redshift $z_S = 9$ are plotted. The dotted line on the left corresponds to noise level expected from PAST/LOFAR where as the dotted line on the right corresponds to noise level expected from second generation PAST+ and the SKA. Measurement errors and accuracy of various surveys in estimating matter power spectra are compared on the right panel. Solid line corresponds to the matter power spectrum at $z = 9$ as in left figure. Dot–dashed line corresponds to power spectrum of patchy reionization with a bias factor $b = 4$ for more details. Dashed lines correspond to noise levels expected for PAST and second generation PAST+. Dotted line corresponds to fractional accuracy of power spectrum estimation per logarithmic l bins. (Figure Courtesy Ue Li-Pen).
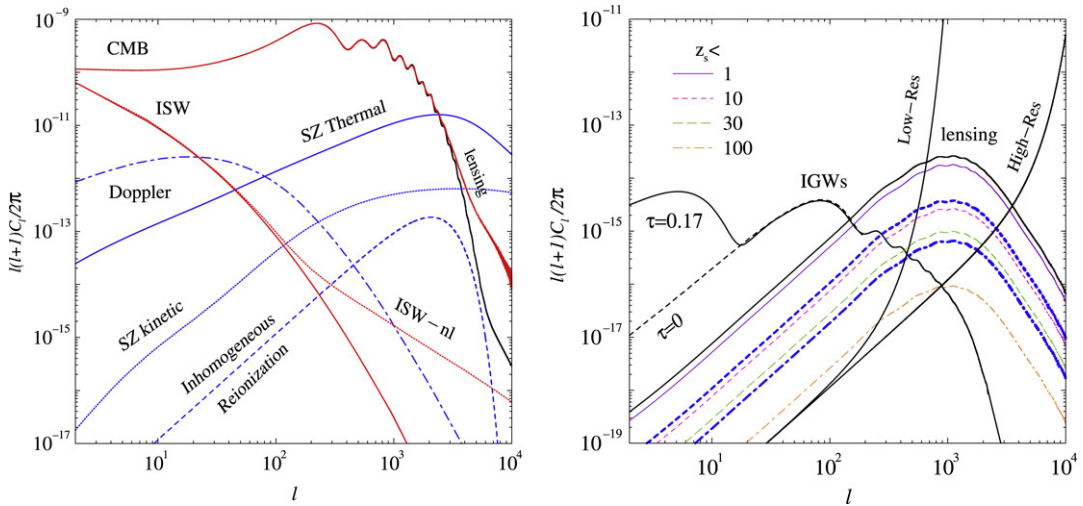

Fig. 21. Left Panel: Power spectrum for the temperature anisotropies in the fiducial ΛCDM model with $\tau = 0.1$. In the case of temperature, the curves show the local universe contributions to CMB due to gravity (ISW and lensing) and scattering (Doppler, SZ effects, patchy reionization). See, Cooray, Baumann and Sigurdson [56] for a review on large scale structure contributions to temperature anisotropies (Figure Courtesy: Asantha Cooray). Right Panel: CMB B-mode polarization. The curve labeled 'IGWs' is the IGW contribution with a tensor-to-scalar ratio of 0.1 with (solid line; $\tau = 0.17$) and without (dashed line) reionization. The curve labeled 'lensing' is the total lensing confusion to B-modes. Thin lines show the residual B-mode lensing contamination for removal of with lensing out to z_s. See, Sigurdson and Cooray [267] for details.

7.1. Ray tracing

In case of experiments involving ray-tracing simulations, one combines several large-scale boxes obtained from cosmological N-body simulations to build a large simulated volume from the observer up to the source plane at redshift z_s. Then, the dark-matter particle distributions within each box are projected on successive two-dimensional planes up to the redshift of the source. Typically up to 30 such planes are employed to sample the matter density to a source redshift of $z_s \sim 1$ and 10^6 rays are propagated through the N-body data volume. The computation of the derivatives of the gravitational potential in each of these lens planes is performed using FFTs. This provides the shear tensor at each plane which allows one

to follow the deflection of the light rays from one plane to the next. The Jacobian matrix $\mathcal{A}$ of the mapping from source to the image plane determines lensing observables such as the convergence κ and the shear components γ_1, γ_2, see Eq. (2.6). Such an algorithm is also known as the multiple-lens algorithm (see e.g. [237] for more detailed discussions).

Various numerical artifacts that determine the resolution of a ray-tracing simulation include the spatial and mass resolution of the underlying N-body simulation through which the ray tracing experiments are being performed as well as the size of the grid which is used to compute the intermediate projected densities and the gravitational potential. The finite size of the simulation boxes on the other hand determines the largest angular scales to which we can reliably use the results from ray-tracing simulations. Depending on the size of the simulation box and source redshift one can typically construct a few degree square patches of the sky. To improve the statistics, the N-body simulation box is rotated and ray tracing experiments repeated, to generate additional weak lensing sky patches.

Studies using ray tracing simulations were initiated by [138]. They used a 256^3 adaptive P^3M simulation outputs from Virgo to perform the ray-tracing simulations. The lens plane grid used to compute the potential and its derivatives from the projected matter distribution had a resolution of 2048^2. Depending on a specific cosmology these studies generated weak lensing maps of a few degrees, with resolution down to sub-arc minutes. Recent ray tracing simulation using multiplane techniques include the ones presented in [94].

7.2. Line-of-sight integration

Ref. [58] pointed out that several problems can arise in weak lensing studies from the use of the multiple-plane approach described in the previous section, especially when the sources are distributed at relatively high redshifts. In particular, the projection of the matter distribution onto successive 2D planes orthogonal to the mean line of sight clearly approximates all angular diameter distances by a constant within a given redshift interval. This may lead to significant errors if these intervals are too large. Thus, Ref. [58] introduced a 3D algorithm which computes the second derivatives of the gravitational potential $\Phi(\mathbf{x})$ within the full 3D volume using FFTs. Then, light rays are followed within the 3D volume and deflections are taken into account along the 3D grid using the local derivatives of the gravitational potential and the local angular distances, which allows one to derive the Jacobian matrix $\mathcal{A}$ between source and observer planes (for more detailed discussions see [58,9, 10]). The variance of the cosmic shear obtained from this algorithm was compared with analytical predictions and other simulations in [11]. More detailed comparisons appear in [12,295,207] where a good agreement was found with a whole range of analytical predictions.

It should be noted that ray-tracing simulations and line-of-sight integrations still remain costly options to simulate a reasonable portion of the sky with fairly low resolution. This limits the number of independent realizations which can be simulated. However, to probe the small angular scales where non-linear gravity has not been understood analytically yet, simulations are the only reliable option against which all analytical predictions are tested regularly.

8. Weak Lensing at other wavelengths

Current weak lensing surveys mostly rely on statistical studies of ellipticities of background galaxies at optical wavelengths. However various authors have considered the possibility of weak lensing studies in other wavebands, both for individual radio or IR sources at high redshift and for the fluctuations in the integrated diffuse emission from unresolved sources [55,219]. It was pointed out that future facilities at radio wavelengths will even start competing with space-based optical observations which are limited by their ability to resolve the shape of distant sources and their small field of view. Radio surveys by the proposed Square Kilometre Array (SKA) will be able to make huge progress in this direction by resolving orders of magnitude more sources [243]. In addition to resolved individual sources it was also suggested that integrated diffuse emission from the first stars and protogalaxies at high redshift ($z_s = 15$–30) as well as 21 cm emission by neutral intergalactic medium can provide useful arenas for weak lensing studies. It was realized that such programmes could be very useful in bridging the gap between weak lensing surveys based on optical studies of nearby galaxies at a redshift of a few and weak lensing studies of the CMB at a redshift of $z_s = 1100$. Nevertheless separating galactic contamination from cosmological signal remains a difficult task, see Fig. 21.

8.1. Weak lensing studies in Radio and near IR

Future radio facilities, such as the proposed SKA,[2] will be superior to current radio observatories by orders of magnitude, particularly in its field of view, and in sensitivity. In addition, the higher resolution achieved by SKA will place it in a much better position than the present generation of radio telescopes. Surveys using SKA will push radio astronomy into a position where the number density of radio sources will be comparable to that of the optical sky (where the number density of useable galaxies is ~ 30 arc min^{-2} up to a redshift of order unity, for ground-based surveys). This is possible thanks to the fact that SKA will be able to observe 100 times fainter objects than currently achievable; the radio sky at present is almost literally

---

[2] http://www.skatelescope.org/.

empty. For effective weak lensing studies the number density n of sources as well as the mean redshift of sources $\langle z_s \rangle$ should be as high as possible. However predictions about these faint radio sources and their $\langle z_s \rangle$ and n is currently less certain. If the dominant population consists of normal or star-forming galaxies the average redshift would be roughly unity. Additional populations of sources can make the redshift distribution less certain. Another complexity in the whole scenario is that we do not know to any accuracy the shape distribution (i.e. the value of σ_ε) of the faint radio sources. Ref. [32] give estimates for the SKA of $\sigma_\gamma = 0.2$ and $n = 500$ arc min^{-2} (Fig. 20). Ideally one would hope for near-spherical sources with no intrinsic ellipticities acting as source objects, i.e. with σ_ε as low as possible. If the radio sources in SKA are dominated by core-jet type objects, then σ_ε can be very high, whereas normal galaxies have relatively lower values. The field of view (FOV) for SKA will be large and clearly the PSF will be controllable; this makes it comparable or probably better than the present generation of optical surveys. As discussed above, seeing provides a fundamental limitation for optical telescopes: as they become fainter, the source galaxies tend to become smaller too. This limits the number density of sources for which the ellipticity can be measured reliably. A situation where point sources dominate resolved source number counts is already present in some of the deepest space-based images available to date. These include the Hubble Deep Fields North and South and recent images from the Advanced Camera for Surveys (ACS) on the Hubble Space Telescope (HST). Clearly the space-based images are much better compared to their ground-based counterparts, but the FOV of such observations is limited. Radio observations using future facilities could be highly productive as they could combine high measurable source density and large FOV. However, these conclusions will depend to some extent on the intrinsic properties of the sources, and further assume that sources are not too elongated and that the average redshift distribution of these sources is not too shallow. Ionospheric effects and how they change the PSF remains to be understood more accurately.

8.2. Possibility of 21 cm weak lensing studies

Usually background objects can be broken down to individual sources at optical and infra-red wavelengths, but the emission of 21 cm radiation [252,182,287,135,79] from neutral gas prior to reionization, and the CMB, provide examples of truly diffuse backgrounds [216,276,268,127].

At high redshifts, typically beyond current large-scale surveys, the unresolved point sources become more dominant. At a source redshift of $z_s = 15$–30, first generations of stars and protogalaxies start to appear according to current theory of galaxy formation. These point-like objects provide a perfect background for weak lensing studies due to the large distances that light rays need to travel from these objects to reach us. Though detection of these objects is beyond present observational technology, the spatial fluctuations in the integrated diffuse background emission can be potentially interesting for lensing studies if we assume the most optimistic emission models.

The analytical formalism for weak lensing studies of diffuse backgrounds has recently been established [55]. Borrowing techniques from studies of weak lensing of the CMB, this shows that a perturbative approach — typically employed to study CMB lensing — will still be valid for diffuse background studies. This is despite the fact that unlike the CMB there is considerable power at small angular scales due to the lack of damping tail. This indicates that a perturbative series has a comparatively slow convergence rate and a larger number of terms need to be included for realistic calculations.

In contrast to CMB lensing studies [314,18,92,126,110], the weak lensing studies based on diffuse components suffer from the fact that the lensing modification to the power spectrum is minor at arc-minute angular scales and the lensing information that one can extract from low-redshift diffuse background is significantly limited. This is related to the presence of significant structure in CMB power spectra, as signified by the acoustics peaks, which is lacking in the case of diffuse background studies. The presence of a damping tail in the CMB means that the convolution associated with weak lensing effects transfers some power from larger angular scales to smaller angular scales at the arc-minute range, which makes it most easily detectable. Use of polarization information in CMB also carries much richer lensing information as compared to unpolarized diffuse background studies. Moreover, at the last scattering surface where the CMB temperature and polarization fluctuations are generated they follow a Gaussian pattern. Then lensing due to the intervening mass distribution imprints a non-Gaussian footprint which can be effectively used to extract cosmological information [22,159]. There have been extensive studies in this direction using higher-order moment-based techniques (see e.g. [54]). By contrast the non-Gaussianity generated by weak lensing in diffuse backgrounds such as the 21 cm background is unlikely to be detected in near future. Nevertheless if possible 21 cm weak lensing studies can extend the reconstruction of the integrated matter power spectrum out to redshifts of 15–30, and will bridge the gap between current and upcoming galaxy lensing studies and the CMB.

8.3. Using resolved mini-halos for weak lensing studies

Concentrating on mini-halos that will contribute to the 21 cm background radiation, [219] found that instruments such as PAST, LOFAR would tremendously improve our knowledge of some key cosmological parameters. Before reionization, most of the baryonic matter in the Universe is in the form of neutral hydrogen. The first gravitational bound objects are the collapsed virialized dark matter mini-halos where this neutral hydrogen resides. These mini-halos [182,135,136] provide a fluctuating background with a characteristic scale that can be used for weak lensing studies.

For weak lensing studies, one would like to have a background at a high source redshift that also exhibits structures at small scales. Clearly the CMB satisfies the first criterium but it is smooth at small scales. It was pointed out that the Universe

at the epoch of reionisation might be the most natural place to look for applications of weak lensing studies. Clearly not only it is at a very high redshift, but also it emits brightly in the hydrogen hyperfine transition line and has structures on many scales ranging from several arcminutes to under a milliarcseconds. Experiments which will target these particular redshifts and wavelengths are being planned, including some that are already undergoing construction, e.g. PAST,[3] LOFAR [158].[4] Other experiments which will have low signal-to-noise include T-REX[5] and CATWALK.[6]

Presenting a detailed calculation of signal to noise analysis [219] argues that weak lensing studies of epoch-of-reionization gas can constrain the projected matter power spectrum to very high accuracy. Use of tomography can further increase the level of accuracy with which certain cosmological parameters can be constrained. It was claimed that with such a technique, the neutrino mass could be constrained with an accuracy of 0.1 meV. The inflationary gravity-wave background and consequently the inflationary dynamics as encoded by the Hubble parameter during inflation can be constrained with high accuracy too. These calculations show that such 21 cm weak lensing observations are an order of magnitude better than those from galaxy surveys. However such optimistic scenarios will require resolving each of the 10^{18} mini halos that will be observed on the sky.

Clearly several problems arise when one tries to map gravitational lensing at such an ambitious scale. For example [213] have shown that synchrotron emission from ionised gas can outshine the 21 cm radiation. However, [79] pointed out that such components can be removed by power-law spectra from spatial fluctuations.

9. Weak lensing of the cosmic microwave background

Observation of cosmic microwave background (CMB) radiation is one of the cleanest probes of cosmology [127,128, 64,130,44,253]. However *lensing* of CMB photons by intervening mass clumps can provide additional information about the structure and dynamics of the Universe. Besides, lensing of the CMB provides information at larger scales and higher redshift than can be reached by any other astronomical observations. Weak lensing of the CMB is responsible for many observable effects which have been studied in extensive detail — for a detailed review see [172]. Calculations of these effects have been made both for temperature and polarisation anisotropies [30,49,176,258,198], see Fig. 21.

9.1. Effect of weak lensing on the temperature and polarisation power-spectrum

Lensing broadens the acoustic peaks and enhances power at small angular scales. These features are non degenerate with the standard cosmological parameters. This allows a determination of the lensing amplitude by comparing the observed spectra with CMB spectra of different mass fluctuations. The magnitude of distortion is sensitive to the level of mass fluctuations as a function of redshift and scale. This in turn depends on the background cosmology. In this way lensing of CMB can be used as a window to probe the fluctuations in the dark matter distribution over a huge range of redshifts and length scales.

Lensing generates a non zero B-mode polarization from a purely E-mode. (Note that here we are referring to E and B modes in the CMB polarisation map, not in the shear map). B-modes generated during inflation by tensor mode perturbations or gravitational waves produce a distinct spectrum which can be used to discriminate between different classes of inflationary models. Lensing of E-modes produces B-modes which dominate the more primordial signal on small scales, and which are considered mainly as a source of confusion in polarisation experiments. Detection of a primordial B-mode signal in the presence of lensing therefore pushes observational strategies towards favouring larger sky coverage [157,259]. A low sky coverage and presence of boundaries also causes additional confusion by introducing mixing of E and B modes. It is however useful to note that as the inflationary B-mode signal is mainly significant on large angular scales experiments with low resolution can also be very promising. High resolution B-mode detection experiments will typically employ a "delensing" step in data reduction to effectively restore the unlensed sky from the lensed data.

Typically the power spectrum of the lensed map is computed by a series expansion in the deflection angle. A perturbative expansion in the deflection angle is a transparent way to understand most of the lensing effects. Non-perturbative evaluations of lensing effects are carried out by considering the correlation function [258,45,51,315,55,183].

9.2. Non-Gaussianity in the CMB induced by weak lensing

Primordial perturbations produced during inflation are very nearly Gaussian and the linear evolution of these perturbations up to the last-scattering surface does not generate any non-Gaussianity. Weak lensing by the intervening matter distribution however does introduce non-Gaussianity in maps of the CMB sky [315].

All odd-order correlation functions vanish for a Gaussian random field. On the other hand weak lensing generates a non-zero contribution through correlations between the large-scale temperature and lensing potential. This cross-correlation

---

[3] http://astrophysics.phys.cmu.edu/jbp/past6.pdf.

[4] http://www.lofar.org/.

[5] http://orion.physics.utoronto.ca/sasa/Download/poster/casca_poster.pdf.

[6] ftp://ftp.astro.unm.edu/pub/users/john/AONov03.ppt.

which is due to the Integrated Sachs–Wolfe (ISW) effect at large angular scales can therefore be a very useful tool to probe the growth of perturbations and the expansion history of the Universe [125,260,87,84–86]. This implies that such studies can be very useful tools for studying the dark energy equation of state [275] or the neutrino mass [170]. These correlations are negligible on smaller scales. Besides non-linear evolution of the matter distribution as well as late time non-linear effects including the Sunyaev–Zeldovich (SZ) effect also contribute to the bispectrum. The four-point correlation function is the lowest order non-zero correlation function which does not vanish in the absence of any the cross-correlation between the low redshift mass distribution and the CMB temperature distribution. The non-Gaussianity studies involving polarisation fields are very similar to the temperature case, at least for the E-mode polarisation. Various combinations of four-point correlation functions involving E- and B-mode polarisations have been studied in the literature [22,123]. For future high resolution all-sky polarisation surveys such studies will be feasible.

9.3. Weak lensing effects as compared to other secondary anisotropies

The thermal Sunyaev–Zeldovich (tSZ) effect, which is caused by the scattering of photons from hot electrons in clusters, is a dominant anisotropy contribution on small scales. Due to a very characteristic frequency spectrum such a component can however be readily separated from primordial anisotropies. Another secondary contamination, the kinetic Sunyaev–Zeldovich (kSZ) effect, has the same frequency dependence as the primary anisotropies, so is harder to separate. Similarly, lensing does not cause any frequency shift in an otherwise perfect blackbody spectrum of primary CMB. Thus non-linear sources, such as kSZ are potential sources of confusion, when trying to understand the effect of lensing on the CMB. Current uncertainties in the reionization history and topology of reionization patches also make it more difficult to model. For polarisation spectra the kinetic SZ is sub-dominant, simplifying the situation to some extent [293,82,43,266].

9.4. Lensing of the CMB by individual sources

On small scales, the CMB lacks power. As mentioned earlier, most of the power is generated by secondary anisotropies and transfer of power from larger scales to smaller scales due to lensing. This raises the possibility of detecting individual cluster-mass objects in CMB maps by their effect of lensing on the CMB. Unlike other probes such as the SZ which depends on baryon physics, such studies can constrain the physical mass distribution of individual objects directly [171,65,53].

9.5. Future surveys

In the future, satellite experiments such as Planck[7] (to be launched in 2008) will be in a good position to detect the effect of lensing in temperature power spectra. In the case of polarisation, experiments such as CLOVER[8] and QUIET,[9] which are being planned, will have detection of B-mode from inflation as their primary science driver [173,206,274,175]. Ongoing experiments such as QUaD,[10] may reach the required sensitivity, but for all of these, lensing is the main source of confusion on small scales for such experiments.

10. Weak lensing and external data sets: Independent and joint analysis

Weak lensing is a very powerful probe of the projected dark matter clustering, and in principle it is very good at constraining the cosmological parameters playing a dominant role in the structure growth. The main limitation comes from the strong degeneracy between the dark matter power spectrum normalisation σ_8 and the matter density Ω_m (see the introduction of Section 5 and Eq. (2.9)). These two parameters are degenerate because any change in Ω_m can be balanced by an appropriate change in σ_8 slowing down or accelerating the growth rate. In [21] it was shown that the shear variance at scale θ_s scales roughly as

$$\langle \bar{\gamma}^2 \rangle_{\theta_s} \propto \sigma_8^2 \Omega_m^{1.5} z_s^{1.5} \theta_s^{-\frac{(n+2)}{2}} . \tag{10.1}$$

This equation, which is the first term of the perturbation series on the mass density contrast, assumes a power-law power spectrum with constant slope n and a single source redshift z_s. It has a very limited application but it has a pedagogical value in that it shows that the parameter degeneracy between σ_8 and Ω_m extends to the source redshift as well. Therefore, weak lensing in 2D can become a high precision cosmology tool only if it is combined with another cosmology probe and provided we have a *good* knowledge of the source redshift distribution. The simultaneous observation of non-linear and linear scales in lensing surveys shows some features in the projected mass power spectrum which helps to lift this degeneracy [137].

---

[7] http://www.rssd.esa.int/index.php?project=Planck.
[8] http://www.astro.cf.ac.uk/groups/instrumentation/projects/clover/.
[9] http://quiet.uchicago.edu.
[10] http://www.astro.cf.ac.uk/groups/instrumentation/projects/quad/.

Alternative approaches which can also lift degeneracies were discussed in Section 4, using 3D information, and in Section 5, using higher-order correlations beyond the shear variance. However, like any other cosmology probe, this is not enough for weak lensing to be a high precision cosmology tool alone. In this section we review the advantages of combining lensing with different probes and we outline the gain on cosmological constraints in the future missions.

10.1. With CMB, supernovae and baryon acoustic oscillations to probe cosmology

Weak lensing alone provides a measure of $\Omega_m^{0.7}\sigma_8$, provided that the redshift of the sources is known. This means that weak lensing best performance is in the measurement of the amplitude of the projected mass power spectrum. For this reason, it is very powerful at breaking the parameter degeneracies seen in other cosmology probes, which are usually sensitive to other combinations of cosmological parameters. It is known, for instance, that a precise measurement of σ_8 and Ω_m can be obtained from the combination of lensing and CMB [302,50]. Fig. 22 shows the set of parameters to be combined for an optimal joint CMB-lensing analysis [286]. This result, obtained for the CFHTLS and WMAP1 surveys, is not modified for a different choice of lensing and CMB data sets. Note that the best improvement is obtained on parameters which the shape of the dark matter power spectrum is the most sensitive to: the mass density Ω_m, the power spectrum normalisation σ_8, the reduced Hubble constant h, the primordial power spectrum slope n_s and the running spectral index $\alpha = -\mathrm{d}\ln(n_s)/\mathrm{d}\ln k$.

For the lensing signal alone, an improvement of a factor ~ 3 in the parameter errors is expected if the lensing signal is combined for different source redshift slices instead of measured from the broad source distribution [280]. This is the well known tomography technique which requires the measurement of photometric redshifts (see Section 4.3). Unfortunately, for these parameters, the improvement cannot be further increased with a larger number of source slices: one can show that the signal-to-noise saturates for a maximum of 3–5 redshift slices [281], which is a consequence of the fact that the lensing selection window is a rather flat function of redshift where the signal is the strongest. Another source of improvement for the lensing constraints is the use of higher-order statistics ([280], see Section 5 of this review): the probe of the non-linear regime of structure formation helps considerably in the determination of the precise moment when large scale structures become non-linear and at which scale. This event is a strong function of the cosmological parameters, in particular of dark energy [188,17]. Some measurement of high order statistics have been done [25,218], but this area of research is still in its infancy.

A major science driver for cosmology has become the measurement of the Dark Energy equation of state. The Dark Energy Task Force report (DETF) [2] and the ESA-ESO working group report [215] are summaries of where cosmology is heading to for the next decade: there is a consensus among cosmologists that the goal of measuring the dark energy parameters can only be achieved from the joint analysis of several cosmological probes. Fig. 23 shows the dark energy parameters forecast for the future experiments (which includes a pessimistic and optimistic cases). Most of the panels on this figure are extracted from the DETF report, and they show the various degeneracies for different cosmological probes. The three projects that DETF has considered are the following:

- Baryon oscillations: 20,000 square degrees, ground-based survey. Photometric redshifts cover the 0.2–3.5 range, and their precision is 0.01 for the optimistic case and 0.05 for the pessimistic one.
- Supernovae: ground-based survey with 300,000 supernovae. The photometric redshift accuracy is $0.01(1 + z)$ for the optimistic case and $0.05(1 + z)$ for the pessimistic.
- Weak lensing: 20,000 square degrees, ground-based survey. The shear calibration is $f_{\mathrm{cal}} = 0.01$ and photometric redshift accuracy $\sigma_z = 0.01(1 + z)$ for the pessimistic case. $f_{\mathrm{cal}} = 0.001$ and $\sigma_z = 0.001(1 + z)$ for the optimistic case.

Note that these surveys are all providing predictions of very accurate determination of the dark energy equation of state w_p and energy density Ω_{de}, far better than any joint analysis would do today [272]. Here w_p is the equation of state at an intermediate redshift, typically around 0.4. The bottom right panel on Fig. 23 is from [280] and shows the joint constraints on w_p and Ω_{de} from the future CMB PLANCK mission and a lensing survey covering 4000 square degrees, combining the two and three-points statistics. Fig. 23 shows that the supernovae, CMB and lensing (or BAO) have very different degeneracies in the dark energy parameter space, which offers an optimal complementarity in the combination of cosmology probes. It is believed that only the combination of all probes together will provide convincing constraints regarding the dark energy, although each individual probe seems to predict very accurate results. The main limitation being the systematics, it is indeed important to have more constraints than parameters we wish to measure: weak lensing for instance may appear as the most powerful probe. However, the lensing signal is rather featureless compared to CMB and BAO, which makes it more vulnerable to systematics like shear calibration and photometric redshift inaccuracies (see Section 6). The future of cosmology certainly lies in a joint analysis of surveys, and lensing surveys play a particular role in the sense that this is the only probe which can provide an unbiased measurement of the dark matter fluctuations amplitude. Note that the constraints on quintessence models can be improved by the combination of various cosmology probes, such as lensing and SNeIa as demonstrated in [235].
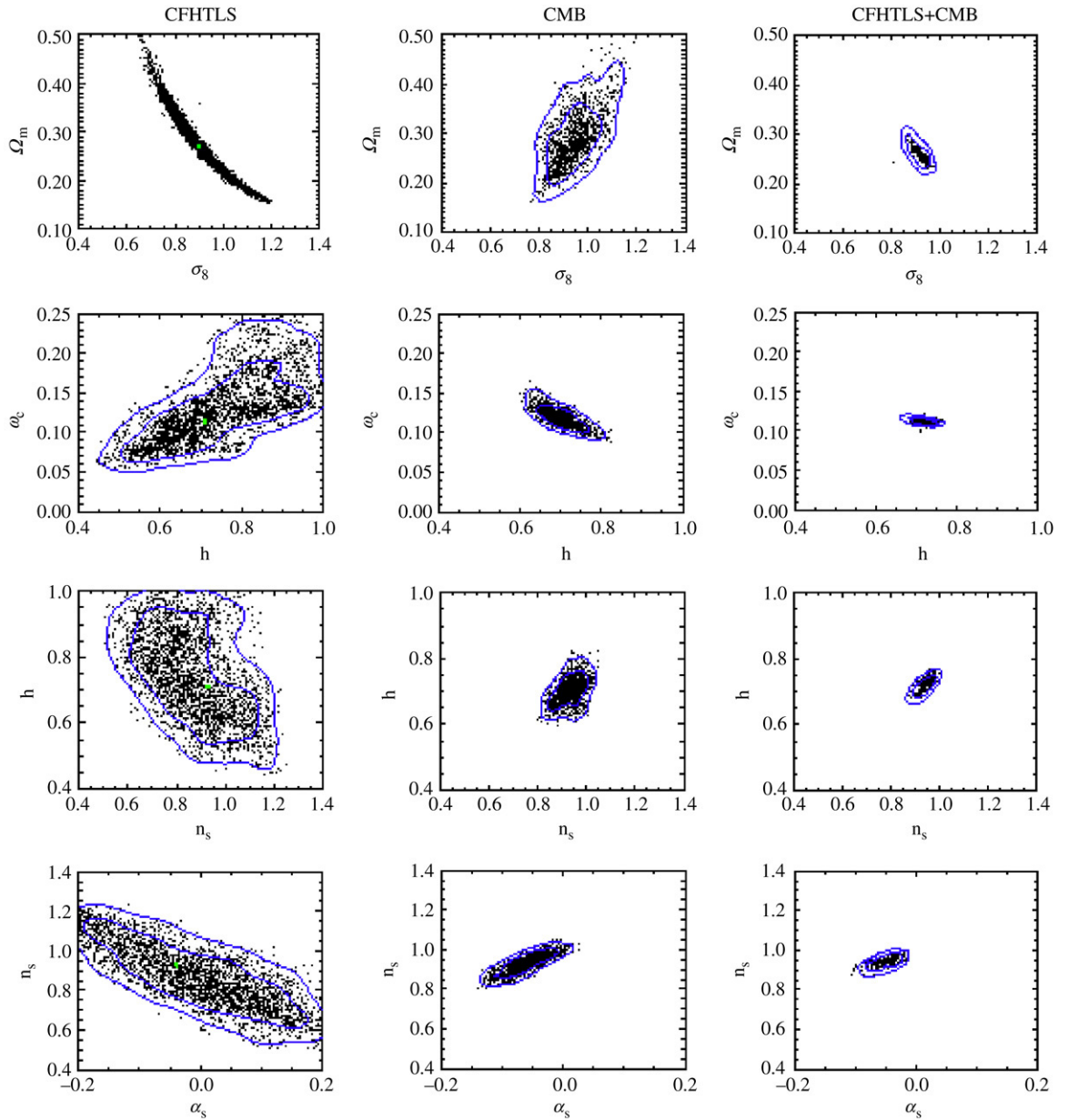
Fig. 22. Figure showing the most orthogonal parameter degeneracies between CMB (WMAP1) and weak lensing (CFHTLS). The set of parameters is Ω_m, σ_8, $\omega_c = \Omega_c h^2$, n_s, α_s and h (from [286]).

10.2. Beyond-Einstein gravity

The success of the joint analysis depends on the validity of our Cold Dark Matter and Dark Energy picture. Given the unknown nature of these ingredients, it is possible that our description might be incomplete or wrong. We must therefore keep an open mind and consider alternative interpretations of the data.

Perhaps the most exciting new aspect of weak lensing on large scales is that it has the capability in principle to test the Einstein gravity model. This is because it probes two effects, the distance–redshift relation and the growth rate of perturbations. In General Relativity, these both depend on the evolution of the Hubble parameter, but in other theories, the relationship between the expansion history and the growth rate is different. One can always match a given expansion history of a modified gravity model within the standard model, by adjusting the dark energy equation of state parameter, but it is harder to reproduce the growth rate as well [132,177,168,142]. For string-inspired models involving extra dimensions, the growth rate of fractional density perturbations δ is given quite accurately as a function of scale factor a and matter
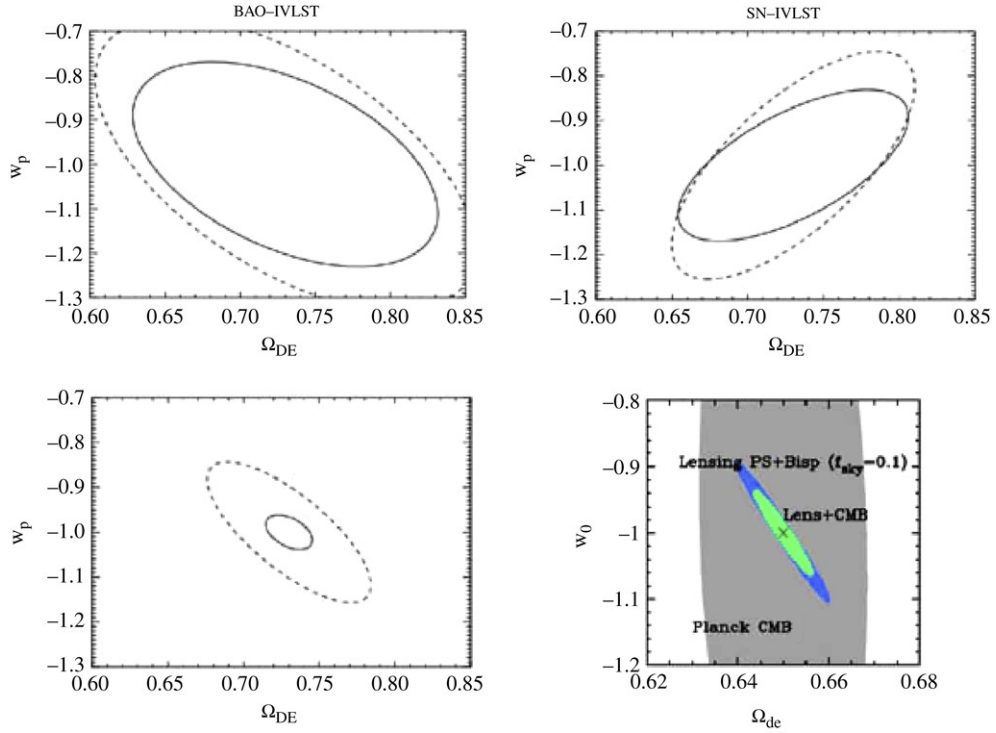
Fig. 23. Panels showing the measurement forecast of the dark energy equation of state parameter w_p and dark energy density Ω_{DE} from the baryon oscillations (top-left panel), supernovae Ia (top-right panel) and weak lensing (bottom-left) from the DETF report (2006). w_p is the equation of state parameter of the Dark Energy parameter at an intermediate 'pivot' redshift, usually a little less than 0.5. Solid and dashed lines are for optimistic and pessimistic surveys respectively. The surveys characteristics are described in the text. The bottom-right panel shows the constraints from the PLANCK CMB experiment with a lensing survey [280].

density parameter $\Omega_m(a)$ by

$$\frac{\delta}{a} = \exp\left\{\int_0^a \frac{da'}{a'}\left[\Omega_m(a')^\gamma - 1\right]\right\}, \tag{10.2}$$

where $\gamma = 0.68$ for the DGP braneworld model, and General Relativity is accommodated by $\gamma = 0.55$. Analysis of possible future space-based lensing experiments such as DUNE shows that it should be very feasible to distinguish Einstein gravity from the flat DGP braneworld model at very high significance [101,4].

The modified gravity theory MOND proposed by [202] lacks a solid physical motivation and it appears to be unable to explain the halo flattening seen in weak lensing data [118]. Nevertheless, this study initiated the idea that a modified theory of General Relativity could solve the dark matter and dark energy problems. These models include the string-motivated braneworld scenarios [70]. Ref. [290] suggested that modified gravity can be tested directly from a testing of the Poisson equation

$$\nabla^2 \Phi = 4\pi G \rho, \tag{10.3}$$

which may be modified in alternative gravity theories. The gravitational potential Φ can be measured from weak lensing by large-scale structures, and the mass density ρ from the galaxy distribution, which at large enough scale can be assumed to be an unbiased tracer of the mass distribution, as shown in [305] from the 2dF Galaxy Redshift Survey.

A general problem with modified theories of gravity is the significantly increased level of degeneracy due to a larger number of degrees of freedom. As pointed out by [132], it is necessary to measure independently the growth rate of structures and the Universe expansion rate in order to reduce the degeneracy to a reasonable level. Modified gravity also might not be the cause of all the dark components of the Universe. The investigation of a realistic mix of dark component and modified gravity in [132] shows that neglecting the modified gravity severely biases the dark energy parameters, even with a joint Supernovae, CMB and weak lensing constraints. To make things worse, the addition of inflation parameters introduces quantum correction, the running spectral index, to the primordial mass power spectrum which is a scale-dependent effect. Yet another degree of complication comes from the small-scale amplitude prediction which is highly non-linear. Dark Matter itself could also be self-interacting as suggested by [40], resulting in density-dependent observational effects [321].

The present situation is that the simple Big-Bang scenario (i.e. no alternative theories) will indeed be accurately constrained by a joint analysis of different surveys. A general scenario including alternative theories might be harder to

constrain. Whether or not this is possible with the next generation of surveys remains to be demonstrated, but it is clear that weak lensing by large scale structure plays a central role in being sensitive to the "dark matter" whether it is real dark matter or modified gravity.

10.3. With galaxy surveys to probe bias

Weak lensing is the only reliable technique able to probe the dark matter distribution up to redshift of a few using optical surveys, or at even higher redshifts from lensing of the CMB and the 21 cm line. The peculiar velocity field, which is also an unbiased tracer of the matter distribution, is no longer accurate at distances larger than a few hundred Megaparsecs. The combination of lensing with the galaxy distribution is therefore a unique way of constraining the relative amount of matter with respect to light, the so-called bias. This can be done out to reasonably high redshift, giving astronomers access to the dark side of galaxy formation over a wide range of its evolutionary history.

10.3.1. Galaxy biasing

An apparent limitation of lensing surveys is that the mass is only seen in projection, impeding a 3-dimensional probe of the bias. A method for alleviating this problem was proposed by [296] and [241]. It is an alternative to the 3D mass reconstruction technique discussed in Section 4, which was designed specifically for potential or density measurements. We assume a population of foreground galaxies with a known narrow redshift distribution $n_f(z)$ centered on z_f (in units of arc min^{-2}), from which we want to measure the mass-to-light ratio. The lensing signal is measured from a background galaxy population which can have a broad redshift distribution $n_b(z)$ (normalized to unity), while the technique discussed in Section 4 requires an estimate for all redshifts. The cross-correlation of the lensing signal with the foreground galaxy density distribution provides a measurement of the bias at redshift z_f. The scale dependence of the bias can be obtained by filtering the lensing signal and the galaxy density with an aperture filter, which is a narrow band filter (Fig. 2).

Assuming that the galaxy number density contrast δ_{gal} is proportional to the matter density contrast δ with the proportionality factor defined as the bias parameter b, the lensing-galaxy density cross-correlation at scale θ_s is given by [296]:

$$\langle M_{ap}(\theta_s) \mathcal{N}(\theta_s) \rangle = b\pi\theta_s^2 \int_0^{\chi_{max}} d\chi\, \hat{n}_f(\chi) \frac{\hat{w}(\chi)}{\mathcal{D}^2(\chi)} \int \frac{d\ell}{2\pi} \ell\, P\left(\frac{\ell}{\mathcal{D}(\chi)}; \chi\right) W_{M_{ap}}^2(\ell\theta_s), \tag{10.4}$$

see Eqs. (2.9)–(2.12), (3.4) and (3.10) in Sections 2 and 3. Here the weight $\hat{w}(\chi)$ along the line of sight depends on the redshift distribution $n_b(z)$ of the background sources as in Eq. (2.10) whereas $\hat{n}_f(\chi)$ is the redshift distribution of the foreground galaxies (with $\hat{n}_f(\chi)d\chi = n_f(z)dz$) of "number counts" $\mathcal{N}$ with respect to the aperture of radius θ_s. $P(k; \chi)$ is the time-evolving 3-D matter power spectrum (where χ is a parameterization of the redshift along the line of sight) and $W_{M_{ap}}^2(\ell\theta_s)$ is the square of the Fourier transform of the aperture filter, which peaks at some effective wavelength $\ell_{eff} \sim 5/\theta_s$, see Fig. 2. For a narrow foreground redshift distribution, the function $\hat{n}_f(\chi)$ peaks at some radial comoving distance $\chi_f(z_f)$. Eq. (10.4) shows that the cross-correlation is dominated by $P(k_{eff}; \chi_f)$ where $k_{eff} \sim 5/(\mathcal{D}(\chi_f)\theta_s)$. In order to extract the bias parameter b, we need to define the variance of the number density fluctuations for the foreground galaxies:

$$\langle \mathcal{N}^2(\theta_s) \rangle = b^2 (\pi\theta_s^2)^2 \int d\chi \frac{\hat{n}_f^2(\chi)}{\mathcal{D}^2(\chi)} \int \frac{d\ell}{2\pi} \ell\, P\left(\frac{\ell}{\mathcal{D}(\chi)}; \chi\right) W_{M_{ap}}^2(\ell\theta_s), \tag{10.5}$$

and define the ratio R

$$R \equiv \frac{\langle M_{ap}(\theta_c) \mathcal{N}(\theta_c) \rangle}{\langle \mathcal{N}^2(\theta_c) \rangle}. \tag{10.6}$$

The quantity R is proportional to the inverse bias factor b. It was shown in [296] that R is nearly independent of scale for all cosmologies and any dark matter power spectrum, unless the bias parameter is scale-dependent (this statement was shown to be valid in the non-linear regime as well). The bias at angular scale k_{eff}^{-1} and redshift z_f can therefore be measured from weak lensing data.

Refs. [116,269] have performed the only application of this technique. Ref. [116] measured the bias from a combination of the VIRMOS [302] and RCS [114] surveys, which is shown on Fig. 24. This analysis shows a significant scale dependence of the bias, although its calibration is still uncertain due to incomplete knowledge of the source redshift distribution. With the GaBoDS surveys, [269] found $b = 0.8 \pm 0.1$ and a cross-correlation coefficient $r = 0.6 \pm 0.2$, which is consistent with [116]. The cross-correlation coefficient r measures the stochasticity of the biasing and is defined as:

$$r = \frac{\langle M_{ap}(\theta_c) \mathcal{N}(\theta_c) \rangle}{\langle \mathcal{N}^2(\theta_c) \rangle^{1/2} \langle M^2(\theta_c) \rangle^{1/2}}. \tag{10.7}$$
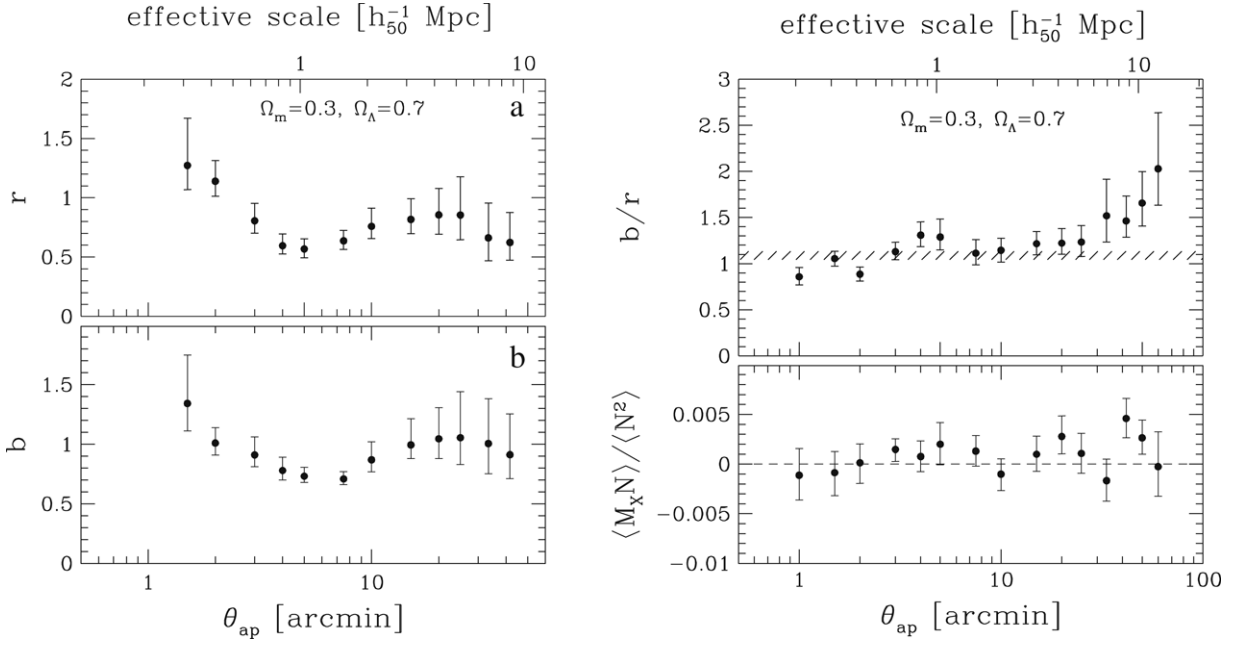
Fig. 24. Galaxy biasing constraints from the VIRMOS and RCS weak lensing surveys [116]. The left panel shows the cross-correlation coefficient r and biasing b as function of scale. The right panel, top plot, shows the ratio b/r and its prediction for a concordance model $\Omega_m = 0.3$, $\Omega_\Lambda = 0.7$. The bottom plot shows the most convincing test of residual systematics obtained by rotating the lensed galaxies by 45°, which is supposed to cancel the lensing signal.

10.3.2. Galaxy–galaxy Lensing

The probe of galaxy biasing can be extended down to galactic halo scales with a technique called galaxy–galaxy lensing. First proposed by [289] and then formalised by [35], the idea is to cross-correlate the shape of distant lensed galaxies with foreground galaxies. As shown in the left panel of Fig. 25, the background galaxies lensed by a foreground galactic halo are preferentially tangentially aligned with respect to the foreground galaxy. The situation is identical to lensing by a cluster of galaxies, but the lensing by individual galaxies is much weaker, since the amplitude of the effect scales as the mass of the lens. To measure the galaxy–galaxy lensing, one must therefore stack the lensing signal behind a large number of foreground lenses. The average shear as function of angular distance from the center gives an estimate of the average halo profile around the foreground galaxies (see right panel in Fig. 25).

The tangential shear of a lensed galaxy at position angle θ with respect to the lens on the sky is given by

$$\gamma_t = -e_1 \cos(2\theta) + e_2 \, \sin(2\theta). \tag{10.8}$$

It is straightforward to show that, when averaged over all position angles, the mean tangential ellipticity is unchanged if a constant is added to the galaxy ellipticity $\vec{e} = (e_1, e_2)$. For this reason, galaxy–galaxy lensing is robust against an imperfect Point Spread Function (PSF) anisotropy correction, as long as the latter is a slowly-varying function of position. The lensing signal is therefore relatively easy to measure, even if the amplitude of the signal is low.

Given that the foreground galaxies span a large range of velocity dispersion and luminosity, scaling relations are needed in order to calibrate the expected lensing signal to the same *fiducial* galaxy with luminosity $L_\star$ and size $s_\star$. If $\sigma_\star$ is the velocity dispersion of the fiducial galaxy, the scaling relations are:

$$s = s_\star \left(\frac{\sigma}{\sigma_\star} \right)^2 ; \qquad \frac{L}{L_\star} = \left(\frac{\sigma}{\sigma_\star} \right)^\eta , \tag{10.9}$$

where the latter corresponds to the Tully–Fisher or Faber–Jackson relation for spiral and elliptical galaxies respectively if $\eta = 1/4$. (L, s, σ) are the luminosity, scale and velocity dispersion of one foreground galaxy. The lens mass model chosen by [35] is a truncated isothermal sphere (TIS), which is also frequently used by several authors [131,118]. The mass density of the TIS is given by

$$\rho(r) = \frac{\sigma^2 \, s^2}{2\pi G r^2 (r^2 + s^2)}, \tag{10.10}$$

whose total mass M_{tot} is [118]:

$$M_{\text{tot}} = 7.3 \times 10^{12} h^{-1} M_\odot \left(\frac{\sigma}{100 \text{ km s}^{-1}} \right)^2 \left(\frac{s}{1 \text{ Mpc}} \right). \tag{10.11}$$
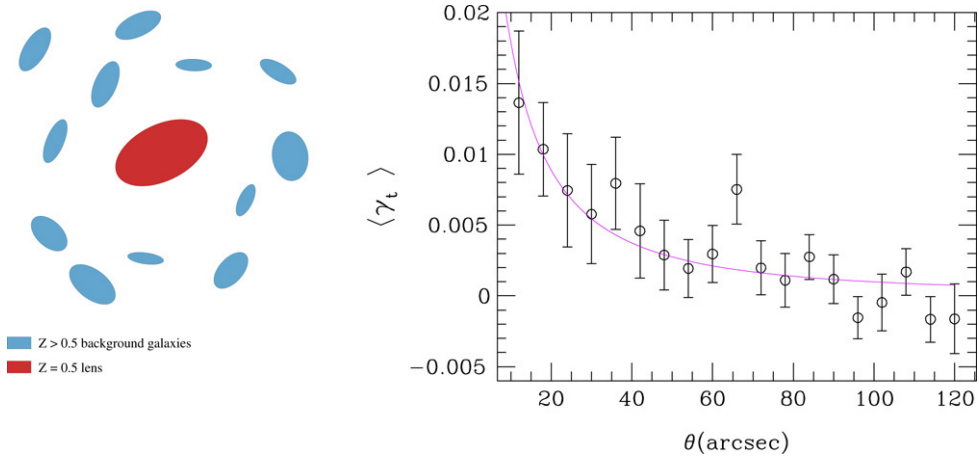
Fig. 25. Left panel: Schematic illustration of galaxy–galaxy lensing. Right panel: Galaxy–galaxy lensing signal from the GEMS survey (Heymans et al. [107]). The solid line shows the best fit NFW mass profile, assuming an average lens redshift of $z_l = 0.65$.

The tangential shear is calculated from the mass model (e.g. Eq. (10.10)), and can be compared to the data provided that an estimate of the lens and source redshifts is known. In general, the free parameters measured with galaxy–galaxy lensing are the fiducial velocity dispersion $\sigma_\star$ and truncation radius $s_\star$ of an $L_\star$ galaxy. The apparent magnitude of each foreground lens is used to estimate its absolute luminosity L (which may require an appropriate k-correction to be included), then the velocity dispersion σ is obtained from the scaling relations. The maximum likelihood technique developed by [240] ensures an optimal analysis, in particular if individual photometric redshifts can be obtained. Note that simple mass models such as the singular isothermal sphere (SIS) do not have a truncation radius:

$$\rho(r) = \frac{\sigma^2}{2\pi G r^2},$$
(10.12)

in which case one could constrain the scaling relations, Eq. (10.9), like the parameter η, in addition to the fiducial velocity dispersion $\sigma_\star$. Ref. [131] and [165] measured a η parameter very close to the Tully–Fisher and Faber–Jackson relation.

At low redshift, the most extensive galaxy–galaxy lensing analysis was performed by [93] on the SDSS data set. They found a Virial mass $M_{200} = 5$–$10 \times 10^{11}\, h^{-1} M_\odot$ for $L_\star = 10^{10}\, h^{-1} L_\odot$, depending on the galaxy color and morphological type. In the redshift range 0.2–0.7 a Virial mass of $M_{200} = 4$–$8 \times 10^{11}\, h^{-1} M_\odot$, the less massive corresponding to the bluest galaxies [104, 165]. Ref. [263] measured the galaxy-mass bias from the SDSS galaxy–galaxy lensing signal, and found a constant bias over correlation coefficient ratio $b/r = 1.3 \pm 0.3$ for $\Omega_m = 0.27$, which is in agreement with the cosmic shear study presented in Section 10.3.1 (see Fig. 24).

Recent studies use the Navarro–Frenk–White density profile as the parametric mass model, which is particularly well suited for galaxy–galaxy lensing in more massive structures such as galaxy groups [115] and galaxy clusters [211,81]. In [186] the authors measured the lensing around Luminous Red Galaxies (LRG) from the Sloan Digital Sky Survey. The LRG sample was split into a bright and faint sample at $M_{cut} = -22.3$. LRG are particularly good foreground targets for probing larger mass halos because they are known to be present in the core of groups and cluster of galaxies. Fig. 26 shows the measured signal against several mass models. It is particularly interesting to note that the flattening of the dark halo profile is clearly visible, leading to a concentration parameter of $c \sim 5$–7, in perfect agreement with Cold Dark Matter predictions [212].

Ref. [104] marginally measured a halo over lens ellipticity ratio of $e_h/e_g \sim 0.8 \pm 0.2$, consistent with the Cold Dark Matter Scenario [69]. A significant, but contradictory, measurement is shown in [185], who found $e_h/e_g = 0.1 \pm 0.06$ for red galaxies and 0.8 ± 0.4 for blue galaxies. The baryon fraction can also be measured by galaxy–galaxy lensing from a comparison of the lensing to the stellar mass. Ref. [119] and [107] find a virial to baryon mass-to-light ratio between 50 and 100, and they show that massive early type galaxies have a stellar to total baryon fraction of $\sim$10%, which indicates that these galaxies are not efficient at producing stars.

10.4. With Sunyaev–Zeldovich studies to probe small scale baryonic physics

The energy of the CMB photons is boosted by scattering on the free electrons contained in the plasma of the Intra Cluster Medium (ICM). It is the source of the Sunyaev–Zeldovich (SZ) effect, which shifts the spectral energy distribution of CMB photons for the lines-of-sight containing hot, ionized, gas. The SZ effect is a probe of the hot baryon distribution, which can be compared to stellar and lensing mass distributions in order to learn about the cluster physics. If one assume that the gas is isothermal, SZ is a measure of the electronic density $n_e(\vec{\theta}, z)$ projected along the line of sight:

$$y(\vec{\theta}) = \frac{kT}{m_e c^2} \sigma_T \int dz\, n_e(\vec{\theta}, z),$$
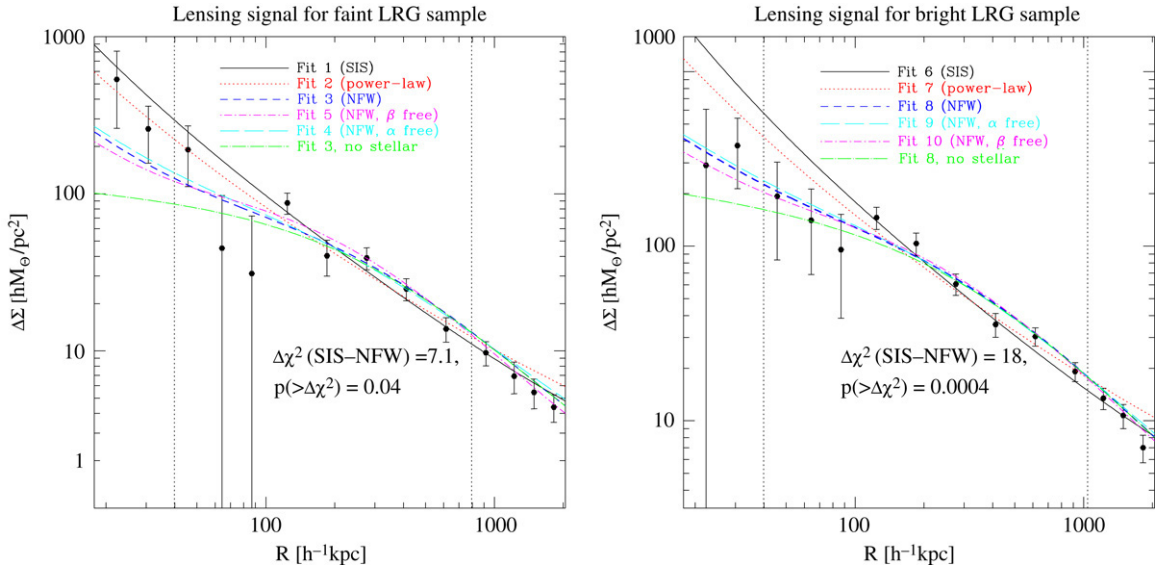(10.13)

Fig. 26. Galaxy–galaxy lensing signal for the Luminous Red Galaxies (LRG), used as tracers of galaxy groups and small clusters [186]. 43335 LRG from the Sloan Digital Sky Survey were used. The left and right panels correspond to faint ($M_r > -22.3$) and bright ($M_r < -22.3$) samples respectively.

where σ_T is the Thompson scattering cross-section and T the temperature of the gas. The SZ effect is therefore independent on the cluster redshift, as opposed to the lensing effect which has its maximum sensitivity at mid distance between the observer and the sources. Lensing and SZ are complementary because they are both linear in the density: for this reason they probe the same regions of galaxy clusters, while X-rays for instance scale as the density squared, which is more sensitive to the cluster core.

One approach of the combined SZ and lensing data sets analysis consists in working on individual clusters. Both data sets can be used to predict the X-ray emission of the cluster [68], which provides a direct test of the cluster dynamical equilibrium. The 3-dimensional halo shape (assuming axial symmetry) can be reconstructed from the combination of SZ, lensing and X-ray observations [317,222]. Ref. [255] have shown that large lensing and SZ surveys (a few hundred square degrees) would be able to detect the evolution of the mass-SZ luminosity relation with redshift, which in turn is a measure of the cluster baryonic physics. This is particularly important for the understanding of the source of energy maintaining the temperature of the intra-cluster plasma at high temperature. The other approach is statistical, when the SZ and convergence maps correlations are measured statistically; one does not focus on individual cluster detection this time, rather one tries to constrain the statistical properties of the cluster population like its baryonic and total mass function, luminosity function, etc. One of the goals then is to use the cluster number counts to probe cosmology [15], the lensing data is used to measure the cluster masses. But this requires a full sky survey with a mass sensitivity down to a few $10^{14} M_{\odot}$ to provide interesting constraints.

One should remember that cluster masses derived from lensing are subject to large noise and projection effects [113, 311], although recent studies seem to show that the discrepancy between dynamical, lensing and X-ray masses is rather small [108]. The ideas developed around the combination of SZ and lensing yet remain to be put into practice: instruments such as the Cosmic Background Interferometer, Atacama Cosmology Telescope, Arcminute Imager and South Pole Telescope, all with angular resolution of the order of a few arcminutes, are very promising for this purpose. The understanding of cluster physics from SZ and lensing is not without any consequences for cosmological studies: statistical lensing for instance probes the projected mass power spectrum down to arbitrarily small angular scale (if the statistical noise is low enough). At the cluster scale, typically one arcminute, we know that baryon cooling and heating modify the cluster gravitational potential well, and therefore the dark matter distribution itself. Ref. [318,312] have shown how the cluster physics could affect the power spectrum by ∼10% below one arcminute. Taking into account this effect might be necessary for the next generation of high precision weak lensing studies.

10.5. Weak lensing of supernovae and effects on parameter estimation

Type Ia supernovae (SNeIa), which are believed to be the thermonuclear explosion of an accreting white dwarf, are standard candles with a small intrinsic dispersion around their average luminosity. Moreover, this dispersion can be further reduced to about 0.12 mag using an empirical relation between the peak magnitude and the width of the light curve [228]. This makes SNeIa excellent tools for observational cosmology. In particular, by measuring their apparent magnitude we can derive their distance from us and obtain the redshift–distance relation up to $z \sim 1$ which provides useful constraints on cosmological parameters [90]. This method has supplied the main contribution to the discovery of the present acceleration

of the Universe [229,220] and it is the basis of future proposals to probe the nature of dark energy through its equation of state (e.g. the SuperNova Acceleration Probe, [3]). On the other hand SNeIa, like all radiation sources, are affected by gravitational lensing effects which can magnify or demagnify their observed luminosity. This is a source of noise for studies which intend to measure the redshift–distance relation but this effect may also be used by itself to constrain cosmology in the same manner as gravitational lensing distortion of distant galaxies.

There are several important differences between SNeIa and galaxies as probes of gravitational lensing effects. Firstly, since SNeIa are point sources one uses the magnification (associated with the convergence κ) rather than the shear γ which we focussed on in previous Sections. In particular, the magnification μ can be written as:

$$\mu = \frac{1}{(1-\kappa)^2 - |\gamma|^2} \qquad \text{whence } \mu \simeq 1 + 2\kappa \quad \text{for } |\kappa| \ll 1, |\gamma| \ll 1. \tag{10.14}$$

Second, whereas weak gravitational lensing only modifies the observed ellipticities of galaxies at $z_s = 1$ by less than 10%, so that one needs many galaxies to extract the signal, the magnification of a type Ia supernova at $z_s = 1$ by gravitational lensing is of the same order as the intrinsic magnitude dispersion. Hence the signal-to-noise ratio is larger for SNeIa but since we have many more observed galaxies than SNeIa, accurate weak gravitational lensing effects have only been measured from galaxy ellipticities so far. Third, in order to derive the coherent shear on large scales one must cross-correlate the observed ellipticities of many distant galaxies over a window radius θ_s of the order of a few arcmin (since galaxies are not exactly spherical). This leads to observables such as the aperture-mass $M_{\rm ap}$ or the mean shear over scale θ_s which probe matter density fluctuations over scales of the order of $\mathcal{D}\theta_s$. On the contrary, the magnification of each SNeIa only probes the density fluctuations along its line-of-sight, which corresponds to no smoothing ($\theta_s = 0$). Then, by measuring the probability distribution of observed SNeIa magnitudes (or its variance) rather than cross-correlating different SNeIa, one can probe the statistics of the convergence κ with $\theta_s = 0$. This means that the signal is dominated by scales where $\ell^2 P_\kappa(\ell)$ is maximum, which are set by the matter power-spectrum. For CDM power-spectra this corresponds for sources at $z_s = 1$ to wavenumbers $k \sim 10$ h Mpc^{-1} whereas smoothing galaxy ellipticities over 1 arc min mainly probes smaller wavenumbers $k \sim 1$ h Mpc^{-1} [291]. Thus, weak lensing magnification of SNeIa allows us to probe density fluctuations on smaller scales than with galaxy ellipticities. This also implies that non-Gaussianities are more important for SNeIa gravitational lensing distortions. On the other hand, this difference between the scales probed by galaxy shear maps and SNeIa magnitude distortions means that both effects are only weakly correlated so that weak-lensing shear maps obtained from surrounding galaxies are not very efficient to correct the SNeIa luminosities [62].

The rms magnification of SNeIa was computed by analytical means in [77] who found that this would not significantly decrease the accuracy of the distance–redshift relation at $z_s < 0.5$ used to measure the current acceleration of the universe but it could have a significant effect at higher redshifts $z_s > 1$, in agreement with the numerical simulations performed in [307]. In particular, although future surveys covering more than a few square degrees will be unaffected, pencil beams surveys (< 1 deg^2) suffer significant contamination [57]. Turning to the use of SNeIa as a tool to detect gravitational lensing, [199] computed analytically the rms magnification of SNeIa to find that in a ΛCDM universe one needs at least 2400 SNeIa at $z_s = 0.5$ (or 110 SNeIa at $z_s = 1$) to detect weak lensing from their observed magnitudes. The PDF of the magnification $\mathcal{P}(\mu)$ was computed from a hierarchical model in [291] as well as its impact on the measure of cosmological parameters through the distance–redshift relation. In particular, this study shows the strong non-Gaussianity of the magnification with an extended high-μ tail which follows the high-density tail of the underlying matter density field, as can be seen from left panel of Fig. 27. Then, the high-luminosity tail of observed SNeIa could be used to detect weak lensing since it should be significantly enhanced by gravitational lensing. However, the number of observed SNeIa is still too small to draw definite conclusions about a possible detection of weak lensing effects by this method [310].

On the other hand, since the amplitude of the gravitational lensing contribution to the dispersion of observed SNeIa magnitudes depends on cosmological parameters it could be used to constrain cosmology [57]. Thus, [66] found that 2000 SNeIa in the redshift range $0.5 < z_s < 1.7$ should be able to constrain up to 5% the amplitude σ_8 of the matter power-spectrum. However, they point out that one needs to take into account the non-Gaussianity of the weak-lensing magnification distribution in order to obtain correct estimates, as seen in right panel of Fig. 27.

In order to eliminate the systematic errors associated with uncertainties on the intrinsic SNeIa luminosity distribution and its possible dependence on redshift, it is possible to cross-correlate SNeIa observed magnitudes with foreground galaxies, as advocated in [200]. Indeed, in the absence of gravitational lensing this cross-correlation would vanish. Using a halo model [200] found that a gravitational lensing signal should be detected with ~ 250 SNeIa at $z_s = 1$. This will be within the reach of future experiments (e.g. the SNAP satellite should observe thousands of SNeIa up to $z \sim 1.7$) but current surveys are too small to detect a correlation between SNeIa magnitudes and galaxy overdensities [197].

11. Summary and outlook

Ten years ago, the detection of weak lensing by large scale structures was only a dream. The progress accomplished, summarized in this review, are remarkable. The main reason for this progress in essentially the development of the Charge Coupled Device detectors which had a major impact on the accuracy of galaxy shape measurement. Adequate detectors are probably more important than larger telescopes; weak lensing needs a wide field of view and a well sampled Point Spread
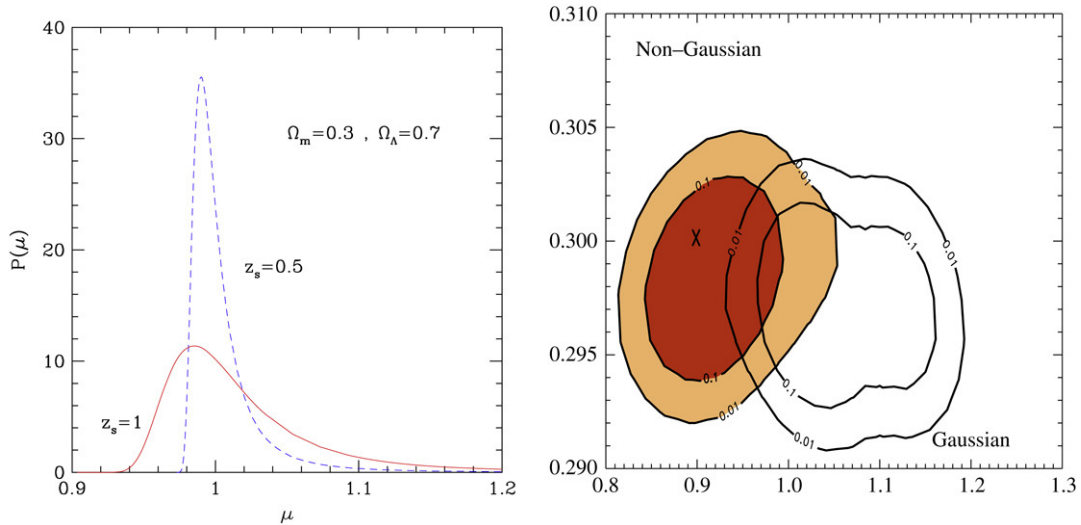
Fig. 27. *Left panel:* The probability distribution $\mathcal{P}(\mu)$ of the magnification within a ΛCDM universe for SNeIa at redshifts $z_s = 0.5$ or $z_s = 1$. From Valageas [291]. *Right panel:* The constraints on cosmological parameters obtained from the dispersion of SNeIa magnitudes from a SNAP-like survey. The two sets of contours correspond to analyzing the data assuming the true non-Gaussian distribution (shaded) or a Gaussian distribution (unshaded). From [66].

Function. One should remember for instance that the very first tentative attempts to measure distorted galaxy shapes [289] failed because of inadequate technology detectors.

In this review we mostly focussed on the statistical lensing, what one can learn on cosmology from the shear or convergence field, rather then focussing on individual lenses like clusters of galaxies. Like most of the cosmology probes, the information is mainly encoded in the power spectrum. We have shown how different cosmological parameters affect the projected mass (convergence or shear) and how it can be measured. In particular a combination of σ_8 and Ω_m appears well constrained from current lensing surveys. Statistical lensing can also be used to probe the biasing between dark matter and light, which provides clues on the assembly of galaxies inside their hosting halos. Future surveys should be able to provide accurate measurement of the biasing history as function of scale. A particularly interesting aspect of lensing is that it can probe the non-linear regime without any assumption on how light traces mass, and therefore go beyond the traditional power spectrum analysis. This property gives access to a different sensitivity to the cosmological parameters, an important feature to help breaking the parameter degeneracy between Ω_m and σ_8, but it also probes the history of the gravitational collapse. In that respect, high-order lensing statistics can be used to test the role of gravity during the collapse. The tomography technique, which has just started to be applied to lensing data, is very promising in probing the Dark Energy equation of state. The redshift slicing of the lensed sources, or 3D analysis of the shear field, are the only ways to measure the growth rate of structures (from the power spectrum and bi-spectrum) which is very sensitive to the dark energy content of the Universe. An interesting alternative to this is the 3-dimensional reconstruction of the mass distribution which in addition will give us the distribution of the dark matter in space. The combination of statistical lensing with other cosmology surveys in other wavelengths was also shown to be very important for three reasons (i) the sensitivity to the cosmological parameters is different and sometimes orthogonal (ii) the systematics can be drastically reduced (e.g. 21 cm observation which offers perfect source redshift measurement) (iii) this is the only way to probe the physics of the lenses beyond the simple mass-light relation.

It appears that ray-tracing techniques are an essential ingredient of any precision weak lensing study. In particular this would be the only way to address many of the complicated higher-order lensing effects such as multiplane deflections, source clustering, intrinsic and intrinsic-shear alignment which cannot be modeled with high precision. This is particularly relevant for future lensing surveys. Moreover, a proper assessment of the cosmic variance associated with the survey geometry can also be done from numerical simulation, which is also important for non-linear scales (typically less than half a degree) where prediction from semi-analytical models is challenging.

In 2006, weak lensing by large structures has just began to reach a status of scientific maturity: the first successes have demonstrated the feasibility of the technique and now begins an era of thorough weak lensing studies. The situation is similar to the Cosmic Microwave Background research in the pre-COBE era, before 1992: many independent groups have now measured the lensing fluctuation amplitude, and the next generation of lensing surveys will provide full sky, or nearly full sky, coverage. Table 5 summarizes the ongoing and future lensing surveys. The largest ongoing effort is the Canada France Hawaii Telescope Legacy Survey (CFHTLS). This survey represents a transition because this is the last one which requires a percent accuracy of galaxy shape measurement in order to be fully scientifically exploited. One percent accuracy is what we are currently capable of. All future surveys require a sub-percent precision level, which is still beyond our capability,

Table 5
List of forthcoming lensing surveys (adapted from [215])

Survey	Telescope	Sky coverage (deg^2)	Filters	Depth
Deep Lens Survey	CTIO	7×4	BVRz'	$R = 25$
CFHTLS-Wide	CFHT	170	ugriz	$i_{AB} = 24.5$
RCS2	CFHT	1000	grz	$i_{AB} = 22.5$
KIDS	VST	1500	ugriz	$i_{AB} = 22.9$
Pan-STARRS	PS1	30 000	grizy	$i_{AB} = 24$
KIDS-VIKING	VISTA	1500	JHK	$i_{AB} = 22.9$
Dark Energy Survey	CTIO	5000	griz	$i_{AB} = 24.5$
DarkCam	VISTA	10 000	ugriz	$i_{AB} = 24$
HyperCam	SUBARU	3500	TBD	TBD
SNAP	Space	300/2000	Narrow band (0.35–1.6)	TBD
LSST	6 m ground	20 000	Narrow band (0.35–1.2)	$i_{AB} = 27$
DUNE	Space	20 000	TBD	$i_{AB} = 25.5$

Surveys are sorted in three groups separated by a line. The top group show the current lensing surveys, the middle group shows survey starting in one year at the latest, and the group at the bottom is essentially not funded or partially funded projects.

as demonstrated by STEP. In fact, below the percent accuracy, many other effects will complicate the lensing measurement and analysis.

All recent studies show that the only way to quantify these effects, such as intrinsic alignment, shear-intrinsic alignment and source clustering, is to have a redshift estimate of each galaxy. This is only doable with photometric redshifts, which poses additional challenges: assuming one can get enough colors to obtain accurate photometric redshifts, there is no spectroscopic survey to help calibrating objects fainter than $I \sim 24$. The magnitude calibration of brighter sources could be problematic, especially from the ground due to zero-point fluctuations for different wavelengths. An absolute zero-point variation is not a problem, but an explicit dependence with color could jeopardize photometric redshift estimates. It appears that the only way to obtain unbiased photometric redshift is to have uniform magnitude calibration and to conduct a deep spectroscopic survey in order to validate the technique at faint magnitude/high redshift. Both might only be doable from space where photometry is stable. The tunable laser project [1] is an interesting solution for the zero-point issue, while the satellite GAIA [83], successor of Hipparcos, could help with absolute astrometry calibration. Interestingly, it seems that the shape measurement problem is likely to be solved in the next two or three years, thanks to the Shear TEsting Program.[11] The main limitation of weak lensing by large scale structures might therefore not be shape measurement anymore but multicolor photometric calibration, a very old astronomical problem!

Acknowledgements

Appendix. Analytical modeling of gravitational clustering and weak-lensing statistics

In order to derive the properties of weak lensing observables, like the shear γ, one first needs to specify the properties of the underlying density field. We briefly describe in this appendix two such models which can be used to predict weak lensing statistics, the hierarchical models presented for instance in [294] and the halo model described in detail in [52].

A.1. From density to weak-lensing many-body correlations

At lowest-order weak-lensing observables can be written as linear functionals of the density field, as seen in Eqs. (2.9)–(2.16). Therefore, their many-body connected correlation functions can be directly written in terms of the connected correlations ξ_p of the 3D matter density field defined by [217]:

$$\xi_p(\mathbf{x}_1, \ldots, \mathbf{x}_p; z) = \langle \delta(\mathbf{x}_1, z) \ldots \delta(\mathbf{x}_p, z) \rangle_c. \tag{A.1}$$

---

[11] http://www.physics.ubc.ca/heymans/step.html.

Note that for a Gaussian field we have $\xi_p = 0$ for $p \geq 3$. For a weak-lensing observable $\bar{X}$ defined as in Eq. (2.11) this gives in real space [291]:

$$\langle \bar{X}^p \rangle_c = \int_0^{\chi_s} \mathrm{d}\chi \, \hat{w}^p \int_{-\infty}^{\infty} \prod_{i=2}^{p} \mathrm{d}\chi'_i \int \prod_{i=1}^{p} \mathrm{d}\vec{\theta}_i \, U_X(\vec{\theta}_i) \, \xi_p \begin{pmatrix} 0 & \chi'_2 & \cdots & \chi'_p \\ \mathcal{D}\vec{\theta}_1 & \mathcal{D}\vec{\theta}_2 & \cdots & \mathcal{D}\vec{\theta}_p ; z \end{pmatrix}, \tag{A.2}$$

where z and $\mathcal{D}$ are the redshift and the angular diameter distance associated with the radial distance χ and $\chi'_i = \chi_i - \chi$ are the relative radial distances (using the fact that the 3D correlation ξ_p is invariant through translations and that cosmological length scales are much larger than the correlation length). This reads in Fourier space [294]:

$$\langle \bar{X}^p \rangle_c = (2\pi)^{-2p-1} \int \mathrm{d}\chi \, \hat{w}^p \int \prod_{j=1}^{p} \mathrm{d}\vec{k}_{\perp j} \, W_X(\vec{k}_{\perp j} \mathcal{D}\theta_s) \, \langle \delta(\vec{k}_{\perp 1}) \ldots \delta(\vec{k}_{\perp p}) \rangle_c. \tag{A.3}$$

In Eqs. (A.2) and (A.3) we used Limber's approximation $k \simeq k_\perp$ as for Eq. (3.4) and the longitudinal Dirac factor $\delta_D(k_{\parallel 1} + \cdots + k_{\parallel p})$ has been factorized out of the correlation $\langle \delta \cdots \delta \rangle_c$ in Eq. (A.3). Note that this approximation means that in real space the angular correlation functions at a redshift z along the line of sight are obtained by integrating the 3D correlation functions ξ_p over the radial coordinates as in Eq. (A.2).

Next, from the correlation functions one can obtain the full probability distribution function (PDF). Indeed, if we define the generating function $\varphi_X(y)$ of the cumulants $\langle \bar{X}^p \rangle_c$ as:

$$\varphi_X(y) = \sum_{p=2}^{\infty} \frac{(-1)^{p-1}}{p!} S_p^{(X)} y^p \quad \text{with} \quad S_p^{(X)} = \frac{\langle \bar{X}^p \rangle_c}{\langle \bar{X}^2 \rangle_c^{p-1}}, \tag{A.4}$$

where we used $\langle \bar{X} \rangle = 0$, then one can show that the PDF $\mathcal{P}_X(\bar{X})$ is given by the inverse Laplace transform:

$$\mathcal{P}_X(\bar{X}) = \int_{-i\infty}^{i\infty} \frac{\mathrm{d}y}{2\pi i \langle \bar{X}^2 \rangle_c} e^{[\bar{X}y - \varphi_X(y)]/\langle \bar{X}^2 \rangle_c}. \tag{A.5}$$

Thus, in order to compute $\mathcal{P}_X(\bar{X})$ one only needs to derive $\varphi_X(y)$, which may be written in terms of the density field from Eq. (A.2) or (A.3).

For the smoothed convergence $\bar{\kappa}$ the cumulants $\langle \bar{\kappa}^p \rangle_c$ correspond to averages of the density cumulants over cylindrical cells along the line of sight and they can be obtained with a good accuracy from the 3D density cumulants averaged over spherical cells. If we also use a mean-redshift approximation one obtains [291,292,12]:

$$\varphi_\kappa(y) \simeq |\kappa_{\min}|^2 \varphi_\delta \left(\frac{y}{|\kappa_{\min}|} \right) \quad \text{with} \quad \kappa_{\min} = -\int \mathrm{d}\chi \hat{w}, \tag{A.6}$$

where we introduced the minimum value $\kappa_{\min}$ of the convergence, which corresponds to an empty line of sight ($\delta = -1$, see Eq. (2.10)). This gives:

$$\mathcal{P}_\kappa(\bar{\kappa}) \simeq \frac{1}{|\kappa_{\min}|} \mathcal{P}_\delta \left(\delta \rightarrow \frac{\bar{\kappa}}{|\kappa_{\min}|}, \bar{\xi}_2 \rightarrow \frac{\langle \bar{\kappa}^2 \rangle}{|\kappa_{\min}|^2} \right), \tag{A.7}$$

where φ_δ and $\mathcal{P}_\delta$ are the generating function and the PDF of the 3D matter density contrast at the mean redshift and scale probed by the smoothed convergence $\bar{\kappa}$ (they depend on the angular radius θ_s and the galaxy distribution $n(z_s)$). Thus, within this simple approximation the PDF of the projected density field $\bar{\kappa}$ is directly expressed in terms of the PDF of the underlying 3D density contrast.

A.2. Hierarchical models

For more intricate observables like the shear or the aperture-mass which involve compensated filters one cannot perform approximations such as Eqs. (A.6) and (A.7) and it is not possible to approximate high-order cumulants or the PDF of weak-lensing observables in terms of those of the smoothed density contrast. Therefore, one needs to specify the detailed angular behavior of the many-body correlation functions $\xi_p(\mathbf{x}_1, \ldots, \mathbf{x}_p)$. A simple prescription is provided by the general class of "tree-models" defined by the hierarchical property [231,91]:

$$\xi_p(\mathbf{x}_1, \ldots, \mathbf{x}_p) = \sum_{(\alpha)} Q_p^{(\alpha)} \sum_{t_\alpha} \prod_{p-1} \xi_2(\mathbf{x}_i, \mathbf{x}_j), \tag{A.8}$$

where (α) is a particular tree-topology connecting the p points without making any loop, $Q_p^{(\alpha)}$ is a parameter associated with the order of the correlations and the topology involved, t_α is a particular labeling of the topology, (α), and the product is made over the $(p-1)$ links between the p points with two-body correlation functions. Then, as seen in [292] the 2D correlations ω_p involved in weak-lensing cumulants such as (A.2) exhibit the same tree-structure, with:

$$\omega_p(\vec{\theta}_1, \ldots, \vec{\theta}_p; z) = \int_{-\infty}^{\infty} \prod_{i=2}^{p} \mathrm{d}\chi_i \xi_p \begin{pmatrix} 0 & \cdots & \chi_p \\ \mathcal{D}\vec{\theta}_1 & \cdots & \mathcal{D}\vec{\theta}_p ; z \end{pmatrix}. \tag{A.9}$$

In order to perform numerical computations we need to specify the weights $Q_p^{(\alpha)}$. Thus, the "minimal tree-model" corresponds to the specific case where the weights $Q_p^{(\alpha)}$ are given by [20]:

$$Q_p^{(\alpha)} = \prod_{\text{vertices of } (\alpha)} \nu_q, \tag{A.10}$$

where ν_q is a constant weight associated to a vertex of the tree topology with q outgoing lines. The advantage of this minimal tree-model is that it is well-suited to the computation of the cumulant generating functions as defined in Eq. (A.4). Indeed, for an arbitrary real-space filter, $F(\mathbf{x})$, which defines the random variable s as:

$$s = \int d\mathbf{x} \, F(\mathbf{x})\delta(\mathbf{x}) \quad \text{and} \quad \xi_s = \langle s^2 \rangle, \tag{A.11}$$

it is possible to obtain a simple implicit expression for the generating function, $\varphi_s(y)$, see [20,143]:

$$\varphi_s(y) = y \int d\mathbf{x} \, F(\mathbf{x}) \left[\zeta_\nu[\tau(\mathbf{x})] - \frac{\tau(\mathbf{x})\zeta_\nu'[\tau(\mathbf{x})]}{2} \right] \tag{A.12}$$

$$\tau(\mathbf{x}) = -y \int d\mathbf{x}' \, F(\mathbf{x}') \frac{\xi_2(\mathbf{x}, \mathbf{x}')}{\xi_s} \zeta_\nu'[\tau(\mathbf{x}')], \tag{A.13}$$

where the function $\zeta_\nu(\tau)$ is defined as the generating function for the coefficients ν_p:

$$\zeta_\nu(\tau) = \sum_{p=1}^{\infty} \frac{(-1)^p}{p!} \nu_p \tau^p \quad \text{with } \nu_1 = 1. \tag{A.14}$$

Since the 2D correlations ω_p obey the same minimal tree-model we can perform the resummation (A.12) and (A.13) which yields [24,12]:

$$\varphi_X(y) = \int_0^{\chi_s} d\chi \, \frac{\langle \bar{X}^2 \rangle_c}{\overline{\omega}_{2X}} \varphi_{\text{cyl.}} \left(y\hat{w} \frac{\overline{\omega}_{2X}}{\langle \bar{X}^2 \rangle_c}; z \right), \tag{A.15}$$

where we introduced the 2D generating function $\varphi_{\text{cyl.}}$ associated with the 2D correlations ω_p, given by the resummation:

$$\varphi_{\text{cyl.}}(y) = y \int d\vec{\theta} \, U_X(\vec{\theta}) \left[\zeta_\nu[\tau(\vec{\theta})] - \frac{\tau(\vec{\theta})\zeta_\nu'[\tau(\vec{\theta})]}{2} \right] \tag{A.16}$$

$$\tau(\vec{\theta}) = -y \int d\vec{\theta}' \, U_X(\vec{\theta}') \frac{\omega_2(\vec{\theta}, \vec{\theta}'; z)}{\overline{\omega}_{2X}(z)} \zeta_\nu'[\tau(\vec{\theta}')]. \tag{A.17}$$

Here we introduced the angular average $\overline{\omega}_{2X}$ of the 2D correlation ω_2, associated with the filter U_X:

$$\overline{\omega}_{2X}(z) = \int d\vec{\theta}_1 \, d\vec{\theta}_2 U_X(\vec{\theta}_1)U_X(\vec{\theta}_2)\omega_2(\vec{\theta}_1, \vec{\theta}_2; z). \tag{A.18}$$

Thus, one obtains in this way the generating function $\varphi_X(y)$ which yields in turn the PDF $\mathcal{P}_X(\bar{X})$ from Eq. (A.5).

A second simple model is the "stellar model" introduced in [294] where we only keep the stellar diagrams in Eq. (A.8). Thus, the p-point connected correlation ξ_p of the density field can now be written as:

$$\xi_p(\mathbf{x}_1, \ldots, \mathbf{x}_p) = \frac{\tilde{S}_p}{p} \sum_{i=1}^{p} \prod_{j \neq i} \xi_2(\mathbf{x}_i, \mathbf{x}_j). \tag{A.19}$$

The advantage of the stellar-model (A.19) is that it leads to very simple calculations in Fourier space. Indeed, Eq. (A.19) reads in Fourier space:

$$\langle \delta(\mathbf{k}_1) \ldots \delta(\mathbf{k}_p) \rangle_c = \frac{\tilde{S}_p}{p} (2\pi)^3 \delta_D(\mathbf{k}_1 + \cdots + \mathbf{k}_p) \sum_{i=1}^{p} \prod_{j \neq i} P(k_j). \tag{A.20}$$

Using the standard exponential representation of the Dirac distribution gives [294]:

$$\langle \bar{X}^p \rangle_c = \tilde{S}_p \int_0^{\chi_s} d\chi \, \hat{w}^p \int d\vec{\theta} \, U_X(\vec{\theta})I_X(\chi, \vec{\theta})^{p-1}, \tag{A.21}$$

where we introduced:

$$I_X(\chi, \vec{\theta}) = \int \frac{d\vec{k}_\perp}{(2\pi)^2} e^{-i\vec{k}_\perp \cdot \mathcal{D}\vec{\theta}} W_X(\vec{k}_\perp \mathcal{D}\theta_s)P(k_\perp; z). \tag{A.22}$$

Then, using Eq. (A.4) we obtain:

$$\varphi_X(y) = \int_0^{\chi_s} d\chi \int d\vec{\theta} \, U_X(\vec{\theta}) \frac{\langle \bar{X}^2 \rangle_c}{I_X(\chi, \vec{\theta})} \varphi_\delta \left(y\hat{w} \frac{I_X}{\langle \bar{X}^2 \rangle_c}; z \right), \tag{A.23}$$

which directly gives $\varphi_X(y)$ in terms of the cumulant generating function of the 3D density field φ_δ.

A.3. Halo models

An alternative to the hierarchical models presented in Appendix A.2 is provided by the halo model where the matter density field is described as a collection of halos [181,232,264]. Then, the density correlation functions are obtained through a convolution over the halo density profiles. One also needs to specify the many-body correlations of the halos themselves as well as their multiplicity function. Thus, the density field is written as the superposition of the halo profiles:

$$\rho(\mathbf{x}) = \sum_i m_i u_{m_i}(\mathbf{x} - \mathbf{x}_i) \quad \text{with} \int d\mathbf{x}\, u_m(\mathbf{x}) = 1, \tag{A.24}$$

where we introduced the normalized density profile $u_m(x)$ of halos of mass m. Then, the density two-point correlation function is expressed as the sum of correlations within a single halo (1-halo term, both points are within the same halo) and between different halos (2-halo term, the two points are within two different halos):

$$\xi_2(\mathbf{x}_1, \mathbf{x}_2) = \int dm\, n(m) \left(\frac{m}{\bar{\rho}}\right)^2 \int d\mathbf{x}'\, u_m(\mathbf{x}_1 - \mathbf{x}') u_m(\mathbf{x}_2 - \mathbf{x}') + \int dm_1\, n(m_1) \frac{m_1}{\bar{\rho}}$$
$$\times \int dm_2\, n(m_2) \frac{m_2}{\bar{\rho}} \int d\mathbf{x}'_1\, u_{m_1}(\mathbf{x}_1 - \mathbf{x}'_1) \int d\mathbf{x}'_2\, u_{m_2}(\mathbf{x}_2 - \mathbf{x}'_2) \xi_h(\mathbf{x}'_1, \mathbf{x}'_2; m_1, m_2), \tag{A.25}$$

where $n(m)$ is the halo mass function and ξ_h is the halo two-point correlation [278,279]. In a similar fashion one can write the n-point density correlation as a sum of 1-halo up to n-halo terms. In practice, it is more convenient to work in Fourier space (to simplify the convolution products and to take advantage of the statistical homogeneity and isotropy of the system). Thus, the density power-spectrum reads [261,179,251]:

$$P(k) = I_2^0(k, k) + \left[I_1^1(k)\right]^2 P_L(k) \tag{A.26}$$

with:

$$I_\mu^\beta(k_1, \ldots, k_\mu) = \int dm\, n(m) b(m)^\beta \left(\frac{m}{\bar{\rho}}\right)^\mu u_m(k_1) \ldots u_m(k_\mu), \tag{A.27}$$

where $u_m(k)$ is the Fourier transform of the halo density profile. In Eq. (A.26) we assumed that the halo–halo power-spectrum can be written as $P_h(k; m_1, m_2) = b(m_1)b(m_2)P_L(k)$ where P_L is the linear matter power-spectrum and $b(m)$ is the bias parameter which describes how the halo distribution is biased with respect to the dark matter density field. Indeed, the 2-halo term dominates at large scales which are described by the quasi-linear theory (hence it is sufficient to use P_L) whereas the 1-halo term dominates at small non-linear scales. This also ensures that one recovers the results of standard linear theory at large scales. To complete the halo model one needs to specify the halo density profile, which is often taken from [212], the halo mass function, taken for instance from [265,221], and the biasing of the halo distribution as from [205]. Then, the correlation functions of weak-lensing observables can be derived from Eqs. (A.2) and (A.3). For instance, the 1-halo contribution to the angular two-point correlation of the convergence field reads [278]:

$$\langle \kappa(\vec{\theta}_1)\kappa(\vec{\theta}_2)\rangle_{1h} = \int d\chi \frac{\hat{w}^2}{\mathcal{D}^2} \int dm\, n(m) \left(\frac{m}{\bar{\rho}}\right)^2 \int dl \frac{l}{2\pi} |u_m(k)|^2 J_0(l\theta), \tag{A.28}$$

where $k = l/\mathcal{D}(\chi)$. Similar expressions give the 1-halo contribution to higher-order convergence correlation functions whereas 2-halo terms involve the linear density power-spectrum, 3-halo terms involve the density bispectrum and so on. This approach has been used to estimate the low-order correlations of weak-lensing observables up to fourth-order (the kurtosis of the shear, see [277]) but no attempt has been made to predict the full PDF $\mathcal{P}_X(\bar{X})$ yet (however see [283] for a model for the tails of the matter density PDF).

References

[1] J. Albert, W. Burgett, J. Rhodes, astro-ph/0604339.
[2] A. Albrecht, et al. Dark Energy Task Force Report, 2006. astro-ph/0609591.
[3] G. Aldering, New Astron. Rev. 49 (2005) 346.
[4] L. Amendola, M. Kunz, D. Sapone, astroph/0704.2421.
[5] A. Babul, M.H. Lee, Mon. Not. R. Astron. Soc. 250 (1991) 407.
[6] D.J. Bacon, A. Refregier, R. Ellis, Mon. Not. R. Astron. Soc. 318 (2000) 625.
[7] D.J. Bacon, R. Massey, A. Refregier, R. Ellis, Mon. Not. R. Astron. Soc. 344 (2003) 673.
[8] D.J. Bacon, D.M. Goldberg, B.T.P. Rowe, A.N. Taylor, Mon. Not. R. Astron. Soc. 365 (2006) 414.
[9] A.J. Barber, P.A. Thomas, H.M.P. Couchman, Mon. Not. R. Astron. Soc. 310 (1999) 453.
[10] A.J. Barber, P.A. Thomas, H.M.P. Couchman, C.J. Fluke, Mon. Not. R. Astron. Soc. 319 (2000) 267.
[11] A.J. Barber, Mon. Not. R. Astron. Soc. 335 (2002) 909.
[12] A.J. Barber, D. Munshi, P. Valageas, Mon. Not. R. Astron. Soc. 347 (2004) 667.
[13] M. Bartelmann, Astron. Astrophys. 313 (1996) 697.
[14] M. Bartelmann, P. Schneider, Astron. Astrophys. 345 (1999) 17.
[15] M. Bartelmann, Astron. Astrophys. 370 (2001) 754.
[16] M. Bartelmann, P. Schneider, Phys. Rep. 340 (2001) 291.

[17] M. Bartelmann, M. Doran, C. Wetterich, Astron. Astrophys. 454 (2006) 27.
[18] K. Benabed, F. Bernardeau, L. Van Waerbeke, Phys. Rev. D 63 (2001) 043501.
[19] J. Benjamin, et al., Mon. Not. R. Astron. Soc. 381 (2007) 702.
[20] F. Bernardeau, R. Schaeffer, Astron. Astrophys. 255 (1992) 1.
[21] F. Bernardeau, L. Van Waerbeke, Y. Mellier, Astron. Astrophys. 322 (1997) 1.
[22] F. Bernardeau, Astron. Astrophys. 324 (1997) 15. astro-ph/9611012.
[23] F. Bernardeau, Astron. Astrophys. 338 (1998) 375.
[24] F. Bernardeau, P. Valageas, Astron. Astrophys. 364 (2000) 1.
[25] F. Bernardeau, Y. Mellier, L. Van Waerbeke, Astron. Astrophys. 389 (2002) L28.
[26] F. Bernardeau, L. Van Waerbeke, Y. Mellier, Astron. Astrophys. 397 (2003) 405.
[27] F. Bernardeau, Phys. Rev. Lett. (2005) (submitted for publication). astro-ph/0409224.
[28] G. Bernstein, M. Jarvis, Astron. J. 123 (2002) 583.
[29] G. Bernstein, B. Jain, Astrophys. J. 600 (2004) 17.
[30] A. Blanchard, J. Schneider, Astron. Astrophys. 184 (1987) 1.
[31] R.D. Blandford, A.B. Saust, T.G. Brainerd, J.V. Villumsen, Mon. Not. R. Astron. Soc. 251 (1991) 600.
[32] Blake et al., New Astron. Rev. 48 (2004) 1063–1077.
[33] H. Bonnet, Y. Mellier, Astron. Astrophys. 303 (1995) 331.
[34] M. Bradac, D. Clowe, A. Gonzales, et al., Astrophys. J. 652 (2006) 937.
[35] T.G. Brainerd, R.D. Blandford, I. Smail, Astrophys. J. 466 (1996) 623.
[36] S.L. Bridle, M.P. Hobson, A.N. Lasenby, R. Saunders, Mon. Not. R. Astron. Soc. 299 (1998) 895.
[37] S.L. Bridle, L. King, New J. Phys. 9 (2007) 444.
[38] M. Brown, A.N. Taylor, N.C. Hambly, S. Dye, Mon. Not. R. Astron. Soc. 333 (2002) 501.
[39] M. Brown, A.N. Taylor, D.J. Bacon, M.E. Gray, S. Dye, K. Meisenheimer, C. Wolf, Mon. Not. R. Astron. Soc. 341 (2003) 100.
[40] E.D. Carlson, M.E. Machacek, L.J. Hall, Astrophys. J. 398 (1992) 43.
[41] P.G. Castro, A.F. Heavens, T.D. Kitching, Phys. Rev. D 72 (2005) 3516.
[42] P. Catelan, M. Kamionkowski, R. Blandford, Mon. Not. R. Astron. Soc. 320 (2001) L7.
[43] A. Challinor, M. Ford, A. Lasenby, Mon. Not. R. Astron. Soc. 312 (2000) 159. astro-ph/9905227.
[44] A. Challinor, 2004. astro-ph/0403344.
[45] A. Challinor, A. Lewis, Phys. Rev. D 71 (2005) 103010. astro-ph/0502425.
[46] M. Chevallier, D. Polarski, Internat. J. Modern Phy. D 10 (2001) 213.
[47] D. Clowe, M. Bradac, A. Gonzales, et al., Astrophys. J. 648 (2006) L109.
[48] D. Clowe, et al., Astron. Astrophys. 451 (2006) 395.
[49] S. Cole, G. Efstathiou, Mon. Not. R. Astron. Soc. 239 (1989) 195.
[50] C. Contaldi, H. Hoekstra, A. Lewis, Phys. Rev. Lett. 90 (2003) 1303.
[51] A. Cooray, W. Hu, Astrophys. J. 574 (2002) 19. astro-ph/0202411.
[52] A. Cooray, R. Sheth, Phys. Rep. 372 (2002) 1.
[53] A.R. Cooray, Astrophys. J. 596 (2003) L127. astro-ph/0305515.
[54] A. Cooray, M. Kesden, New Astron. 8 (2003) 231.
[55] A.R. Cooray, New Astron. 9 (2004) 173. astro-ph/0309301.
[56] A. Cooray, D. Baumann, K. Sigurdson, 2004. astro-ph/0410006.
[57] A. Cooray, D. Huterer, D.E. Holz, Phys. Rev. Lett. 96 (2006) 1301.
[58] H.M.P. Couchman, A.J. Barber, P.A. Thomas, Mon. Not. R. Astron. Soc. 308 (1999) 180.
[59] R. Crittenden, et al., Astrophys. J. 559 (2000) 552.
[60] R. Crittenden, P. Natarajan, U.-L. Pen, T. Theuns, Astrophys. J. 568 (2002) 20.
[61] R. Croft, C. Metzler, Astrophys. J. 541 (2000) 561.
[62] N. Dalal, D.E. Holz, X. Chen, J.A. Frieman, Astrophys. J. 585 (2003) L11.
[63] J.P. Dietrich, T. Erben, G. Lamer, P. Schneider, A. Schwope, J. Hartlap, M. Maturi, 2007. astroph/0705/3455.
[64] S. Dodelson, Modern Cosmology, Academic Press, ISBN: 0122191412, 2003.
[65] S. Dodelson, G.D. Starkman, 2003. astro-ph/0305467.
[66] S. Dodelson, A. Vallinotto, Phys. Rev. D 74 (2006) 3515.
[67] D. Dolney, B. Jain, M. Takada, Mon. Not. R. Astron. Soc. 352 (2004) 1019.
[68] O. Dore, F. Bouchet, Y. Mellier, R. Teyssier, Astron. Astrophys. 375 (2001) 14.
[69] J. Dubinski, R. Carlberg, Astrophys. J. 378 (1991) 496.
[70] G. Dvali, G. Gabadadze, M. Porrati, Phys. Lett. B 485 (2000) 208.
[71] F.W. Dyson, A.S. Eddington, C. Davidson, Philos. Trans. R. Soc. A 220 (1920) 291.
[72] A. Einstein, Sitzungber. Preuss. Akad. Wiss. (1915) 831.
[73] T. Erben, et al., Astron. Astrophys. 366 (2001) 717.
[74] G. Fahlman, N. Kaiser, G. Squires, D. Woods, Astrophys. J. 437 (1994) 56.
[75] J.E. Forero-Romero, J. Blaizot, J. Devriendt, et al. astro-ph/0611932.
[76] B. Fort, Y. Mellier, Astron. Astrophys. Rev. 5 (1994) 239.
[77] J. Frieman, Comments on Astrophysics (1997). astro-ph/9608068.
[78] L. Fu, E. Semboloni, H. Hoekstra, et al., 2007. arXiv:0712.0884.
[79] S.R. Furlanetto, A. Sokasian, L. Hernquist, Mon. Not. R. Astron. Soc. 347 (2004) 187.
[80] R. Gavazzi, G.. Soucail, astro-ph/0605591.
[81] B. Geiger, P. Schneider, Mon. Not. R. Astron. Soc. 302 (1999) 118.
[82] M. Gibilisco, Astrophys. Space Sci. 249 (1997) 189. astro-ph/9701203.
[83] G. Gilmore, et al. astro-ph/9805180.
[84] F. Giovi, C. Baccigalupi, F. Perrotta, Phys. Rev. D 68 (2003) 123002. astro-ph/0308118.
[85] F. Giovi, C. Baccigalupi, F. Perrotta, Phys. Rev. D 71 (2005) 103009. astro-ph/0411702.
[86] B. Gold, Phys. Rev. D 71 (2005) 063522. astro-ph/0411376.
[87] D.M. Goldberg, D.N. Spergel, Phys. Rev. D 59 (1999) 103002. astro-ph/9811251.
[88] D. Goldberg, P. Natarajan, Astrophys. J. 564 (2002) 65.
[89] D. Goldberg, D. Bacon, Astrophys. J. 619 (2005) 741.
[90] A. Goobar, S. Perlmutter, Astrophys. J. 450 (1995) 14.
[91] E. Groth, P.J.E. Peebles, Astrophys. J. 217 (1977) 385.
[92] J. Guzik, U. Seljak, M. Zaldarriaga, Phys. Rev. D 62 (2000) 043517.
[93] J. Guzik, U. Seljak, Mon. Not. R. Astron. Soc. 335 (2002) 311.
[94] T. Hamana, H. Martel, T. Futamase, Astrophys. J. 529 (2000) 56.
[95] T. Hamana, S.T. Colombi, A. Thion, J.E. Devriendt, Y. Mellier, F. Bernardeau, Mon. Not. R. Astron. Soc. 330 (2002) 365.
[96] T. Hamana, S. Miyazaki, K. Shimasaku, H. Furusawa, M. Doi, et al., Astrophys. J. 597 (2003) 98.
[97] H. Hämmerle, J.M. Miralles, P. Schneider, T. Erben, R.A. Fosbury, Astron. Astrophys. 385 (2002) 743.

[98] A.F. Heavens, A. Refregier, C.E.C. Heymans, Mon. Not. R. Astron. Soc. 319 (2000) 649.
[99] A.F. Heavens, Mon. Not. R. Astron. Soc. 343 (2003) 1327.
[100] A.F. Heavens, T.D. Kitching, A.N. Taylor, Mon. Not. R. Astron. Soc. 373 (2006) 105. astro-ph/0606568.
[101] A.F. Heavens, T.D. Kitching, L. Verde, Mon. Not. R. Astron. Soc. 380 (2007) 1029.
[102] M. Hetterscheidt, et al., Astron. Astrophys. 442 (2005) 43.
[103] C.E.C. Heymans, A.F. Heavens, Mon. Not. R. Astron. Soc. 339 (2003) 711.
[104] C.E.C. Heymans, M.L. Brown, A.F. Heavens, K. Meisenheimer, A.N. Taylor, C. Wolf, Mon. Not. R. Astron. Soc. 347 (2004) 895.
[105] C.E.C. Heymans, et al., Mon. Not. R. Astron. Soc. 368 (2006) 1323.
[106] C.E.C. Heymans, M. White, A.F. Heavens, C. Vale, L. Van Waerbeke, Mon. Not. R. Astron. Soc. 371 (2006) 750.
[107] C.E.C. Heymans, et al., Mon. Not. R. Astron. Soc. 371 (2006) L60.
[108] A.K. Hicks, E. Ellingson, H. Hoekstra, H.K.C. Yee, Astrophys. J. 652 (2006) 232.
[109] C. Hirata, U. Seljak, Mon. Not. R. Astron. Soc. 343 (2003) 459.
[110] C. Hirata, U. Seljak, Phys. Rev. D 67 (2003) 043001.
[111] C. Hirata, U. Seljak, Phys. Rev. D 204 (2004) 3056.
[112] H. Hoekstra, et al., Astrophys. J. 504 (1998) 636.
[113] H. Hoekstra, Astron. Astrophys. 370 (2001) 743.
[114] H. Hoekstra, H.K.C. Yee, M. Gladders, L. Felipe Barrientos, P.B. Hall, L. Infante, Astrophys. J. 572 (2002) 55.
[115] H. Hoekstra, H.K.C. Yee, M. Gladders, Astrophys. J. 577 (2002) 595.
[116] H. Hoekstra, L. Van Waerbeke, M. Gladders, Y. Mellier, H. Yee, Astrophys. J. 577 (2002) 604.
[117] H. Hoekstra, Mon. Not. R. Astron. Soc. 347 (2004) 1337.
[118] H. Hoekstra, H.K.C. Yee, M. Gladders, Astrophys. J. 606 (2004) 67.
[119] H. Hoekstra, B.C. Hsieh, H.K.C. Yee, H. Lin, M.D. Gladders, Astrophys. J. 635 (2005) 73.
[120] H. Hoekstra, et al., Astrophys. J. 647 (2006) 116.
[121] W. Hu, Astrophys. J. 522 (1999) 21.
[122] W. Hu, Phys. Rev. D 62 (2000) 3007.
[123] W. Hu, Phys. Rev. D 64 (2001) 083005. astro-ph/0105117.
[124] W. Hu, M. White, Astrophys. J. 554 (2001) 67.
[125] W. Hu, Phys. Rev. D 65 (2002) 023003. astro-ph/0108090.
[126] W. Hu, T. Okamoto, Astrophys. J. 574 (2002) 566.
[127] W. Hu, S. Dodelson, Astron. Astrophys. 40 (2002) 171. astro-ph/0110414.
[128] W. Hu, Ann. Phys. 303 (2003) 203. astro-ph/0210696.
[129] W. Hu, C. Keeton, Phys. Rev. D 66 (2003) 3506.
[130] W. Hu, M. White, Sci. Am. 290 (2004) 44. http://background.uchicago.edu/whu/Papers/HuWhi04.pdf.
[131] M. Hudson, S. Gwyn, H. Dahle, N. Kaiser, Astrophys. J. 503 (1998) 531.
[132] D. Huterer, E. Linder, 2006 astro-ph/0608681.
[133] D. Huterer, M. Takada, G. Bernstein, B. Jain, Mon. Not. R. Astron. Soc. 366 (2006) 10.
[134] O. Ilbert, et al., Astron. Astrophys. 457 (2006) 841.
[135] I.T. Iliev, P.R. Shapiro, A. Ferrara, H. Martel, Astrophys. J. Lett. 572 (2002) L123.
[136] I.T. Iliev, E. Scannapieco, H. Martel, P.R. Shapiro, Mon. Not. R. Astron. Soc. 341 (2003) 81.
[137] B. Jain, U. Seljak, Astrophys. J. 484 (1997) 560.
[138] B. Jain, U. Seljak, S.D.M. White, Astrophys. J. 530 (2000) 547.
[139] B. Jain, L. Van Waerbeke, Astrophys. J. 530 (2000) L1.
[140] B. Jain, A.N. Taylor, Phys. Rev. Lett. 91 (2003) 1302.
[141] B. Jain, M. Jarvis, G. Berstein, JCAP 02 (2006) 001.
[142] B. Jain, P. Zhang, 2007 astroph-0709.2375.
[143] G. Jannink, J. Des Cloiseaux, Les polymères en solution, Les editions de physique, Les Ulis, France, 1987.
[144] M. Jarosszyńsky, C. Park, B. Paczńisky, J.R. Gott, Astrophys. J. 365 (1990) 22.
[145] M. Jarvis, G.M. Bernstein, P. Fisher, D. Smith, B. Jain, J.A. Tyson, D. Wittman, Astrophys. J. 125 (2002) 1014.
[146] M. Jarvis, G. Bernstein, B. Jain, Astrophys. J. 338 (2004).
[147] Y.P. Jing, Mon. Not. R. Astron. Soc. 335 (2002) L89.
[148] N. Kaiser, Astrophys. J. 388 (1992) 272.
[149] N. Kaiser, G. Squires, Astrophys. J. 404 (1993) 441.
[150] N. Kaiser, G. Squires, G. Fahlman, D. Woods, T. Broadhurst, Wide field spectroscopy and the distant universe, in: Proceedings of the 35th Herstmonceux
      Conference, July 4–8, 1994.
[151] N. Kaiser, Astrophys. J. 439 (1995) L1.
[152] N. Kaiser, G. Squires, T. Broadhurst, Astrophys. J. 449 (1995) 460.
[153] N. Kaiser, G. Squires, Astrophys. J. 473 (1996) 65.
[154] N. Kaiser, Astrophys. J. 498 (1998) 26.
[155] N. Kaiser, Astrophys. J. 537 (2000) 555.
[156] N. Kaiser, G. Wilson, G.A. Luppino, 2000 astro-ph/0003338.
[157] M. Kamionkowski, A. Kosowsky, A. Stebbins, Phys. Rev. D 55 (1997) 7368. astro-ph/9611125.
[158] N.E. Kassim, T.J.W. Lazio, W.C. Erickson, P.C. Crane, R.A. Perley, B. Hicks, in: Harvey R. Butcher, (Ed.) Proc. SPIE, Radio Telescopes, vol. 4015, 2000,
      p. 328–340.
[159] M.H. Kesden, A. Cooray, M. Kamionkowski, Phys. Rev. D 66 (2002) 083007. astro-ph/0208325.
[160] M. Kilbinger, P. Schneider, Astron. Astrophys. 442 (2005) 69.
[161] L. King, P. Schneider, Astron. Astrophys. 396 (2002) 411.
[162] L. King, Astron. Astrophys. 441 (2005) 47.
[163] T.D. Kitching, A.F. Heavens, A.N. Taylor, M.L. Brown, K. Meisenheimer, C. Wolf, M.E. Gray, D.J. Bacon, 2006 astro-ph/0610284.
[164] T.D. Kitching, L. Miller, C.E. Heymans, L. van Waerbeke, A.F. Heavens, 2008 astro-ph/0802.1528.
[165] M. Kleinheinrich, et al., Astron. Astrophys. 455 (2006) 441.
[166] K. Kuijken, Astron. Astrophys. 352 (1999) 355.
[167] K. Kuijken, Astron. Astrophys. 456 (2006) 827.
[168] M. Kunz, D. Sapone, Phys. Rev. Lett. 98 (2006) 121301.
[169] M.H. Lee, B. Paczńisky, Astrophys. J. 357 (1990) 32.
[170] J. Lesgourgues, et al., Phys. Rev. D 73 (2006) 045021. astro-ph/0511735.
[171] A. Lewis, L. King, 2005. astro-ph/0512104.
[172] A. Lewis, A. Challinor, Phys. Rep. 429 (2006) 1.
[173] A. Liddle, D. Lyth, Cosmological Inflation and Large-Scale Structure, Cambridge University Press, 2000.
[174] D.N. Limber, Astrophys. J. 119 (1954) 655.
[175] A. Linde, V. Mukhanov, M. Sasaki, JCAP 0510 (2005) 002. astro-ph/0509015.
[176] E.V. Linder, Mon. Not. R. Astron. Soc. 243 (1990) 353.

[177] E.V. Linder, R.N. Cahn, Astropart. Phys. 28 (2007) 481.
[178] G. Luppino, N. Kaiser, Astrophys. J. 475 (1997) 20.
[179] C.-P. Ma, J.N. Fry, Astrophys. J. 543 (2000) 503.
[180] Z. Ma, W. Hu, D. Huterer, Astrophys. J. 636 (2006) 21.
[181] J. McClelland, J. Silk, Astrophys. J. 217 (1977) 331.
[182] P. Madau, A. Meiksin, M.J. Rees, Astrophys. J. 475 (1997) 429.
[183] K.S. Mandel, M. Zaldarriaga, 2005. astro-ph/0512218.
[184] R. Mandelbaum, et al., Mon. Not. R. Astron. Soc. 361 (2005) 1287.
[185] R. Mandelbaum, et al., Mon. Not. R. Astron. Soc. 370 (2006) 1008.
[186] R. Mandelbaum, et al., Mon. Not. R. Astron. Soc. 372 (2006) 758.
[187] R. Maoli, L. van Waerbeke, Y. Mellier, P. Schneider, B. Jain, et al., Astron. Astrophys. 368 (2001) 766.
[188] L. Marian, G. Bernstein, Phys. Rev. D 73 (2006) l3525.
[189] P.J. Marshall, M.P. Hobson, S.F. Gull, S.L. Bridle, Mon. Not. R. Astron. Soc. 335 (2002) 1037.
[190] R. Massey, A. Refregier, D.J. Bacon, R.S. Ellis, M.L. Brown, Mon. Not. R. Astron. Soc. 359 (2005) 1277.
[191] R. Massey, A. Refregier, Mon. Not. R. Astron. Soc. 363 (2005) 197.
[192] R. Massey, et al., Nature 445 (2007) 286.
[193] R. Massey, et al., Mon. Not. R. Astron. Soc. 376 (2007) 13. astro-ph/0608643.
[194] R. Massey, B. Rowe, A. Refregier, D.J. Bacon, J. Berge, 2006. astro-ph/0609795.
[195] Y. Mellier, Ann. Rev. Astron. Astrophys. 37 (1999) 127.
[196] Y. Mellier, G. Meylan (Eds.), Impact of Gravitational Lensing on Cosmology, IAU S225, Cambridge University Press, 2004.
[197] B. Ménard, N. Dalal, Mon. Not. R. Astron. Soc. 358 (2005) 101.
[198] R.B. Metcalf, J. Silk, Astrophys. J. 489 (1997) 1. astro-ph/9708059.
[199] B Metcalf, Mon. Not. R. Astron. Soc. 305 (1999) 746.
[200] B. Metcalf, Mon. Not. R. Astron. Soc. 327 (2001) 115.
[201] L. Miller, T. Kitching, C. Heymans, A. Heavens, L. van Waerbeke, Mon. Not. R. Astron. Soc. 382 (2007) 185.
[202] M. Milgrom, Astrophys. J. 270 (1983) 365.
[203] J. Miralda-Escude, Astrophys. J. 380 (1991) 1.
[204] S. Miyazaki, et al., Astrophys. J. 580 (2002) L97.
[205] H.J. Mo, S.D.M. White, Mon. Not. R. Astron. Soc. 282 (1996) 347.
[206] V. Mukhanov, H. Feldman, R. Brandenberger, Phys. Rep. 215 (1992) 203.
[207] D. Munshi, P. Valageas, A.J. Barber, Mon. Not. R. Astron. Soc. 350 (2004) 77.
[208] D. Munshi, P. Valageas, Mon. Not. R. Astron. Soc. 356 (2005) 439.
[209] D. Munshi, P. Valageas, Mon. Not. R. Astron. Soc. 360 (2005) 1401.
[210] R. Narayan, R.D. Blandford, Ann. New York Acad. Sci. 647 (1991).
[211] P. Natarajan, J.P. Kneib, Mon. Not. R. Astron. Soc. 287 (1997) 833.
[212] J.F. Navarro, C.S. Frenk, S.D.M. White, Astrophys. J. 490 (1997) 493.
[213] S.P. Oh, K.J. Mack, Mon. Not. R. Astron. Soc. 346 (2003) 871.
[214] J.A. Peacock, S.J. Dodds, Mon. Not. R. Astron. Soc. 280 (1996) L19.
[215] J.A. Peacock, et al. 2006. astro-ph/0610906.
[216] P.J.E. Peebles, J.T. Yu, Astrophys. J. 162 (1970) 815.
[217] P.J.E. Peebles, The Large-Scale Structure of the Universe, Princeton University Press, Princeton, 1980.
[218] U.-L. Pen, T. Zhang, L. Van Waerbeke, Y. Mellier, P. Zhang, J. Dubinski, Astrophys. J. 592 (2003) 664.
[219] U.-L. Pen, New Astron. 9 (2004) 417.
[220] S. Perlmutter, et al., Astrophys. J. 517 (1999) 565.
[221] W. Press, P. Schechter, Astrophys. J. 187 (1974) 425.
[222] E. Puchwein, M. Bartelmann, Astron. Astrophys. 455 (2006) 791.
[223] A. Refregier, J. Rhodes, E. Groth, Astrophys. J. 572 (2002) L131.
[224] A. Refregier, Ann. Rev. Astron. Astrophys. 41 (2003) 645.
[225] A. Refregier, Mon. Not. R. Astron. Soc. 338 (2003) 35.
[226] A. Refregier, D. Bacon, Mon. Not. R. Astron. Soc. 338 (2003) 48.
[227] J. Rhodes, A. Refregier, E. Groth, Astrophys. J. 552 (2001) L85.
[228] A.G. Riess, W.H. Press, R.P. Kirshner, Astrophys. J. 473 (1996) 88.
[229] A.G. Riess, et al., Astron. J. 116 (1998) 1009.
[230] R. Sachs, Proc. R. Soc. Lond. A264 (1961) 309.
[231] R. Schaeffer, Astron. Astrophys. 134 (1984) L15.
[232] R.J. Scherrer, E. Bertschinger, Astrophys. J. 381 (1991) 349.
[233] J. Schmalzing, K.M. Gorski, Mon. Not. R. Astron. Soc. 297 (1998) 355.
[234] C. Schmid, J.-P. Uzan, A. Riazuelo, 2005. astro-ph/0412120.
[235] C. Schimd, I. Tereno, J.-P. Uzan, et al., Phys. Rev. D 71 (2005) 083512. astro-ph/0603158.
[236] P. Schneider, A. Weiss, Astrophys. J. 330 (1988) 1.
[237] P. Schneider, J. Ehlers, E.E. Falco, Gravitational Lenses, Springer-Verlag, Berlin, 1992.
[238] P. Schneider, S. Seitz, Astron. Astrophys. 294 (1995) 411.
[239] P. Schneider, Mon. Not. R. Astron. Soc. 283 (1996) 837.
[240] P. Schneider, H.W. Rix, Astrophys. J. 474 (1997) 25.
[241] P. Schneider, Astrophys. J. 498 (1998) 43.
[242] P. Schneider, L. Van Waerbeke, B. Jain, G. Kruse, Mon. Not. R. Astron. Soc. 296 (1998) 873.
[243] P. Schneider, Perspectives on Radio Astronomy, Scientific Imperatives at cm and m wavelengths, in: Proceedings of a Workshop in Amsterdam, April 7–9, 1999.
[244] P. Schneider, J. Ehlers, E. Falcon, Gravitational Lenses, Springer, 1999.
[245] P. Schneider, L. Van Waerbeke, Y. Mellier, Astron. Astrophys. 389 (2002) 729.
[246] P. Schneider, L. Van Waerbeke, M. Kilbinger, Y. Mellier, Astron. Astrophys. 396 (2002) 1.
[247] P. Schneider, Astron. Astrophys. 408 (2003) 829.
[248] P. Schneider, M. Lombardi, Astron. Astrophys. 397 (2003) 809.
[249] P. Schneider, Gravitational Lensing: Strong, Weak and Micro, in: G. Meylan, P. Jetzer, P. North (Eds.), Lecture Notes of the 33rd Saas-Fee Advanced Course, Springer-Verlag, Berlin, 2006, p. 273. astro-ph/0509252.
[250] P. Schneider, M. Kilbinger, M. Lombardi, Astron. Astrophys. 431 (2005) 9.
[251] R. Scoccimarro, R.K. Sheth, L. Hui, B. Jain, Astrophys. J. 546 (2001) 652.
[252] D. Scott, M.J. Rees, Mon. Not. R. Astron. Soc. 247 (1990) 510.
[253] D. Scott, G. Smoot, 2006. astro-ph/0601307.
[254] R. Scranton, et al., Astrophys. J. 633 (2005) 589.
[255] C. Sealfon, L. Verde, R. Jimenez, Astrophys. J. 649 (2006) 118.

[256] S. Seitz, P. Schneider, J. Ehlers, Classical Quantum Gravity 11 (1994) 2345.
[257] S. Seitz, P. Schneider, M. Bartelmann, Astron. Astrophys. 337 (1998) 325.
[258] U. Seljak, Astrophys. J. 463 (1996) 1. astro-ph/9505109.
[259] U. Seljak, M. Zaldarriaga, Phys. Rev. Lett. 78 (1997) 2054. astro-ph/9609169.
[260] U. Seljak, M. Zaldarriaga, Phys. Rev. D 60 (1999) 043504. astro-ph/9811123.
[261] U. Seljak, Mon. Not. R. Astron. Soc. 318 (2000) 203.
[262] E. Semboloni, L. Van Waerbeke, C. Heymans, et al. astro-ph/0606648.
[263] E. Sheldon, et al., Astron. J. 127 (2004) 2544.
[264] R.K. Sheth, B. Jain, Mon. Not. R. Astron. Soc. 285 (1997) 231.
[265] R.K. Sheth, G. Tormen, Mon. Not. R. Astron. Soc. 308 (1999) 119.
[266] M. Shimon, et al. 2006. astro-ph/0602528.
[267] K. Sigurdson, A. Cooray, Phys. Rev. Lett. 95 (2005) 1303.
[268] J. Silk, Astrophys. J. 151 (1968) 459.
[269] P. Simon, M. Hetterscheidt, M. Schirmer, T. Erben, P. Schneider, C. Wolf, K. Meisenheimer, Astron. Astrophys. 461 (2007) 861.
[270] D.R. Smith, G.M. Bernstein, P. Fischer, M. Jarvis, Astrophys. J. 551 (2001) 643.
[271] R.E. Smith, J.A. Peacock, A. Jenkins, S.D.M. White, C.S. Frenk, et al., Mon. Not. R. Astron. Soc. 341 (2003) 1311.
[272] D. Spergel, et al. 2006. astro-ph/0603449.
[273] J.-L. Starck, S. Pires, A. Refregier, Astron. Astrophys. 451 (2006) 1139.
[274] P.J. Steinhardt, N. Turok, Phys. Rev. D 65 (2002) 126003. hep-ph/0111098.
[275] R. Stompor, G. Efstathiou, Mon. Not. R. Astron. Soc. 302 (1999) 735. astro-ph/9805294.
[276] R.A. Sunyaev, Ya.B. Zel'dovich, Astrophys. Space Sci. 7 (1970) 3.
[277] M. Takada, B. Jain, Mon. Not. R. Astron. Soc. 337 (2002) 875.
[278] M. Takada, B. Jain, Mon. Not. R. Astron. Soc. 340 (2003) 580.
[279] M. Takada, B. Jain, Mon. Not. R. Astron. Soc. 344 (2003) 857.
[280] M. Takada, B. Jain, Mon. Not. R. Astron. Soc. 348 (2004) 897.
[281] M. Takada, M. White, Astrophys. J. 601 (2004) L1.
[282] A. Taruya, M. Takada, T. Hamana, I. Kayo, T. Futamase, Astrophys. J. 571 (2002) 638.
[283] A. Taruya, T. Hamana, I. Kayo, Mon. Not. R. Astron. Soc. 339 (2003) 495.
[284] A.N. Taylor, 2001. astro-ph/0111605.
[285] A.N. Taylor, T.D. Kitching, D.J. Bacon, A.F. Heavens, Mon. Not. R. Astron. Soc. 374 (2007) 1377. astro-ph/0606416.
[286] I. Tereno, O. Dore, L. Van Waerbeke, Y. Mellier, Astron. Astrophys. 429 (2005) 383.
[287] P. Tozzi, P. Madau, A. Meiskin, M.J. Rees, Astrophys. J. 528 (2000) 597.
[288] E.L. Turner, J.P. Ostriker, J,R. Gott, Astrophys. J. 284 (1984) 1.
[289] J. Tyson, F. Valdes, J. Jarvis, A. Mills, Astrophys. J. 281 (1984) L59.
[290] J.P. Uzan, F. Bernardeau, Phys. Rev. D 64 (2001) 3004.
[291] P. Valageas, Astron. Astrophys. 354 (2000) 767.
[292] P. Valageas, Astron. Astrophys. 356 (2000) 771.
[293] P. Valageas, A. Balbi, J. Silk, Astron. Astrophys. 367 (2001) 1. astro-ph/0009040.
[294] P. Valageas, A.J. Barber, D. Munshi, Mon. Not. R. Astron. Soc. 347 (2004) 654.
[295] P. Valageas, D. Munshi, A. Barber, Mon. Not. R. Astron. Soc. 356 (2005) 386.
[296] L. Van Waerbeke, Astron. Astrophys. 334 (1998) 1.
[297] L. Van Waerbeke, F. Bernardeau, Y. Mellier, Astron. Astrophys. 342 (1999) 15.
[298] L. Van Waerbeke, Mon. Not. R. Astron. Soc. 313 (2000) 524.
[299] L. Van Waerbeke, Y. Mellier, T. Erben, J.C. Cuillandre, et al., Astron. Astrophys. 358 (2000) 30.
[300] L. Van Waerbeke, T. Hamana, R. Scoccimarro, S. Colombi, F. Bernardeau, Mon. Not. R. Astron. Soc. 322 (2001) 918.
[301] L. van Waerbeke, Y. Mellier, M. Radovich, E. Bertin, M. Dantel-Fort, et al., Astron. Astrophys. 374 (2001) 757.
[302] L. van Waerbeke, Y. Mellier, R. Pelló, U.-L. Pen, H.J. McCracken, B. Jain, Astron. Astrophys. 393 (2002) 369.
[303] L. van Waerbeke, Y. Mellier, 2003. astro-ph/0305089.
[304] L. Van Waerbeke, M. White, H. Hoekstra, C. Heymans, Astrophys. J. 26 (2006) 91.
[305] L. Verde, A.F. Heavens, W.J. Percival, Mon. Not. R. Astron. Soc. 335 (2002) 432.
[306] J. Wambsganss, R. Cen, J.P. Ostriker, E.L. Turner, Science 268 (1995) 274.
[307] J. Wambsganss, R. Cen, G. Xu, J.P. Ostriker, Astrophys. J. Lett. 475 (1997) 81.
[308] J. Wambsganss, R. Cen, J.P. Ostriker, Astrophys. J. 494 (1998) 29.
[309] Y. Wang, D. Holz, D. Munshi, Astrophys. J. 572 (2002) 15.
[310] Y. Wang, 2005. astro-ph/0406635.
[311] M. White, L. Van Waerbeke, J. Mackey, Astrophys. J. 575 (2002) 640.
[312] M. White, Astrophys. J. 22 (2004) 211.
[313] D.M. Wittman, J. Tyson, D. Kirkman, I. Dell'Antonio, G. Bernstein, Nature 405 (2000) 143.
[314] M. Zaldarriaga, U. Seljak, Phys. Rev. D 59 (1999) 123507.
[315] M. Zaldarriaga, Phys. Rev. D 62 (2000) 063510. astro-ph/9910498.
[316] M. Zaldarriaga, R. Scoccimarro, Astrophys. J. 584 (2003) 559.
[317] S. Zaroubi, G. Squires, Y. Hoffman, J. Silk, Astrophys. J. 500 (1998) L87.
[318] H. Zhan, L. Knox, Astrophys. J. 616 (2004) L75.
[319] J. Zhang, L. Hui, A. Stebbins, Astrophys. J. 635 (2005) 806.
[320] P. Zhang, U.L. Pen, Phys. Rev. Lett. 95 (2005) 241302.
[321] A. Zhitnitsky, Phys. Rev. D 74 (2006) 043515.